

# What can we learn from REE abundances in clinopyroxene and orthopyroxene in residual mantle peridotites?

Yan Liang<sup>1,1</sup>, Zejia Ji<sup>2,2</sup>, and Boda Liu<sup>3,3</sup>

<sup>1</sup>Brown University

<sup>2</sup>Peking University

<sup>3</sup>Rice University

November 30, 2022

## Abstract

Clinopyroxene and orthopyroxene are the two major repositories of rare earth elements (REE) in spinel peridotites. Most geochemical studies of REE in mantle samples focus on clinopyroxene. Recent advances in in situ trace element analysis has made it possible to measure REE abundance in orthopyroxene. The purpose of this study is to determine what additional information one can learn about mantle processes from REE abundances in orthopyroxene coexisting with clinopyroxene in residual spinel peridotites. To address this question, we select a group of spinel peridotite xenoliths (9 samples) and a group of abyssal peridotites (12 samples) that are considered residues of mantle melting and that have major element and REE compositions in the two pyroxenes reported in the literature. We use a disequilibrium double-porosity melting model and the Markov chain Monte Carlo method to invert melting parameters from REE abundance in the bulk sample. We then use a subsolidus reequilibration model to calculate REE redistribution between cpx and opx at the extent of melting inferred from the bulk REE data and at the closure temperature of REE in the two pyroxenes. We compare the calculated results with those observed in clinopyroxene and orthopyroxene in the selected peridotitic samples. Results from our two-step melting followed by subsolidus reequilibration modeling show that it is more reliable to deduce melting parameters from REE abundance in the bulk peridotite than in clinopyroxene. We do not recommend the use of REE in clinopyroxene alone to infer the degree of melting experienced by the mantle xenolith, as HREE in clinopyroxene in the xenolith are reset by subsolidus reequilibration. In general, LREE in orthopyroxene and HREE in clinopyroxene are more susceptible to subsolidus redistribution. The extent of redistribution depends on the modes of clinopyroxene and orthopyroxene in the sample and thermal history experienced by the peridotite. By modeling subsolidus redistribution of REE between orthopyroxene and clinopyroxene after melting, we show that it is possible to discriminate mineral mode of the starting mantle and cooling rate experienced by the peridotitic sample. We conclude that endmembers of the depleted MORB mantle and the primitive mantle are not homogeneous in mineral mode. A modally heterogeneous peridotitic starting mantle provides a simple explanation for the large variations of mineral mode observed in mantle xenoliths and abyssal peridotites. Finally, by using different starting mantle compositions in our simulations, we show that composition of the primitive mantle is more suitable for modeling REE depletion in cratonic mantle xenoliths than the composition of the depleted MORB mantle.

1           What can we learn from REE abundances in clinopyroxene and  
2                           orthopyroxene in residual mantle peridotites?

3

4                           Zejia Ji<sup>1,2</sup>, Yan Liang<sup>1</sup>, and Boda Liu<sup>1,\*</sup>

5       1 Department of Earth, Environmental and Planetary Sciences, Brown University, Providence,  
6                           RI 02912, United States

7       2 The Key Laboratory of Orogenic Belts and Crustal Evolution, Peking University, Beijing,  
8                           100871, China

9       \* Now at Department of Earth, Environmental and Planetary Sciences, Rice University, Houston,  
10                           TX 77005, United States

11                           Corresponding author: Yan Liang ([yan\\_liang@brown.edu](mailto:yan_liang@brown.edu))

12

13                           **Abstract**

14           Clinopyroxene and orthopyroxene are the two major repositories of rare earth elements  
15 (REE) in spinel peridotites. Most geochemical studies of REE in mantle samples focus on  
16 clinopyroxene. Recent advances in in situ trace element analysis has made it possible to accurately  
17 measure REE abundance in orthopyroxene. The purpose of this study is to determine what  
18 additional information one can learn about mantle processes from REE abundances in  
19 orthopyroxene coexisting with clinopyroxene in residual spinel peridotites. To address this  
20 question, we select a group of spinel peridotite xenoliths (9 samples) and a group of abyssal  
21 peridotites (12 samples) that are considered residues of mantle melting and that have mineral  
22 modes and major element and REE abundances reported in the two pyroxenes in the literature. We  
23 use a multi-mineral disequilibrium melting model and the Markov chain Monte Carlo method to  
24 invert melting parameters from REE abundance in the bulk sample. We then use a subsolidus  
25 reequilibration model to calculate REE redistribution between cpx and opx at the extent of melting  
26 inferred from the bulk REE data and at the closure temperature of REE in the two pyroxenes. We  
27 compare the calculated results with those observed in clinopyroxene and orthopyroxene in the

28 mantle sample. Results from our two-step modeling show that it is more reliable to deduce melting  
29 parameters from REE abundance in the bulk peridotite than in clinopyroxene. We do not  
30 recommend the use of REE in clinopyroxene alone to infer the degree of melting experienced by  
31 the mantle xenolith, as HREE in clinopyroxene in the xenolith are reset by subsolidus  
32 reequilibration. In general, LREE in orthopyroxene and HREE in clinopyroxene are more  
33 susceptible to subsolidus redistribution. The extent of redistribution depends on the modes of  
34 clinopyroxene and orthopyroxene in the sample and thermal history experienced by the peridotite.  
35 By modeling subsolidus redistribution of REE between orthopyroxene and clinopyroxene after  
36 melting, we show that it is possible to discriminate mineral mode of the starting mantle and cooling  
37 rate experienced by the peridotitic sample. We conclude that endmembers of the depleted MORB  
38 mantle and the primitive mantle are not homogeneous in mineral mode. A modally heterogeneous  
39 peridotitic starting mantle provides a simple explanation for the large variations of mineral mode  
40 observed in mantle xenoliths and abyssal peridotites. Finally, by using different starting mantle  
41 compositions in our simulations, we show that composition of the primitive mantle is more suitable  
42 for modeling REE depletion in mantle xenoliths than the composition of the depleted MORB  
43 mantle.

44

## 45 1. INTRODUCTION

46 Abundances of rare earth element (REE) in mantle rocks have been widely used to study  
47 partial melting, melt migration and melt-rock interaction processes in the mantle. Most  
48 geochemical studies of REE in spinel peridotites focus on clinopyroxene (cpx) which is the major  
49 repository of REE in the peridotites. Important conclusions based on REE abundances in cpx in  
50 abyssal peridotites include (1) samples with depleted LREE are resulted from fractional or near  
51 fractional melting (Johnson et al., 1990; Johnson and Dick, 1992; Kelemen et al., 1997; Niu and  
52 Hékinian, 1997; Shimizu, 1998; Hellebrand et al., 2001; Brunelli et al., 2006; Liang and Peng,  
53 2010); (2) samples with elevated LREE are due to melt impregnation and melt-rock interaction  
54 (Hellebrand et al., 2002; Warren et al., 2009; Brunelli et al., 2014); and (3) cpx with higher HREE  
55 but depleted LREE is attributed to melting starting in the garnet stability field in the upwelling  
56 mantle (Johnson et al., 1990; Hellebrand et al., 2002; Brunelli et al., 2006). However, not all of  
57 the interpretations are unique. For examples, the slightly elevated LREE patterns in abyssal

58 peridotites that show no obvious signs of melt addition can also be explained by small extent of  
59 disequilibrium melting (Liang and Liu, 2016; Liu and Liang, 2017). Near fractional melting  
60 starting in the garnet stability field failed to explain some samples with elevated HREE patterns  
61 (Liang and Peng, 2010). One possible explanation of the higher than expected HREE in residual  
62 cpx is subsolidus redistribution (Sun and Liang, 2014). During subsolidus reequilibration, REE is  
63 strongly and preferentially partitioning into cpx relative to orthopyroxene (opx) and olivine in  
64 spinel peridotites (e.g., Stosch, 1982; Witt-Eickschen and O'Neill, 2005; Lee et al., 2007; Liang  
65 et al., 2013; Sun and Liang, 2014). To sort out the various magmatic and subsolidus processes  
66 affecting the abundance and distribution of REE and other trace elements in residual peridotites,  
67 additional information is needed.

68         Recent advances in in situ trace element analysis makes it possible to measure REE and  
69 other incompatible trace elements in opx. An increasing number of geochemical studies of spinel  
70 peridotites have reported REE in both cpx and opx (e.g. Hellebrand et al., 2005; Warren et al.,  
71 2009; Brunelli and Seyler, 2010; Seyler et al., 2011; D'Errico et al., 2016). These additional data  
72 not only can be used to reconstruct bulk trace element compositions for samples that experienced  
73 secondary alteration, but also offer an opportunity for a more complete assessment of the thermal  
74 and magmatic history experienced by the peridotite. To learn more from REE abundances in  
75 coexisting cpx and opx in residual peridotite samples, we use a multi-mineral disequilibrium  
76 melting model and a subsolidus reequilibration model to investigate how REE in the bulk residue  
77 are fractionated during decompression melting along a mantle adiabat and how REE in residual  
78 cpx and opx are redistributed during subsolidus reequilibration. In a close system, REE abundance  
79 in the bulk sample is independent of subsolidus reequilibration, whereas REE abundances in  
80 coexisting cpx and opx are sensitive to temperature and mineral mode. Hence it is more  
81 advantageous to infer melting parameters from REE abundance in the bulk sample than in cpx  
82 alone. As will be demonstrated in this study, it is possible to constrain mineral mode in the starting  
83 mantle and thermal history of the residual peridotites based on REE abundances in cpx and opx.

84         The remaining of this paper is organized as follows. In Section 2, we briefly describe key  
85 parameters used in the disequilibrium melting model detailed in Appendix A and the procedure  
86 used in the subsolidus reequilibration calculation. In Section 3, we present two case studies of REE  
87 abundance and distribution in selected residual spinel peridotites from cratons (mantle xenoliths)

88 and mid-ocean ridges (abyssal peridotites). In Section 4, we discuss additional processes or factors  
89 that may contribute to the variations of REE in the bulk and two pyroxenes in some of the samples  
90 included in this study. We then compare melting parameters derived from REE in the bulk and cpx  
91 alone for the selected mantle xenoliths and abyssal peridotite samples. Finally, in Section 5, we  
92 summarize the main results of this study. The methodology developed in this study is general and  
93 can be used to study the abundance and distribution of REE as well as other incompatible trace  
94 elements in residual mantle samples from a variety of tectonic settings.

95

## 96 2. MELTING FOLLOWED BY SUBSOLIDUS REEQUILIBRATION

### 97 2.1. Model description

98 We are interested in the fractionation of REE in cpx and opx during decompression melting  
99 in an upwelling steady-state mantle column and the redistribution of REE between cpx and opx at  
100 a subsolidus temperature after melting. We use the multi-mineral disequilibrium melting model of  
101 Liang and Liu (2016) to simulate REE depletion during partial melting along a mantle adiabat.  
102 Key features of the melting model include channelized melt extraction and diffusion-limited  
103 chemical exchange between the pyroxenes and the interstitial melt. Because diffusivities of REE  
104 in olivine and garnet are considerably larger than those in the pyroxenes (Van Orman et al., 2001,  
105 2002; Cherniak and Liang, 2007; Cherniak, 2015) and abundances of REE in olivine and spinel  
106 are much smaller than those in the pyroxenes, it is reasonable to assume that olivine and spinel  
107 (also garnet for melting in the garnet stability field) are in local chemical equilibrium with their  
108 interstitial melt during melting.

109 The governing mass conservation equations and their simplifications are summarized in  
110 Appendix A. There are four dimensionless parameters in the multi-mineral disequilibrium melting  
111 model for this problem: degree of melting experienced by the residual mantle ( $F$ ), fraction of melt  
112 extracted to the channel ( $\mathbb{R}$ , called melt suction rate hereafter), disequilibrium parameter of La in  
113 cpx ( $\varepsilon_{cpx}^{La}$ ), and relative diffusion rate of REE in cpx and opx ( $\frac{R_{cpx}}{R_{opx}}$ ). The limits of perfect fractional  
114 melting and batch melting are realized when  $\mathbb{R} = 0$  and  $\mathbb{R} = 1$ , respectively. The limit of  
115 equilibrium melting is realized when  $\varepsilon_{cpx}^{La} = 0$ . The diffusive exchange rate constants for an REE

116 in opx ( $R_{\text{opx}}$ ) and cpx ( $R_{\text{cpx}}$ ) are inversely proportional to the diffusive time scales for opx and cpx  
 117 (Navon and Stolper, 1987; Bodinier et al., 1990; Liang, 2003):

$$118 \quad R_{\text{opx}} = \frac{3\beta D_{\text{opx}}}{d_{\text{opx}}^2}, \quad R_{\text{cpx}} = \frac{3\beta D_{\text{cpx}}}{d_{\text{cpx}}^2}, \quad (1a, 1b)$$

119 where  $D$  is the diffusion coefficient of REE in opx or cpx;  $d$  is the average or effective mineral  
 120 grain size of opx or cpx; and  $\beta$  is a geometric factor. The relative diffusion rate for an REE is given  
 121 by the expression:

$$122 \quad \frac{R_{\text{opx}}^{\text{REE}}}{R_{\text{cpx}}^{\text{REE}}} = \frac{D_{\text{opx}}^{\text{REE}}}{D_{\text{cpx}}^{\text{REE}}} \frac{d_{\text{cpx}}^2}{d_{\text{opx}}^2}. \quad (2)$$

123 The disequilibrium parameter is a measure of bulk melting rate relative to diffusion rate for the  
 124 element of interest in a mineral (Eq. A1d in Appendix A). Given the disequilibrium parameter of  
 125 La in cpx, disequilibrium parameters for other REE in cpx can be calculated according to their  
 126 diffusivity ratio (Liang and Liu, 2016):

$$127 \quad \varepsilon_{\text{cpx}}^{\text{REE}} = \frac{D_{\text{cpx}}^{\text{La}}}{D_{\text{cpx}}^{\text{REE}}} \varepsilon_{\text{cpx}}^{\text{La}}. \quad (3)$$

128 During decompression melting along a mantle adiabat, temperature decreases upward in the  
 129 melting column. In this study, we calculate the relative diffusion rate and disequilibrium  
 130 parameters using experimentally determined diffusion parameters for REE in cpx and opx (Van  
 131 Orman et al., 2001, 2002; Cherniak and Liang, 2007). For convenience of numerical calculations,  
 132 we scale the disequilibrium parameters in Eq. 3 by their respective values at 1300°C,

$$133 \quad \varepsilon_{\text{cpx}}^T = \frac{D_{\text{cpx}}^{1300}}{D_{\text{cpx}}^T} \varepsilon_{\text{cpx}}^{1300}. \quad (4)$$

134 In the simulations presented below, we treat  $\varepsilon_{\text{cpx}}^{1300}$  for La in cpx as a free parameter and calculate  
 135 the disequilibrium parameter at other temperatures using Eq. 4. Variations of the disequilibrium  
 136 parameter of La in cpx as a function of temperature and degree of melting along a 1300 °C mantle  
 137 adiabat can be found in supplementary Fig. S1.

138 We use the temperature and major element composition dependent opx-cpx and olivine-  
 139 cpx REE partitioning models of Sun and Liang (2014) and mineral mode in the sample to calculate  
 140 REE abundances in coexisting opx and cpx at a subsolidus temperature after melting. In a closed  
 141 system, concentration of a trace element in the bulk peridotite ( $C_s$ ) depends on mineral mode and  
 142 mineral composition, but is independent of temperature, viz.,

$$143 \quad C_s = w_{cpx}C_{cpx} + w_{opx}C_{opx} + w_{ol}C_{ol} + w_{sp}C_{sp}, \quad (5)$$

144 where  $w_j$  and  $C_j$  are the weight fraction of and trace element concentration in mineral  $j$  in the  
 145 residual peridotite, respectively. Since REE abundances in olivine and spinel are much lower than  
 146 those in cpx and opx, concentrations of a REE in cpx and opx at a given temperature ( $T$ ) can be  
 147 calculated using the expressions (see also Eq. A2e in Appendix A):

$$148 \quad C_{cpx}(T) = \frac{C_s}{w_{cpx} + w_{opx} k_{opx-cpx}}, \quad (6a)$$

$$149 \quad C_{opx}(T) = k_{opx-cpx} C_{cpx}, \quad (6b)$$

150 where  $k_{opx-cpx}$  is the temperature and major element composition dependent opx-cpx REE partition  
 151 coefficient. In the case studies presented in Section 3, we set the temperature in Eqs. 6a and 6b to  
 152 the closure temperature of REE based on the REE-in-two-pyroxene thermometer of Liang et al.  
 153 (2013).

## 154 2.2. Forward simulations of REE in pyroxenes during melting and subsolidus reequilibration

155 Variations of REE in opx and cpx in residual peridotites that have experienced  
 156 decompression melting and subsolidus reequilibration can be visualized through forward  
 157 simulations using the two-step melting followed by subsolidus reequilibration model outlined in  
 158 Section 2.1. Figure 1a shows one such example for a case of 6% near fractional melting ( $R = 0.95$ ,  
 159  $\epsilon_{La}^{1300} = 0.01$ ) of spinel lherzolite along the 1300 °C adiabat. Melting strongly depletes LREE in  
 160 both cpx and opx, hence the bulk rock (solid lines in Fig. 1a). Since REE abundances in cpx are  
 161 considerably higher than those in opx, olivine and spinel, REE pattern of the bulk residue follows  
 162 that of cpx, forming subparallel trends in the chondrite-normalized REE diagram (Fig. 1a). To the  
 163 first order, REE abundance in the bulk rock is proportional to the amount of cpx in the residue,  
 164 viz.,  $C_s \sim w_{cpx} * C_{cpx}$ . This is demonstrated in Fig. 1a where the abundance of REE in cpx is about

165 7 times that in the bulk rock and the modal abundance of cpx in the residue after 6% of melt is  
166 13.6 %. The close similarity between REE in the bulk rock and its constituent cpx forms the basis  
167 for using REE in cpx to study mantle melting processes in the literature.

168 Figure 1a also shows that REE pattern of residual opx differs considerable from those of  
169 cpx and the residue: light and middle REE are preferentially depleted in opx relative to those in  
170 the bulk or cpx whereas heavy REE in opx are comparable to those in the bulk rock. This is due to  
171 the smaller M2 site of opx structure, making LREE more incompatible in opx than in cpx. The net  
172 effect is a steeper LREE depleted pattern for opx in the REE diagram. The REE pattern in opx can  
173 be further complicated by subsolidus reequilibration: with decreasing temperature, LREE is  
174 preferentially redistributed from opx to cpx, shifting the entire opx REE pattern below that  
175 produced by partial melting (cf. dashed and solid green lines in Fig. 1a). Although it is not  
176 straightforward to infer mantle melting processes based on REE abundances and patterns in opx  
177 in residual peridotites, abundances of REE in opx may offer useful information on the thermal  
178 history experienced by the peridotite (e.g., Liang et al., 2013; Dygert and Liang, 2015; Wang et  
179 al., 2015; Dygert et al., 2017) and mineral modes in the starting mantle. We will demonstrate these  
180 points in Sections 3 and 4. However, due to the ionic size-dependent REE partitioning between  
181 opx and cpx, subsolidus reequilibration mildly elevates HREE in cpx (Fig. 1a), which may  
182 complicate the interpretation of garnet signal in residual spinel lherzolite and harzburgite (Sun and  
183 Liang, 2014). Since the abundance of LREE is considerably lower in residual opx, LREE in cpx  
184 are not sensitive to subsolidus redistribution in spinel lherzolite. When the degree of melting is  
185 large, the modal abundance of cpx decreases in the residue, and the effect of subsolidus  
186 reequilibration on the LREE in cpx will be more significant. Supplementary Fig. S2 presents a  
187 calculated example for a case of 15% near fractional melting ( $R = 0.95$ ,  $\epsilon_{La}^{1300} = 0.01$ ).

188 The mineral grain size also affects REE abundances in cpx and opx during disequilibrium  
189 melting and subsequent cooling through the relative diffusive exchange rate (Eq. 2). In general,  
190 grain size of opx (2-5 mm) is larger than grain size of cpx (1-2 mm) in residual spinel peridotites.  
191 The effect of chemical disequilibrium increases with increasing opx grain size, leading to an  
192 increase in the effective partition coefficient for REE between opx and its coexisting melt (Liang  
193 and Liu, 2016). This can be demonstrated through a forward simulation in which we increase the  
194 relative opx-to-cpx grain size from 1 to 5 while keeping the cpx grain size to 1 mm. As shown in

195 Fig. 1b, the calculated middle and heavy REE abundances in cpx slightly decrease whereas the  
196 light REE abundances in opx significantly increase compared to the case of 1 mm opx.  
197 Consequently, the simulated bulk REE is not very sensitive to the choice of opx/cpx grain size  
198 ratio. Regardless how REE are distributed between opx and cpx, the REE abundance in the bulk  
199 residue remains the same as that produced by partial melting. Hence it is more reliable to use REE  
200 in the bulk rock to infer melting processes experienced by residual peridotites than REE in cpx  
201 alone. We will demonstrate this point through two case studies below.

202

### 203 3. READING MAGMATIC AND THERMAL HISTORY FROM REE ABUNDANCES IN 204 BULK PERIDOTITES AND TWO PYROXENES: AN INVERSE STUDY

205 The multi-mineral disequilibrium melting model can be used to infer melting parameters  
206 from measured REE abundance in bulk residual peridotites through inverse geochemical modeling.  
207 In this study we investigate REE + Y abundances in selected spinel peridotite samples from cratons  
208 (mantle xenoliths) and mid-ocean ridges (abyssal peridotites). We include Y in our analysis  
209 because it behaves similarly to HREE during mantle melting and its abundance is routinely  
210 measured along with REE in opx and cpx. Peridotites from stable cratons are generally well-  
211 equilibrated and have similar and relatively low equilibrium or closure temperatures for both major  
212 elements and REE in coexisting cpx and opx, whereas abyssal peridotites have higher closure  
213 temperatures for REE than major elements in pyroxenes (Liang et al., 2013; Dygert and Liang,  
214 2015; Wang et al., 2015). This is illustrated in Fig. 2 for the selected samples in this study. Since  
215 abyssal peridotites are variously serpentinized and some mantle xenoliths contain glass veins, we  
216 use measured REE + Y abundances in minerals (cpx, opx, and olivine when available) and mineral  
217 modes reported in the literature to reconstruct bulk REE + Y abundances in the peridotites. As  
218 shown in Fig. 1, the light and middle REE in opx are considerably lower than those in cpx, making  
219 accurate measurements of these elements in opx an analytical challenge. This problem is especially  
220 prevalent for odd atomic number elements such as La (57) and Pr (59), resulting in scattered LREE  
221 patterns in some samples. To include more elements and more samples in this study, we applied  
222 an interpolation procedure to some of the samples that exhibit scattered REE patterns. The  
223 procedure, detailed in Supplementary Materials, is based on correlation between the nearest  
224 neighbor REE (e.g., La and Ce) established by mantle pyroxenes that have smooth REE patterns.

225 In Supplementary Table S1a, we list mineral modes and REE abundances in cpx, opx, and the bulk  
226 peridotite included in this study.

227 In order to use the multi-mineral disequilibrium melting model to calculate the melting  
228 parameters from the bulk REE + Y abundance in residual peridotites, we need to know mineral  
229 grain size, mineral mode, and composition of the starting mantle. Following standard practice in  
230 REE modeling, we assume that abundances of REE + Y in the starting mantle are the same as the  
231 average DMM (Workman and Hart, 2005) for abyssal peridotites and the primitive mantle (PM,  
232 McDonough and Sun, 1995) for mantle xenoliths. We will discuss effects of other starting mantle  
233 compositions in Section 4. The mineralogy of the starting mantle is a primitive spinel lherzolite.  
234 (Effect of garnet field melting will be discussed in Section 3.2.) There are some uncertainties in  
235 the mineral mode of the starting mantle. For example, the DMM of Workman and Hart (2005)  
236 consists of 13% cpx, 28% opx, 57% olivine, and 2% spinel, whereas the starting mantle of Johnson  
237 (1998) and Hellebrand et al. (2002) has 17% cpx, 27% opx, 53% olivine, and 3% spinel. The latter  
238 has been used in our recent studies of REE depletion in residual cpx from abyssal peridotites (Liang  
239 and Peng, 2010; Liang and Liu, 2016; Liu and Liang, 2017). Figs. 3a and 3b show large variations  
240 in mineral modes in both mantle xenoliths and abyssal peridotites (see also Fig. 4 in Warren, 2016  
241 for more abyssal peridotite data). Even for the small number of samples included in the present  
242 study, the range of modal variations cannot be explained by a single melting trend or melting  
243 reaction using either of the starting mode mentioned above. It is possible that mineral modes are  
244 not well constrained for some of the peridotite samples (e.g., heavily serpentinized abyssal  
245 peridotites). Estimates of modal abundance of fresh mantle xenoliths are typically made through  
246 mass balance calculations using measured major and minor element concentrations in the bulk  
247 sample and constituent minerals, which is likely more accurate than point counting. It is possible  
248 that mineral mode in the starting mantle is not uniform. In this study, we consider three mineral  
249 modes for the starting mantle source. For simplicity, we fix the modal abundance of olivine in the  
250 mantle source to 56% and vary the cpx:opx proportion in the mantle source (Fig. 3). This is a  
251 reasonable approach as (1) the relative REE pattern in the bulk rock is not very sensitive to the  
252 abundance of olivine in the mantle source, and (2) the resultant residual modes cover a wider range  
253 of mineral modal abundances (Fig. 3). Finally, the grain size of the starting mantle is unknown,  
254 although in general grain size of opx is larger than grain size of cpx in peridotites. As a starting

255 model, we assume that the grain size ratio between opx and cpx ( $\frac{d_{cpx}}{d_{opx}}$ ) does not change during  
256 melting. The latter helps to simplify the evaluation of the relative diffusion rate between opx and  
257 cpx (Eq. 2).

258 Since there is no analytical solution to the multi-mineral disequilibrium melting model (Eqs.  
259 A2a-A2c in Appendix A), we use Markov chain Monte Carlo (MCMC) method to invert for the  
260 melting parameters  $F$ ,  $\epsilon_{cpx}^{1300}$ , and  $\mathbb{R}$ . MCMC methods are a class of powerful statistical tools for  
261 solving nonlinear inverse problems (e.g., Sambridge and Mosegaard, 2002). Liu and Liang (2017)  
262 used MCMC to invert melting parameters from REE abundance in residual cpx in abyssal  
263 peridotites. To facilitate MCMC inversion, we set bounds for the disequilibrium parameter  $\epsilon_{cpx}^{1300}$   
264 to  $[0, 0.15]$  and the melt suction rate  $\mathbb{R}$  to  $[0, 1]$ , based on previous inversion results using similar  
265 model or method (Lundstrom, 2000; Liang and Peng, 2010; Liang and Liu, 2016; Liu and Liang,  
266 2017). We run 10,000 to 50,000 simulations for each sample to ensure convergence and use the  
267 result to calculate best fitting parameters and uncertainties. The best fitting parameters are then  
268 used to calculate REE abundances in the bulk sample, residual cpx and opx, and chemically re-  
269 equilibrated cpx and opx at subsolidus temperatures. Below we present results from two case  
270 studies.

### 271 3.1. Case 1: Mantle xenoliths

272 To demonstrate the basic feature of the multi-mineral disequilibrium melting model and  
273 the effect of subsolidus redistribution, we select 9 well-characterized spinel lherzolite and  
274 harzburgite xenoliths from the literature: 3 samples from Yangyuan, North China Craton (Liu et  
275 al., 2012), 1 sample from West Eifel, Germany (Witt-Eickschen and O'Neill, 2005), 1 sample from  
276 East Africa Rift (Bedini and Bodinier, 1999), 3 samples from Kilbourne Hole, New Mexico  
277 (Harvey et al., 2012), and 1 sample from the Coast Ranges of central California (Quinn et al.,  
278 2018). These samples are protogranular, free of garnet, plagioclase, hydrous minerals, and veins.  
279 They are selected on the basis of their depleted light REE patterns in cpx and opx, well-defined  
280 linear trends for at least the middle and heavy REE in the inversion diagram of the REE-in-two-  
281 pyroxene thermometer, and similar equilibrium temperatures between major element-based and  
282 REE-based pyroxene thermometers. Figure 2 shows that the calculated temperatures are generally  
283 below the solidus of the peridotite xenoliths. Figure 3a displays modal abundances of the selected

284 samples. For reference, we plot selected major element concentrations in these samples as a  
 285 function of bulk MgO content and spinel Cr# (= 100Cr/Cr+Al, in molar) in supplementary Figs.  
 286 S3a and S3b. Supplementary Tables S1b and S2 and Fig. S5 present results of MCMC simulations  
 287 with PM and DMM starting compositions for the nine xenolith samples along the 1300°C mantle  
 288 adiabat (Fig. S1). Figure 4 shows an example of MCMC simulations for sample CK-2 from the  
 289 Coast Ranges of central California (Quinn et al., 2018). The main results are summarized below.

290 First, the bulk REE patterns are well reproduced by the multi-mineral disequilibrium  
 291 melting model. The quality of fit is not very sensitive to the choice of starting mantle mode (cf.  
 292 Figs. 4a-4c). This is shown by the similar Pearson's Chi-squares among the three cases for each  
 293 sample (Supplementary Table S2). Here we calculate Pearson's Chi-square for the bulk REE after  
 294 inversion using the expression:

$$295 \quad \chi_{bulk}^2 = \sum_{j=1}^N \frac{(C_{s,j} - C_{s,j}^m)^2}{C_{s,j}}, \quad (7)$$

296 where  $C_{s,j}$  and  $C_{s,j}^m$  are the model-derived and measured bulk solid concentrations for element  $j$ ,  
 297 respectively;  $N$  is the number of elements in the model. In general, the smaller the Pearson's Chi-  
 298 square, the better the predict model will be. There is a small trade-off between cpx abundance in  
 299 the starting mantle and the degree of melting: the higher the cpx mode in the starting mantle, the  
 300 greater the degree of melting is required to match the observed depletion in REE in the bulk residue.  
 301 Increasing cpx mode from 14% to 20% in the starting mantle results in 0.11~3% increase in the  
 302 inferred degree of melting for the nine xenolith samples.

303 Second, the observed REE patterns in residual cpx and opx (filled blue and green circles  
 304 in Fig. 4) cannot be reproduced directly using melting parameters derived from the bulk REE  
 305 pattern (blue and green solid lines). Very often, LREE in opx is overestimated and HREE in cpx  
 306 is underestimated by the melting model, which appears to be consistent with the subsolidus  
 307 reequilibration trends displayed in Fig. 1a. To quantify the effect of subsolidus redistribution, we  
 308 recalculated the model-derived REE abundances in opx and cpx using the temperature and major  
 309 element composition dependent REE opx-cpx partition coefficients (Sun and Liang, 2014) and  
 310 closure temperatures ( $T_{REE}$ ) derived from the REE-in-two-pyroxene thermometer (Liang et al.,  
 311 2013). The latter is 964°C for sample CK-2. Figure 4 and supplementary Fig. S5 show that the

312 matches to the measured REE patterns in cpx and opx in the nine xenolith samples are considerably  
313 improved after adjustment of subsolidus redistribution. This is an important result from this study.

314 Finally, for a given sample, our preferred starting mantle mode and melting parameter  
315 should have the smallest sum of Pearson's Chi-squares for the bulk peridotite, cpx, and opx among  
316 the three starting mantle modes, where Pearson's Chi-squares for cpx and opx are calculated after  
317 adjustment for subsolidus reequilibration. Supplementary Table S2 lists melting parameters of our  
318 preferred model. It is interesting to note that the quality of fit to REE patterns in cpx is comparable  
319 to that based on inversion of REE in cpx alone, as the calculated Pearson's Chi-squares for cpx  
320 from the bulk model and cpx alone model are very similar for the nine samples (Supplementary  
321 Table S2). The misfits, if present, are mostly LREE in opx and cpx. (We will discuss the misfits  
322 in Section 4.) Figure 4 and supplementary Fig. S5 also show that the recalculated REE patterns in  
323 model-derived opx and cpx (dashed lines) are sensitive to starting mantle mode. This is highlighted  
324 by the large differences in the sum of Pearson's Chi-squares among the three choices of mantle  
325 mode (e.g., 0.94, 4.25, and 15.2 for 14%, 17%, and 20% cpx in the starting mantle, respectively  
326 for sample CK-2). Hence by modeling REE redistribution among cpx, opx, and olivine in the  
327 mantle xenolith after melting, it is possible to constrain mineral mode of the starting mantle.

### 328 3.2. Case 2: Abyssal peridotites

329 Trace element abundances in cpx in abyssal peridotites have been widely used to study  
330 melting and melt-rock interaction processes beneath mid-ocean ridges (e.g., Johnson et al., 1990;  
331 Kelemen et al., 1997; Hellebrand et al., 2002, 2005; Salters and Dick, 2002; Hellebrand and Snow,  
332 2003; Brunelli et al., 2006; Warren et al., 2009; Brunelli and Seyler, 2010; D'Errico et al., 2016).  
333 Detailed modeling of REE patterns in residual cpx in abyssal peridotites from Central Indian Ridge  
334 (data from Hellebrand et al., 2002) using an equilibrium near fractional melting model revealed a  
335 systematic difference between measured and calculated HREE in cpx: very often model predicted  
336 HREE in cpx are slightly lower than those measured in actual samples (see Fig. 8 in Liang and  
337 Peng, 2010). To fit the HREE in cpx, one can decrease the extent of melting, but this would result  
338 in an over estimation of LREE in cpx. One way to get around this dilemma is by allowing small  
339 extent of chemical disequilibrium for LREE in cpx (Liang and Liu, 2016; Liu and Liang, 2017),  
340 which hinders the depletion of LREE in cpx. This is consistent with measured rates of REE  
341 diffusion in diopside (Van Orman et al., 2002). Another possible way to elevate HREE in cpx is

342 through subsolidus reequilibration, as we demonstrated in previous sections. However, the extent  
343 of subsolidus redistribution may be limited due to higher REE closure temperatures recorded in  
344 abyssal peridotites (Fig. 2) (Liang et al., 2013; Dygert and Liang, 2015; Yao and Liang, 2015).  
345 Yet another mechanism to produce depleted LREE and elevated HREE in cpx is to start melting  
346 in the garnet stability field (e.g., Johnson et al., 1990; Hellebrand et al., 2002; Brunelli et al., 2006).

347 To critically assess the roles of garnet field melting, finite rate of chemical exchange for  
348 LREE, and subsolidus redistribution of REE between cpx and opx in affecting REE patterns in  
349 abyssal peridotites, we select 12 residual abyssal peridotites from the literature that reported REE  
350 abundances in both cpx and opx: 4 samples from eastern Southwest India Ridge (SWIR, Selyer et  
351 al., 2011), 2 samples from Gakkel Ridge (D'Errico et al., 2016), 4 samples from western SWIR  
352 (Warren et al., 2009), and 2 samples from Central Atlantic Ridge (Brunelli and Seyler, 2010).  
353 Based on the criteria of Warren (2016), these samples are residual peridotites as they are free of  
354 plagioclase and melt veins, have low TiO<sub>2</sub> in spinel and LREE deplete REE patterns in cpx and  
355 opx. Similar to mantle xenoliths, these samples also have well-defined linear trends for at least the  
356 middle and heavy REE in the inversion diagram of the REE-in-two-pyroxene thermometer. Fig.  
357 3b display modal abundances of the selected samples. For reference, we also plot major element  
358 compositions of the samples as a function of bulk MgO content and spinel Cr# in supplementary  
359 Figs. S4a and S4b. Previous experimental studies have demonstrated that melting reaction of  
360 peridotite varies systematically with pressure (e.g., Kinzler and Grove, 1992; Baker and Stolper,  
361 1994; Walter and Presnall, 1994). During decompression melting of garnet lherzolite, modal  
362 abundance of opx first increases until the pressure is around 2 GPa and then decreases as the  
363 pressure decreases (Ghiorso et al., 2002; Walter, 2014). To include more realistic melting reaction  
364 for decompression melting, we use pMELTS (Ghiorso et al., 2002) to calculate mineral mode  
365 along an adiabatic melting path that has a potential temperature of 1330°C. The starting mantle  
366 contains 150 ppm water. In this pMELTS-based model, the maximum extent of melting in the  
367 garnet stability field is 0.7% and the cpx exhausts at  $F = 20\%$ . Since there is no clear experimental  
368 nor geophysical evidence for the presence of high-porosity channels at depth greater than 60 km  
369 beneath mid-ocean ridges, we use the batch melting model for melting in the garnet stability field  
370 (i.e., by setting  $\mathbb{R} = 0$  in our model). Fig. 3b displays variations of mineral mode in residual  
371 peridotites calculated using pMELTS for three choices of starting mantle mineralogy (solid curves).  
372 Supplementary Fig. S6 and Supplementary Tables S1c and S2 present simulation results for

373 individual samples. Figure 5 shows an example of MCMC simulations for sample Van 7-85-49  
374 from Western SWIR (Warren et al., 2009). The main results are summarized below.

375           Similar to the case of mantle xenolith, the multi-mineral disequilibrium melting model can  
376 fit the bulk REE patterns very well for most of the abyssal peridotite samples included in this study.  
377 The exceptions are sample Van7-96-38 from Western SWIR (Warren et al., 2009) and sample Dr  
378 23-3-2 from Eastern SWIR (Seyler et al., 2011) which exhibit some misfits in light and middle  
379 REE (Fig. S6). We will discuss the misfits in Section 4.1. As in the case of mantle xenolith, the  
380 quality of fit to the bulk REE data is not very sensitive to the starting mantle mode, and the match  
381 to the measured REE in cpx and opx depends strongly on the starting mantle mode (cf. the three  
382 cases in Fig. 5). Overall, the fits to the observed REE patterns in cpx and opx are improved after  
383 adjustment of subsolidus redistribution (cf. solid and dashed lines in Fig. 5 and Fig. S6). However,  
384 the improvement is moderate because of the relatively high  $T_{REE}$  for the peridotite samples (Fig. 2)  
385 and very small adjustment for REE in cpx. These are consistent with the simply analysis of Sun  
386 and Liang (2014) and the inferred thermal history of abyssal peridotites (Liang et al., 2013; Dygert  
387 and Liang, 2015; Yao and Liang, 2015). Supplementary Table 2 lists melting parameters of our  
388 preferred model for the 12 abyssal peridotite samples based on the sum of Pearson's Chi-squares  
389 of the bulk and subsolidus redistributed cpx and opx.

390

## 391 **4. DISCUSSION**

### 392 **4.1. Misfits of REE in the bulk samples**

393           Although the multi-mineral disequilibrium melting model can account for most of the  
394 variations of REE + Y in the bulk peridotites, noticeable misfits in the light and middle REE are  
395 observed in samples Van7-96-38 (from Western SWIR, Warren et al., 2009) and Dr23-3-2 (from  
396 eastern SWIR, Seyler et al., 2011, see Fig. S6). In both cases, the model-predicted La, Er, Tm and  
397 Yb in the bulk residue are higher than, whereas the predicted Nd, Sm, E, Gd and Tb are lower than,  
398 measured values in the samples. This humped feature is not sensitive to starting mantle mode, and  
399 is also present in the cpx-alone inversion models. Addition of melt would elevate La in cpx and  
400 opx and hence cannot explain the depleted LREE patterns in the two samples. The lower than  
401 expected bulk La, Er, Tm and Yb can be accounted for by increasing the degree of melting, but

402 this would result in additional misfits in Nd, Sm, E, Gd and Tb. Since partition coefficients of  
403 middle REE in cpx are higher than those in garnet and the partition coefficients of HREE in cpx  
404 are lower than those in garnet, prolonged melting in the garnet stability field can produce the  
405 humped middle REE pattern in cpx and the bulk residue (e.g., Johnson et al., 1990). Our pMELTS  
406 based model for abyssal peridotites presented in Section 3.2 includes 0.7% initial melting in the  
407 garnet field. To further explore the role of garnet field melting, we consider a hypothetical case in  
408 which batch melting in the garnet stability field is 4.1%. Supplementary Fig. S7 presents the  
409 simulation results. The simulated bulk rock and pyroxene REE patterns after 4.1% batch melting  
410 in the garnet field show only a small improvement for sample Dr23-3-2 (the sum of Pearson's Chi-  
411 squares decreases from 3.8 to 3.3 which is still higher than the other 10 abyssal peridotites) and no  
412 improvement at all for sample Van7-96-38. Hence the misfits are unlikely due to batch melting in  
413 the garnet stability field. Although fractional melting of garnet lherzolite can produce humped  
414 REE in cpx (Johnson et al., 1990), the physical mechanism for fractional melting in the garnet  
415 stability field remains uncertain.

416 Abyssal peridotites are heavily altered by serpentinization. It is possible that mineral modes  
417 in these two samples are not accurately determined. To explore this possibility, we reconstruct two  
418 new modal abundances for the two samples: one by increasing cpx mode by 2% and decreasing  
419 opx mode by 2%, and the other by decreasing cpx mode by 2% and increasing opx mode by 2%.  
420 We run MCMC simulations followed by subsolidus redistribution for these 4 cases and the results  
421 are shown in supplementary Fig. S8. Changing cpx mode by  $\pm 2\%$  in the samples does not lead to  
422 a significant improvement in the fit to the reconstructed bulk REE in these two samples (i.e., the  
423 humped pattern persists). However, addition of 2% cpx does result in moderate improvement in  
424 the match to the observed REE patterns in cpx and opx in the two samples. This is confirmed by  
425 the smaller sum of Pearson's Chi-squares for the +2% cpx case.

426 We should point out that none of the hypotheses explored in this section can explain the  
427 humped REE pattern in cpx using the cpx-alone inversion model. In theory, one can match the  
428 observed REE pattern in bulk residue by judiciously adjusting starting mantle composition. It is  
429 possible that composition of the starting mantle for these two samples are different from DMM.  
430 We will come back to this point in Section 4.3.

#### 431 **4.2. Misfits of LREE in opx and cpx: Incomplete reequilibration?**

432 A common misfit shared by all the abyssal peridotite samples and four of the nine mantle  
433 xenoliths (ET80, CK-2, YY-26B, and KN03-25) in this study is that model-derived LREE (La +  
434 Ce + Pr ± Nd) are lower in cpx but higher in opx than measured values in cpx and opx, respectively.  
435 The misfit, which persists even after adjustment of subsolidus re-distribution, can be visualized by  
436 plotting the apparent opx/cpx REE partition coefficient against REE ionic radius: the apparent  
437 partition coefficients for the middle and heavy REE follow closely to an isotherm, whereas those  
438 for LREE are gradually displaced above the isotherm, defining a spoon-shaped or U-shaped pattern  
439 (Figs. 6a and 6b). In the inversion diagram for the REE-in-two-pyroxene thermometer, the  
440 displaced LREE fall below the linear trend established by the heavy and middle REE and are  
441 excluded from the temperature calculation (Liang et al., 2013). Spoon- or U-shaped opx/cpx REE  
442 partitioning pattern is a common feature among mantle samples (e.g., Stosch, 1982; Agranier and  
443 Lee, 2007; Seyler et al., 2011). It arises when LREE in opx and cpx are out of chemical equilibrium.  
444 Agranier and Lee (2007) identified two mechanisms that can produce U-shaped disequilibrium  
445 patterns in mantle xenoliths from Dish Hill, California and abyssal peridotites from the Gakkel  
446 Ridge: diffusive fractionation at subsolidus state or metasomatism introduced by “injection and  
447 subsequent freezing in of small amounts of melt” under lithospheric or asthenospheric conditions.  
448 These authors preferred the latter mechanism as they argued that diffusive fractionation alone  
449 could not account for the large deviation in the apparent opx/cpx LREE partition coefficients in  
450 some samples. The 9 mantle xenoliths and 12 abyssal peridotite samples included in the present  
451 study are all depleted in LREE. Given that our multi-mineral disequilibrium melting model can fit  
452 the bulk REE patterns very well in these samples, we can rule out the melt addition hypothesis for  
453 these samples.

454 We suggest that the spoon- or U-shaped opx/cpx REE partitioning patterns can be produced  
455 by disequilibrium melting followed by diffusive exchange between cpx and opx at subsolidus state.  
456 Figures 6a and 6b compare the apparent opx/cpx REE partition coefficients calculated from the  
457 measured REE abundances in opx and cpx in mantle xenolith CK-2 from the Coast Ranges of  
458 central California (Quinn et al., 2018, filled circles) and abyssal peridotite Van7-85-49 from  
459 western SWIR (Warren et al., 2009) with those calculated using melting parameters derived from  
460 our MCMC simulations (magenta lines). (Similar plots for other samples included in this study are  
461 presented in supplementary Figs. S5 and S6.) In both samples, the simulated apparent partition  
462 coefficients at the end of melting are displaced above the measured values. Since opx/cpx REE

463 partition coefficients decrease with the decrease of temperature (cf. the three isotherms in Fig. 6)  
464 and diffusion coefficients of REE in cpx increase systematically from La to Lu at a given  
465 temperature (Van Orman et al., 2001, 2002; see also supplementary Fig. S1c), time scales for  
466 diffusive exchange between opx and cpx in a closed system are longer for LREE than HREE (see  
467 Fig. 5 in Liang, 2014). During diffusive reequilibration, HREE approach opx/cpx equilibrium  
468 partitioning faster than LREE. Depending on thermal history experienced by the samples (e.g.,  
469 cooling and upwelling rates), the elevated opx/cpx REE patterns produced by disequilibrium  
470 melting (magenta lines in Fig. 6) would be gradually relaxed to the spoon-shaped pattern recorded  
471 in the peridotite samples (filled circles). As a proof-of-concept, we carry out two forward  
472 simulations of diffusive reequilibration of REE between opx and cpx under two prescribed cooling  
473 rates. In this simple demonstration, cooling starts at the end of melting and terminates at the closure  
474 temperature of REE (i.e.,  $T = T_{REE}$ ). Figures 6a and 6b show that the results are promising (thin  
475 orange lines). In a more complicate but realistic situation, the cooling rate, which is likely very  
476 different for the mantle xenolith and abyssal peridotite, may vary as a function of time. Hence it  
477 may be possible to deduced cooling rate through detailed modeling of the spoon-shaped opx/cpx  
478 REE patterns in residual peridotites, a subject that we will pursue in the near future.

### 479 **4.3. Mantle source composition**

480 The starting mantle composition (DMM vs. PM) affects our inversion results. The depleted  
481 MORB mantle or DMM (e.g., Workman and Hart, 2005) has been widely used in REE modeling  
482 of abyssal peridotites. In their original studies of mantle xenoliths, Liu et al. (2012) and Harvey et  
483 al. (2012) anchored their major and trace element data to the primitive mantle of McDonough and  
484 Sun (1995), whereas Quinn et al (2018) used DMM and HREE in their samples to infer the extent  
485 of melting. We used the primitive mantle of McDonough and Sun (1995) as the starting mantle  
486 composition in our inversion of the mantle xenolith data. Composition of the mantle source is  
487 unlikely homogeneous, even for a suite of depleted samples from the same locality. Liu et al. (2012)  
488 reported Nd and Hf isotopic compositions of cpx for the three North China Craton samples (YY-  
489 26, YY-40B, and YY-42) included in this study. They found that samples YY-40B and YY-42  
490 have considerably higher  $^{143}\text{Nd}/^{144}\text{Nd}$  and  $^{176}\text{Hf}/^{177}\text{Hf}$  ratios than sample YY-26 and suggested that  
491 samples such as YY-26 might be affected by melt addition via melt-rock interaction. In Section  
492 3.1, we showed that REE patterns in the bulk sample, cpx, and opx in YY-26 can be well

493 reproduced by our melting followed by subsolidus reequilibration model using PM as the starting  
494 mantle composition (Fig. S5). The misfit is LREE in opx, which is likely resulted from incomplete  
495 reequilibration at a low temperature ( $T_{REE} = 889$  °C). The higher  $^{143}\text{Nd}/^{144}\text{Nd}$  and  $^{176}\text{Hf}/^{177}\text{Hf}$  ratios  
496 in samples YY-40B and YY-42 suggest that these samples may have derived from a more depleted  
497 mantle source. To test this hypothesis, we run MCMC simulations for samples YY-40B and YY-  
498 42 using DMM as our starting mantle composition. The results are summarized in Supplementary  
499 Table S2 and Fig. S5: the fits to sample YY-40B are slightly improved as the sum of Pearson's  
500 Chi-squares decreases from 1.76 (PM) to 1.68 (DMM), whereas no improvement is observed for  
501 YY-42 as the sum of Pearson's Chi-squares increases from 0.62 (PM) to 1.21 (DMM). In fact,  
502 inversion of the remaining 7 xenolith samples with DMM starting composition leads to moderate  
503 to significant reduction in the quality of fits to the observed REE patterns (i.e., the sum of Pearson's  
504 Chi-squares has increased, Fig. S5). This intriguing result suggests that composition of PM is more  
505 suitable for modeling REE depletion in residual mantle xenoliths, although the number of samples  
506 included in this study is rather small. Given the slight improvement of fits to sample YY-40B using  
507 DMM starting mantle composition, we include inversion results with DMM starting composition  
508 in our discussion (two points connected by red dashed lines in Figs. 7a, 8a, 8c, and 9 below).

509         Composition of the average DMM is a convenient common start point in modeling REE  
510 depletion in abyssal peridotites. According to Warren et al. (2009),  $^{143}\text{Nd}/^{144}\text{Nd}$  ratios in cpx in the  
511 4 samples from SWIR (Van7-85-42, Van7-85-47, Van7-85-49, and Van7-96-38) are more similar  
512 to the depleted endmember of DMM (D-DMM) of Workman and Hart (2005) than the average  
513 DMM (see Fig. 5a in Warren et al., 2009). Intrigued, we run MCMC simulations again for the 4  
514 samples using REE + Y in the D-DMM of Workman and Hart (2005) as starting mantle  
515 composition. The results are presented in supplementary Fig. S9: the fits to the observed REE in  
516 the bulk, cpx, and opx are slightly improved as the sums of Pearson's Chi-squares for the 4 samples  
517 are all reduced. The small improvement is probably due to the fact that concentration differences  
518 between D-DMM and DMM of Workman and Hart (2005) are small. As we discussed in Section  
519 4.1, concentrations of Pr to Eu in sample Van7-96-38 are underestimated in our models. It is  
520 possible that the starting mantle for Van7-96-38 is more depleted than D-DMM. Existence of ultra-  
521 depleted mantle domains have been proposed for magma genesis beneath mid-ocean ridges based  
522 on Os, Nd, and Hf isotope ratios in residual peridotites and olivine-hosted melt inclusions (e.g.,  
523 Liu et al., 2008; Stracke et al., 2011, 2019; Sanfilippo et al., 2019). The mantle source composition

524 for residual abyssal peridotites such as the ones examined in this study is likely more variable than  
525 that represented by the DMM model of Workman and Hart (2005). More study is needed to  
526 quantify the abundances of REE and other trace elements in these extremely depleted mantle  
527 sources.

#### 528 **4.4. Mantle source mode**

529 The starting mantle mode also affects fitting results. Our original purpose of exploring 3~6%  
530 variations in cpx and opx modes in the starting lherzolitic mantle was to understand the large  
531 variations in mineral modal abundance observed in the mantle xenoliths and abyssal peridotites  
532 included in this study, as such variations cannot be produced by melting a single mantle source. It  
533 turns out that the quality of fits to the bulk REE in the mantle xenoliths and abyssal peridotites are  
534 not very sensitive to the starting mantle mode, albeit a trade-off between cpx mode in the starting  
535 mantle and the inferred degree of melting (Section 3.1). This is explained by the very similar bulk  
536 REE partition coefficients for the three starting mantle modes: they are subparallel to each other  
537 in the spider diagram (see supplementary Fig. S10). Hence one cannot use bulk REE in residual  
538 peridotite to discriminate starting mantle mode. However, REE abundances in residual cpx and  
539 opx are sensitive to starting mantle mode for the mantle xenoliths and abyssal peridotites. This is  
540 due simply to mass balance and temperature-dependent opx/cpx and ol/cpx REE partition  
541 coefficients (Eqs. 5 and 6). During subsolidus reequilibration in a closed system (i.e., for a constant  
542  $C_s$  in Eq. 5), concentrations of REE in opx and ol in lherzolite or harzburgite decrease with the  
543 decrease of temperature, whereas concentrations of REE in cpx increase. At a given temperature,  
544 the change of concentration depends on mineral mode (see Fig. 6 in Sun and Liang, 2014) which  
545 is sensitive to the starting mantle mode and the melting reaction. During subsolidus reequilibration,  
546 cpx and opx modes and major element compositions also change due to pyroxene exsolution and  
547 subsolidus reaction among the mantle minerals, which complicates the application of Eq. 6. A  
548 preliminary pMELTS-based study suggests that these major element effects are small to moderate  
549 on REE re-distribution in peridotites (Yao, 2015). Results from this study suggest that the mineral  
550 mode in the starting mantle is not homogeneous. This is consistent with the scattered correlations  
551 between the bulk MgO and incompatible major and minor elements (CaO, Al<sub>2</sub>O<sub>3</sub>, Na<sub>2</sub>O, and TiO<sub>2</sub>)  
552 in the mantle xenoliths and abyssal peridotites (supplementary Figs. S3a and S4a).

#### 553 **4.5. Comparing melting parameters derived from REE in the bulk and REE in cpx**

554 In general, degrees of melting based on MCMC inversion of REE + Y in the bulk samples  
555 (designated as  $F_{bulk}$  hereafter) and cpx alone ( $F_{cpx}$ ) are positively correlated (Fig. 7). Figure 7a  
556 compares our estimated  $F_{bulk}$  with  $F_{cpx}$  for the nine xenoliths. Samples CK-2 (Coast Ranges of  
557 central California, Quinn et al., 2018) and ET80 (East African Rift, Bedini and Bodinier, 1999)  
558 are considerably more fertile in terms of spinel Cr# and contain 12.4% and 15.8% cpx, respectively.  
559 Hence REE + Y in cpx in these two samples should be less affected by subsolidus redistribution.  
560 Indeed, the calculated degrees of melting for CK-2 and ET80 based on the multi-mineral  
561 disequilibrium melting model (3.7% and 3.9%) are essentially the same as that derived from HREE  
562 in cpx (2.9% and 4.2%, Supplementary Table S2). Nonetheless, light and middle REE in opx in  
563 these samples are strongly affected by subsolidus redistribution, which is consistent with their low  
564  $T_{REE}$  (964°C and 952°C, respectively). The remaining seven samples are more depleted. Except  
565 sample YY-42, their inverted  $F_{bulk}$  are 2~6% higher than  $F_{cpx}$ . Sample YY-42 from North China  
566 Craton (Liu et al., 2012) has the lowest cpx mode (4%, a harzburgite), the highest spinel Cr#, and  
567 the second highest  $F_{bulk}$  (19%) among the nine xenolith samples included in this study. This is in  
568 contrast to the rather small  $F_{cpx}$  for this sample (11%, Table S2). Given its very refractory nature,  
569 we suspect that a large fraction of cpx in this sample may have derived from exsolution of opx  
570 after melting. Hence the degree of melting inferred from cpx alone in this sample is not meaningful.  
571 Caution should be exercised when inferring extent of melting using REE abundance in cpx in  
572 harzburgitic mantle xenoliths.

573 Given the relatively high  $T_{REE}$  recorded by the 12 abyssal peridotite samples (Fig. 2) and  
574 the limited extent of subsolidus redistribution of REE between cpx and opx (Section 3.2), it is not  
575 surprising that the inferred degrees of melting based REE in the bulk samples are only slightly  
576 higher than those derived from REE in cpx alone (Fig. 7b). The maximum difference is only 2.2%,  
577 which is in general agreement with the assessment of Sun and Liang (2014). Hence in the absence  
578 of bulk REE data, one can use REE in cpx to infer the extent of melting experienced by residual  
579 abyssal peridotites.

580 There are considerable uncertainties in the inverted disequilibrium parameter for La in cpx  
581 ( $\epsilon_{cpx}^{1300}$ ) and the melt suction rate ( $\mathbb{R}$ ) (Supplementary Table S2). Excluding melting parameters  
582 from cpx-alone inversion for sample YY-42, inverted disequilibrium parameters for La in cpx  
583 derived from REE in the bulk and REE in cpx alone are correlated, whereas the melt suction rates

584 are uncorrelated for the eight mantle xenoliths (Figs. 8a and 8c). It also appears that inverted  
585 disequilibrium parameter for La in cpx and melt suction rate derived from REE in the bulk are  
586 lower than values derived from REE in cpx alone for the abyssal peridotites (Figs. 8b and 8d),  
587 although exceptions are noted (sample Dr23-3-2). Potential causes for the apparent differences  
588 between the xenolith and abyssal peridotite samples include difference in tectonic setting (i.e.,  
589 thermal and magmatic histories), difference in melting path and melting reaction, and/or nonlinear  
590 trade-off between the two melting parameters in the presence of inaccurate trace element data.  
591 More work is needed to confirm and sort out the differences noted.

#### 592 **4.6. Variations of the melting parameters derived from bulk REE with key melting indices**

593 Chromian spinel has been widely used in studies of abyssal peridotites and peridotites from  
594 other tectonic settings (e.g., Dick and Bullen, 1984). Hellebrand et al (2001) showed that spinel  
595 Cr# in residual abyssal peridotites are strongly and inversely correlated with HREE abundances in  
596 cpx in the peridotites and developed empirical equations relating degree of melting to spinel Cr#  
597 for abyssal peridotites. Figure 9a shows the positive correlation between our inverted  $F_{bulk}$  and  
598 spinel Cr# for the xenolith and abyssal peridotite samples included in this study. The abyssal  
599 peridotites are bracketed by the batch melting and perfect fractional melting trends of Hellebrand  
600 et al. (2011). However, due to the low spinel Cr#, the mantle xenolith data are mostly plotted below  
601 the batch melting trend. The latter may in part due to subsolidus redistribution of Cr and Al in  
602 spinel peridotite (e.g., Viogt and von der Handt, 2011). Caution should be exercised when inferring  
603 extent of melting using Cr# of spinel in mantle xenoliths.

604 Our inferred degrees of melting for the mantle xenoliths and abyssal peridotites are  
605 consistent with the observed variation trends of the major and minor elements in the samples. For  
606 example, with increasing degree of melting, MgO content in the bulk residue increases from the  
607 starting DMM or PM (Fig. 9b), whereas CaO, Al<sub>2</sub>O<sub>3</sub>, Na<sub>2</sub>O, and TiO<sub>2</sub> contents in the bulk sample  
608 decrease (Figs. S3c and S4c). The scatteredness of the data shown in Figs. 9b, S3c and S4c can be  
609 attributed to variations in mineral modes, hence major element composition, in the starting mantle.

610

#### 611 **5. What have we learned from REE abundances in residual peridotites?**

612 LREE depleted spinel peridotites are generally interpreted as residues of mantle melting.  
613 Through case studies of carefully selected residual spinel peridotites from two distinct tectonic  
614 settings we have demonstrated the advantages of using REE abundances in both the bulk rock and  
615 constituent minerals (cpx and opx) in deducing magmatic and thermal history of the peridotites.  
616 REE abundances in bulk residual peridotites are well-suited for studying melting process, provided  
617 their concentrations are accurately determined, and grain size and mineral mode are known. As a  
618 first application, we kept opx and cpx grain size ratio constant in our MCMC inversion. This is  
619 likely a simplification, as we do not know how grain sizes of cpx and opx vary during mantle  
620 melting and subsolidus reequilibration. LREE in opx and HREE in cpx are more susceptible to  
621 subsolidus redistribution. The extent of redistribution depends on cpx and opx abundances in the  
622 sample and thermal history experienced by the peridotite. We have shown that, by modeling  
623 subsolidus redistribution of REE between opx and cpx after melting, it is possible to discriminate  
624 mineral mode of the starting mantle. HREE in cpx in less primitive spinel lherzolite and  
625 harzburgite from continental cratons are significantly reset by subsolidus reequilibration over  
626 geologic time. We do not recommend the use of REE in cpx alone to study mantle melting process  
627 in such samples. The harzburgite YY-42 from North China Craton (Liu et al., 2012) is an extreme  
628 example. In the absence of REE abundance in opx, REE in cpx in residual abyssal peridotites can  
629 be used to infer the degree of melting of samples that experienced small to moderate extent of  
630 melting. HREE in highly depleted harzburgite may be affected by subsolidus reequilibration. By  
631 modeling REE abundances in the bulk and constituent cpx and opx, it is also possible to  
632 discriminate starting mantle composition. We find that composition of the primitive mantle is more  
633 suitable for modeling REE depletion in cratonic mantle xenoliths, whereas composition of DMM  
634 is more suitable for modeling REE depletion in residual abyssal peridotites. REE patterns in some  
635 of the isotopically more depleted abyssal peridotites such as the four samples from SWIR (Warren  
636 et al., 2009) can be better explained by a starting mantle that is more depleted than the average  
637 DMM.

638 The mantle xenoliths and residual abyssal peridotites examined in this study are a small  
639 fraction of xenolith samples (9 out of 71) and abyssal peridotite samples (12 out of 60) analyzed  
640 in the original studies cited in Sections 3.1 and 3.2. To focus on REE depletion in the bulk  
641 peridotite produced by partial melting, we exclude samples that have LREE enriched patterns,  
642 samples that may have been affected by melt addition, and samples that exhibit disequilibrium

643 partitioning in HREE between opx and cpx. In spite of our conservative approach in sample  
644 selection, we find that the composition and mode of the starting mantle are still not homogeneous  
645 for these two groups of highly selective mantle peridotites. It is well known that the upper mantle  
646 is chemically (e.g., enriched vs. depleted) and lithologically (e.g., peridotite vs. pyroxenite)  
647 heterogeneous. Results from the present study suggests that the endmember of the depleted  
648 peridotitic upper mantle is also modally heterogeneous. A modally heterogeneous starting mantle  
649 provides a simple explanation for the large variations of mineral mode observed in peridotitic  
650 mantle xenoliths and abyssal peridotites, and may have important implications for the  
651 interpretation of geophysical data.

652         Finally, we note that the methodology developed in this study can also be applied to other  
653 trace elements in residual peridotites, provided their diffusion in and partitioning between mantle  
654 minerals are well characterized. A potential target is the high field strength elements. Spoon- or  
655 U-shaped opx/cpx REE partitioning patterns are observed in all the abyssal peridotite samples  
656 included in this study. Four of the nine mantle xenoliths that have lower REE closure temperature  
657 also have spoon-shaped REE partitioning pattern. Through simple forward modeling, we have  
658 shown that the spoon- or U-shaped opx/cpx REE partitioning patterns can be produced by  
659 disequilibrium melting followed by diffusive exchange between cpx and opx at subsolidus state.  
660 It may be possible to deduce cooling rate and thermal history through detailed modeling of spoon-  
661 shaped opx/cpx REE partitioning patterns in mantle samples.

662

## 663 **ACKNOWLEDGEMENTS**

664         We thank Daniele Brunelli, Henry Dick, Jingao Liu, and Jessica Warren for useful  
665 discussion regarding grain size in peridotites. This work was supported by National Science  
666 Foundation grant EAR-1852088 and the China Scholarship Council (201806010079).

667

668 **APPENDIX A. GOVERNING EQUATIONS**

669 The non-modal disequilibrium melting model of Liang and Liu (2016) is intended for  
 670 modeling trace element fractionation during concurrent melting, channelized melting extraction,  
 671 and finite rate of crystal-melt chemical exchange in an upwelling steady-state melting column. In  
 672 terms of the degree of melting experienced by the solid matrix ( $F$ ), mass conservation equations  
 673 for a trace element in the interstitial melt ( $C_f$ ), residual solid ( $C_s$ ), individual mineral ( $C_s^j$ ) can be  
 674 written as:

$$675 \quad \varepsilon_{cpx}(1 - \mathbb{R})F \frac{dC_f}{dF} = \varepsilon_{cpx}(C_s^p - C_f) + \sum_{j=1}^N w_j \frac{R_j}{R_{cpx}} (C_s^j - k_j C_f) \quad (A1a)$$

$$676 \quad \varepsilon_{cpx} (1 - F) \frac{dC_s}{dF} = \varepsilon_{cpx} (C_s - C_s^p) - \sum_{j=1}^N w_j \frac{R_j}{R_{cpx}} (C_s^j - k_j C_f) \quad (A1b)$$

$$677 \quad \varepsilon_{cpx} (1 - F) \frac{dC_s^j}{dF} = - \frac{R_j}{R_{cpx}} (C_s^j - k_j C_f) \quad (A1c)$$

678 where  $k_j$  is the partition coefficient between mineral  $j$  and melt for the element of interest;  $\mathbb{R}$  is  
 679 the dimensionless melt suction rate defined as the fraction of melt removed from the residual solid  
 680 (to a nearby channel) relative to the amount of melt produced by melting (Iwamori, 1994; Liang  
 681 and Peng, 2010);  $\varepsilon_{cpx}$  is the disequilibrium parameter for a trace element in cpx;  $C_s^p$  is the  
 682 concentration of bulk solid calculated according to melting reaction; and  $w_j$  is the weight fraction  
 683 of mineral  $j$  in residual solid. The latter three parameters are defined as follows:

$$684 \quad \varepsilon_{cpx} = \frac{\Gamma}{\rho_s(1-\phi_f)R_{cpx}} \quad (A1d)$$

$$685 \quad C_s^p = \sum_{j=1}^N w_j^p C_s^j \quad (A1e)$$

$$686 \quad w_j = \frac{w_j^0 - w_j^p F}{1 - F} \quad (A1f)$$

687 where  $\Gamma$  is the melting rate;  $\rho_s$  is the density of the bulk solid;  $\phi_f$  is the volume fraction of the  
 688 melt in the residue;  $w_j^0$  is the weight fraction of mineral  $j$  at the onset of the melting; and  $w_j^p$  is the  
 689 weight fraction of mineral  $j$  participating in the melting reaction. Equations (A1a)-(A1c) can be  
 690 further simplified by assuming that the interstitial melt and olivine and spinel are location chemical  
 691 equilibrium. The mass conservation equations become:

$$692 \left( \varepsilon_{\text{cpx}}(1 - \mathbb{R})F + \varepsilon_{\text{cpx}}(1 - F)(w_{\text{ol}}k_{\text{ol}} + w_{\text{sp}}k_{\text{sp}}) \right) \frac{dC_f}{dF} =$$

$$693 \varepsilon_{\text{cpx}}(C_s^p - C_f) + w_{\text{cpx}}(C_s^{\text{cpx}} - k_{\text{cpx}}C_f) + w_{\text{opx}} \frac{R_{\text{opx}}}{R_{\text{cpx}}} (C_s^{\text{opx}} - k_{\text{opx}}C_f) \quad (\text{A2a})$$

$$694 \varepsilon_{\text{cpx}}(1 - F) \frac{dC_s^{\text{cpx}}}{dF} = -(C_s^{\text{cpx}} - k_{\text{cpx}}C_f) \quad (\text{A2b})$$

$$695 \varepsilon_{\text{cpx}}(1 - F) \frac{dC_s^{\text{opx}}}{dF} = -\frac{R_{\text{opx}}}{R_{\text{cpx}}} (C_s^{\text{opx}} - k_{\text{opx}}C_f) \quad (\text{A2c})$$

$$696 C_s^p = w_{\text{cpx}}^p C_s^{\text{cpx}} + w_{\text{opx}}^p C_s^{\text{opx}} + w_{\text{ol}}^p k_{\text{ol}} C_f + w_{\text{sp}}^p k_{\text{sp}} C_f \quad (\text{A2d})$$

697 Concentration of REE in the bulk residue can be calculated using the expression:

$$698 C_s = \sum w_j C_s^j = w_{\text{cpx}} C_s^{\text{cpx}} + w_{\text{opx}} C_s^{\text{opx}} + w_{\text{ol}} k_{\text{ol}} C_f + w_{\text{sp}} k_{\text{sp}} C_f \quad (\text{A2e})$$

699 Equations (A2a)-(A2c) are closed by the following boundary conditions at the bottom of the  
 700 melting column ( $F = 0$ ):

$$701 C_f(0) = \frac{\varepsilon_{\text{cpx}} k_p + k_0}{k_0(\varepsilon_{\text{cpx}} + k_0)} C_s^0 \quad (\text{A2f})$$

$$702 C_s^{\text{cpx}}(0) = \frac{k_{\text{cpx}}}{k_0} C_s^0 \quad (\text{A2g})$$

$$703 C_s^{\text{opx}}(0) = \frac{k_{\text{opx}}}{k_0} C_s^0 \quad (\text{A2h})$$

704 where  $k_0$  is the bulk solid–melt partition coefficient at the onset of melting; and  $k_p$  is the bulk  
 705 solid–melt partition coefficient according to the melting reaction. Equation (A2f) is based on the  
 706 analysis of Liang and Liu (2016). Equations (A2a)-(A2c) are a set of coupled ordinary differential

707 equations and can be solved numerically using standard methods. In this study, we solve these  
708 equations using the routine ODEIENT in Python.

709

710

711 **References**

- 712 Agranier A. and Lee C. T. A. (2007) Quantifying trace element disequilibria in mantle xenoliths  
713 and abyssal peridotites. *Earth Planetary Science Letter* **257**, 290–298.
- 714 Anders E. and Grevsse N. (1989) Abundances of the elements: Meteoritic and solar. *Geochimica  
715 et Cosmochimica Acta* **53**, 197–214.
- 716 Baker M. B. and Stolper E. M. (1994) Determining the composition of high–pressure mantle  
717 melts using diamond aggregates. *Geochimica et Cosmochimica Acta* **58**, 2811–2827.
- 718 Baker M. B. and Stolper E. M. (1994) Determining the composition of high–pressure mantle  
719 melts using diamond aggregates. *Geochimica et Cosmochimica Acta* **58**, 2811–  
720 2827. Bedini R. and Bodinier J. L. (1999) Distribution of incompatible trace elements  
721 between the constituents of spinel peridotite xenoliths: ICP–MS data from the East  
722 African Rift. *Geochimica et Cosmochimica Acta* **63**, 3883–3900.
- 723 Bodinier J. L., Vasseur G., Vernieres J., Dupuy C. and Fabries J. (1990) Mechanisms of Mantle  
724 Metasomatism: Geochemical Evidence from the Lherz Orogenic Peridotite. *Journal of  
725 Petrology* **31**, 597–628.
- 726 Brey G. and Kohler T. (1990) Geothermobarometry in four–phase lherzolites II. New  
727 thermobarometers, and practical assessment of existing thermobarometers. *Journal of  
728 Petrology* **31**, 1353–1378.
- 729 Brunelli D. and Seyler M. (2010) Asthenospheric percolation of alkaline melts beneath the St.  
730 Paul region (Central Atlantic Ocean). *Earth Planetary Science Letter* **289**, 393–405.
- 731 Brunelli D., Paganelli E. and Seyler M. (2014) Percolation of enriched melts during incremental  
732 open–system melting in the spinel field: a REE approach to abyssal peridotites from the  
733 Southwest Indian Ridge. *Geochimica et Cosmochimica Acta* **127**, 190–203.
- 734 Brunelli D., Seyler M., Cipriani A., Ottolini L. and Bonatti E. (2006) Discontinuous melt  
735 extraction and weak refertilization of mantle peridotites at the Vema Lithospheric Section  
736 (Mid– Atlantic Ridge). *Journal of Petrology* **47**, 745–771.
- 737 Cherniak D. J. (2015) Nb and Ta diffusion in titanite. *Chemical Geology* **413**, 44–50.
- 738 Cherniak D. J. and Liang Y. (2007) Rare earth element diffusion in natural enstatite. *Geochimica  
739 et Cosmochimica Acta* **71**, 1324–1340.
- 740 D’Errico M. E., Warren J. M. and Godard M. (2016) Evidence for chemically heterogeneous  
741 Arctic mantle beneath the Gakkel Ridge. *Geochimica et Cosmochimica Acta* **174**, 291–  
742 312.
- 743 Dick H. J. B. and Bullen T. (1984) Chromian spinel as a petrogenetic indicator in abyssal and  
744 alpine–type peridotites and spatially associated lavas. *Contributions to Mineralogy and  
745 Petrology* **86**, 54–76.

- 746 Dygert N. and Liang Y. (2015) Temperatures and cooling rates recorded in REE in coexisting  
747 pyroxenes in ophiolitic and abyssal peridotites. *Earth Planetary Science Letter* **420**, 151–  
748 161.
- 749 Dygert N., Kelemen P. B. and Liang, Y. (2017) Spatial variations in cooling rate in the mantle  
750 section of the Samail ophiolite in Oman: Implications for formation of lithosphere at  
751 mid-ocean ridges. *Earth and Planetary Science Letters* **465**, 134–144.
- 752 Ghiorso M. S., Hirschmann M. M., Reiners P. W. and Kress V. C. (2002) The pMELTS: a  
753 revision of MELTS for improved calculation of phase relations and major element  
754 partitioning related to partial melting of the mantle to 3 GPa. *Geochemistry, Geophysics,*  
755 *Geosystems* **3**, 1–35.
- 756 Harvey J., Yoshikawa M., Hammond S. J. and Burton K. W. (2012) Deciphering the trace  
757 element characteristics in Kilauea Hole peridotite xenoliths: melt-rock interaction  
758 and metasomatism beneath the Rio Grande Rift, SW USA. *Journal of Petrology* **53**, 1709–  
759 1742.
- 760 Hellebrand E. and Snow J. E. (2003) Deep melting and sodic metasomatism underneath the  
761 highly oblique-spreading Lena Trough (Arctic Ocean). *Earth and Planetary Science*  
762 *Letters* **216**, 283–299.
- 763 Hellebrand E., Snow J. E., Dick H. J. B. and Hofmann A. W. (2001) Coupled major and trace  
764 elements as indicators of the extent of melting in mid-ocean-ridge peridotites. *Nature*  
765 **410**, 677–681.
- 766 Hellebrand E., Snow J. E., Hoppe P. and Hofmann A. W. (2002) Garnet-field melting and late-  
767 stage refertilization in ‘residual’ abyssal peridotites from the Central Indian Ridge.  
768 *Journal of Petrology* **43**, 2305–2338.
- 769 Hellebrand E., Snow J. E., Mostefaoui S. and Hoppe P. (2005) Trace element distribution  
770 between orthopyroxene and clinopyroxene in peridotites from the Gakkel Ridge: a SIMS  
771 and NanoSIMS study. *Contributions to Mineralogy and Petrology* **150**, 486–504.
- 772 Iwamori H. (1994)  $^{238}\text{U}$ – $^{230}\text{Th}$ – $^{226}\text{Ra}$  and  $^{235}\text{U}$ – $^{231}\text{Pa}$  disequilibria produced by mantle melting  
773 with porous and channel flows. *Earth and Planetary Science Letters* **125**, 1–16.
- 774 Johnson K. T. M. (1998) Experimental determination of partition coefficients for rare earth and  
775 high-field-strength elements between clinopyroxene, garnet, and basaltic melt at high  
776 pressures. *Contributions to Mineralogy and Petrology* **133**, 60–68.
- 777 Johnson K. T. M. and Dick H. J. B. (1992) Open system melting and temporal and spatial  
778 variation of peridotite and basalt at the Atlantis II Fracture Zone. *Journal of Geophysical*  
779 *Research: Solid Earth* **97**, 9219–9241.
- 780 Johnson K. T. M., Dick H. J. B. and Shimizu N. (1990) Melting in the oceanic upper mantle: an  
781 ion microprobe study of diopsides in abyssal peridotites. *Journal of Geophysical*  
782 *Research: Solid Earth* **95**, 2661–2678.

- 783 Kelemen P. B., Hirth G., Shimizu N., Spiegelman M. and Dick H. J. B. (1997) A review of melt  
784 migration processes in the adiabatically upwelling mantle beneath oceanic spreading  
785 ridges. *Philosophical Transactions: Mathematical, Physical and Engineering Science* **355**,  
786 283–318.
- 787 Kinzler R. J. and Grove T. L. (1992) Primary magmas of mid-ocean ridge basalts 1. Experiments  
788 and methods. *Journal of Geophysical Research: Solid Earth* **97**, 6885–6906.
- 789 Lee C. T. A., Harbert A. and Leeman W. P. (2007) Extension of lattice strain theory to  
790 mineral/mineral rare-earth element partitioning: An approach for assessing  
791 disequilibrium and developing internally consistent partition coefficients between olivine,  
792 orthopyroxene, clinopyroxene and basaltic melt. *Geochimica et Cosmochimica Acta* **71**,  
793 481–496.
- 794 Liang Y. (2003) On the thermo-kinetic consequences of slab melting. *Geophysical Research*  
795 *Letter* **30**, 2270. [http://dx.doi.org/ 10.1029/2003GL018969](http://dx.doi.org/10.1029/2003GL018969).
- 796 Liang Y. (2014) Time scales of diffusive re-equilibration in bi-mineralic systems with and  
797 without a fluid or melt phase. *Geochimica et Cosmochimica Acta* **132**, 274–287.
- 798 Liang Y. and Liu B. (2016) Simple models for disequilibrium fractional melting and batch  
799 melting with application to REE fractionation in abyssal peridotites. *Geochimica et*  
800 *Cosmochimica Acta* **173**, 181–197.
- 801 Liang Y. and Peng Q. (2010) Non-modal melting in an upwelling mantle column: steady-state  
802 models with applications to REE depletion in abyssal peridotites and the dynamics of  
803 melt migration in the mantle. *Geochimica et Cosmochimica Acta* **74**, 321–339.
- 804 Liang Y., Sun C. and Yao L. (2013) A REE-in-two-pyroxene thermometer for mafic and  
805 ultramafic rocks. *Geochimica et Cosmochimica Acta* **102**, 246–260.
- 806 Liu B. and Liang Y. (2017) An introduction of Markov chain Monte Carlo method to  
807 geochemical inverse problems: Reading melting parameters from REE abundances in  
808 abyssal peridotites. *Geochimica et Cosmochimica Acta* **203**, 216–234.
- 809 Liu C.-Z., Snow J. E., Hellebrand E., Brugmann G., von der Handt A., Buchl A. and Hofmann  
810 A. W. (2008) Ancient, highly heterogeneous mantle beneath Gakkel ridge, Arctic Ocean.  
811 *Nature* **452**, 311–316.
- 812 Liu J., Carlson R. W., Rudnick R. L., Walker R. J., Gao S. and Wu F. (2012) Comparative Sr–  
813 Nd–Hf–Os–Pb isotope systematics of xenolithic peridotites from Yangyuan, North China  
814 Craton: additional evidence for a Paleoproterozoic age. *Chemical Geology* **332**, 1–14.
- 815 Lundstrom C. (2000) Models of U-series disequilibria generation in MORB: the effects of two  
816 scales of melt porosity. *Physics of the Earth and Planetary Interiors* **121**, 189–204.
- 817 McDonough W. F. and Sun S. S. (1995) The composition of the Earth. *Chemical Geology* **120**,  
818 223–253.

- 819 Navon O. and Stolper E. (1987) Geochemical consequences of melt percolation: the upper  
820 mantle as a chromatographic column. *The Journal of Geology* **95**, 285–307.
- 821 Niu Y. and He'kinian R. (1997) Spreading–rate dependence of the extent of mantle melting  
822 beneath ocean ridges. *Nature* **385**, 326– 329.
- 823 Quinn D. P., Saleeby J., Ducea M., Luffi P. and Asimow P. (2018) Late–Cretaceous con-  
824 struction of the mantle lithosphere beneath the central California coast revealed by  
825 Crystal Knob xenoliths. *Geochemistry, Geophysics, Geosystems* **19**, 3302–3346.
- 826 Salters V. J. M. and Dick H. J. B. (2002) Mineralogy of the mid– ocean–ridge basalt source from  
827 neodymium isotopic composition of abyssal peridotites. *Nature* **418**, 68–72.
- 828 Sambridge M. and Mosegaard K. (2002) Monte Carlo methods in geophysical inverse problems.  
829 *Reviews of Geophysics* **40**, 1009.
- 830 Sanfilippo A., Salters V., Tribuzio R. and Zanetti A. (2019) Role of ancient, ultra–depleted  
831 mantle in mid–ocean–ridge magmatism. *Earth Planetary Science Letter* **511**, 89–98.
- 832 Seyler M., Brunelli D., Toplis M. J. and Me'vel C. (2011) Multiscale chemical heterogeneities  
833 beneath the eastern Southwest Indian Ridge (52° E–68° E): Trace element compositions  
834 of along–axis dredged peridotites. *Geochemistry, Geophysics, Geosystems* **12**, Q0AC15,  
835 doi:10.1029/2011GC003585.
- 836 Shimizu N. (1998) The geochemistry of olivine–hosted melt inclusions in a FAMOUS basalt  
837 ALV519–4–1. *Physics of the Earth and Planetary Interiors* **107**, 183–201.
- 838 Stosch H. G. (1982) Rare earth element partitioning between minerals from anhydrous spinel  
839 peridotite xenoliths. *Geochimica et Cosmochimica Acta* **46**, 793–811.
- 840 Stracke A., Genske F., Berndt J. and Koornneef J. M. (2019) Ubiquitous ultra–depleted domains  
841 in Earth's mantle. *Nature Geoscience* **12**, 851–855.
- 842 Stracke A., Snow J. E., Hellebrand E., von der Handt A., Bourdon B., Birbaum K. and Günther,  
843 D. (2011) Abyssal peridotite Hf isotopes identify extreme mantle depletion. *Earth*  
844 *Planetary Science Letter* **308**, 359–368.
- 845 Sun C. and Liang, Y. (2014) An assessment of subsolidus re–equilibration on REE distribution  
846 among mantle minerals olivine, orthopyroxene, clinopyroxene, and garnet in peridotites.  
847 *Chemical Geology* **372**, 80–91.
- 848 Van Orman J. A., Grove T. L. and Shimizu N. (2001) Rare earth element diffusion in diopside;  
849 influence of temperature, pressure, and ionic radius, and an elastic model for diffusion in  
850 silicates. *Contributions to Mineralogy and Petrology* **141**, 687–703.
- 851 Van Orman J. A., Grove T. L. and Shimizu N. (2002) Diffusive fractionation of trace elements  
852 during production and transport of melt in Earth's upper mantle. *Earth Planetary Science*  
853 *Letter* **198**, 93–112.

- 854 Voigt M. and von der Handt A. (2011) Influence of subsolidus processes on the chromium  
855 number in spinel in ultramafic rocks. *Contributions to Mineralogy and Petrology* **162**,  
856 675–689.
- 857 Walter M. J. and Presnall D. C. (1994) Melting behavior of simplified lherzolite in the system  
858 CaO–MgO–Al<sub>2</sub>O<sub>3</sub>–SiO<sub>2</sub>–Na<sub>2</sub>O from 7 to 35 kbar. *Journal of Petrology* **35**, 329–359.
- 859 Wang C., Liang Y. and Xu W. (2015) On the significance of temperatures derived from major  
860 element and REE based two–pyroxene thermometers for mantle xenoliths from the North  
861 China Craton. *Lithos* **224–225**, 101–113.
- 862 Warren J. M. (2016) Global variations in abyssal peridotite compositions. *Lithos* **248–251**, 193–  
863 219.
- 864 Warren J. M., Shimizu N., Sakaguchi C., Dick H. J. B. and Nakamura E. (2009) An assessment  
865 of upper mantle heterogeneity based on abyssal peridotite isotopic compositions. *Journal*  
866 *of Geophysical Research* 114, B122023, doi:10.1029/2008JB006186.
- 867 Witt–Eickschen G. and O’Neill H. S. C. (2005) The effect of temperature on the equilibrium  
868 distribution of trace elements between clinopyroxene, orthopyroxene, olivine and spinel  
869 in upper mantle peridotite. *Chemical Geology* **221**, 65–101.
- 870 Workman R. K. and Hart S. R. (2005) Major and trace element composition of the depleted  
871 MORB mantle (DMM). *Earth Planetary Science Letter* **231**, 53–72.
- 872 Yao L. (2015) Closure Temperature and Closure Pressure in Bi–Mineralic Systems with  
873 Applications to REE–in–Two–Mineral Thermobarometers. Brown University Ph.D.  
874 thesis.
- 875 Yao L. and Liang Y. (2015) Closure temperature in cooling bi–mineralic systems: I. Definition  
876 and with application to REE–in–two–pyroxene thermometer. *Geochimica et*  
877 *Cosmochimica Acta* **162**, 137–150.
- 878

## 879 Figure Captions

880 Fig. 1. (a) Forward simulation of REE patterns in residual solid, clinopyroxene (cpx), and  
881 orthopyroxene (opx) after 6% disequilibrium melting followed by subsolidus  
882 reequilibration. The solid lines represent REE patterns calculated using the multi-mineral  
883 disequilibrium melting model and melting parameters of  $\varepsilon_{La}^{1300} = 0.01$  and  $R = 0.95$ . The  
884 dashed lines represent the recalculated REE concentrations in the two pyroxenes at 1100°C  
885 and 900°C. (b) Comparison of REE patterns in residual solid, clinopyroxene, and  
886 orthopyroxene after 6% disequilibrium melting for two choices of opx grain size. The solid  
887 lines represent the case of  $r_{cpx} = 1$  mm and the dashed lines are for  $r_{opx} = 5$  mm. The grain  
888 size of cpx is assumed to be 1 mm. Parameters used in this simulation are as same as in (a).  
889 The temperature-dependent cpx-opx partition coefficients are from Sun and Liang (2014).  
890 Concentrations of REE are normalized to CI chondrite using the values of Anders and  
891 Grevesse (1989).

892 Fig. 2. Comparison of the temperatures derived from the REE-in-two-pyroxene thermometer of  
893 Liang et al. (2013,  $T_{REE}$ ) and those calculated using the two-pyroxene thermometer of Brey  
894 and Kohler (1990,  $T_{BKN}$ ) for the 9 mantle xenoliths and 12 abyssal peridotites included in  
895 this study (see text for a list of the source of data). All calculations were performed  
896 assuming a pressure of 1.5 GPa.

897 Fig. 3. Modal abundances of clinopyroxene (cpx), orthopyroxene (opx), and olivine (ol) in mantle  
898 xenoliths (a) and abyssal peridotites (b) selected in this study. The magenta lines in (a) are  
899 calculated using the melting reaction of Baker and Stolper (1994):  $0.38 \text{ opx} + 0.71 \text{ cpx} +$   
900  $0.13 \text{ spinel} = 0.22 \text{ olivine} + 1 \text{ melt}$  and for three choices of starting mantle mode. The light  
901 grey area in (b) is based on Warren (2016) for residual abyssal peridotites from around the  
902 world. The magenta curves in (b) represent melting paths based on pMELTS with potential  
903 temperature of 1330 °C and 150 ppm water content and three choices of starting mantle  
904 mode. Sample legends are the same as in Fig. 2.

905 Fig. 4. Comparison between observed (circles) and model derived (curves) REE+Y patterns in the  
906 bulk and two pyroxenes in the xenolith sample CK-2 (Quinn et al., 2018). Simulation  
907 results for three starting mantle modes are shown in panels (a), (b), and (c). The grey solid  
908 curves are MCMC predictions and the red solid curve represents the best-fit of the bulk  
909 REE+Y data. The solid blue and green curves represent the calculated REE abundances in  
910 cpx and opx, respectively, based on the inversed melting parameters of the best-fit of the  
911 bulk data. The dashed blue and green curves represent the model predicted subsolidus REE  
912 abundances in cpx and opx at  $T = T_{REE}$ , calculated using the temperature-dependent cpx-  
913 opx partition coefficients of Sun and Liang (2014). The sum of Pearson's Chi-square ( $\chi_{sum}^2$ )  
914 is the sum of the Chi-squares of simulated bulk (red curve) and simulated cpx and opx after  
915 subsolidus re-equilibrium (dashed bulk and green curves). The open squares and black  
916 curve in (a) represent the cpx data and the best-fit result based on the cpx-alone melting  
917 model. For clarity, data from cpx-alone simulations were elevated by a factor of 5.  
918 Concentrations of REE are normalized to CI chondrite using the values of Anders and  
919 Grevesse (1989).

920 Fig. 5. Comparison between observed (circles) and model derived (curves) REE+Y patterns in the  
921 bulk and two pyroxenes in the abyssal peridotite sample Van7-85-49 (Warren et al., 2009).  
922 For a detailed explanation of symbols and curves, a reader is referred to the caption to Fig.  
923 4.

924 Fig. 6. Variations of the apparent opx-cpx REE partition coefficient as a function of REE ionic  
925 radius for the xenolith sample CK-2 (a) and abyssal peridotite Van7-85-49 (b). The yellow  
926 circles represent the measured data. The magenta and black curves represent the model  
927 predicted apparent partition coefficients at the end of melting and at the subsolidus  
928 temperature  $T = T_{REE}$ , respectively. The thin orange curves were calculated using a simple  
929 model for diffusive reequilibration between two minerals at the stated cooling rates (see  
930 text for details). The three dashed curves are the calculated opx-cpx REE partition  
931 coefficients using the model of Sun and Liang (2014).

932 Fig. 7. Comparison of the degree of melting derived from the cpx-alone inversion ( $F_{cpx}$ ) and the  
933 degree of melting derived from inversion of the bulk sample ( $F_{bulk}$ ) for the mantle xenoliths  
934 (a) and abyssal peridotites (b) selected in this study. The dashed lines and grey areas  
935 represent the 1:1 ratio within a  $\pm 2\%$  range. The red dashed line in (a) connects the inversion  
936 results of sample YY-40B with primitive mantle (PM) and the depleted MORB mantle  
937 (DMM) starting compositions. Error bars are based on MCMC simulations. Sample  
938 legends are the same as in Fig. 2.

939 Fig. 8. Comparison of disequilibrium parameters ( $\epsilon$ ) and melt suction rate ( $\mathcal{R}$ ) derived from the  
940 cpx-alone inversion and the bulk sample inversion for mantle xenoliths (a and c) and  
941 abyssal peridotites (b and d). Other details are the same as in Fig. 7.

942 Fig. 9. Variations of spinel Cr# (a) and bulk MgO content (b) as a function of the degree of melting  
943 for the mantle xenoliths and abyssal peridotites included in this study. The two dashed lines  
944 are based on the empirical expressions of Hellebrand et al. (2001) for fractional and batch  
945 melting. Symbols are the same as in Fig. 2.

**Figure 1**

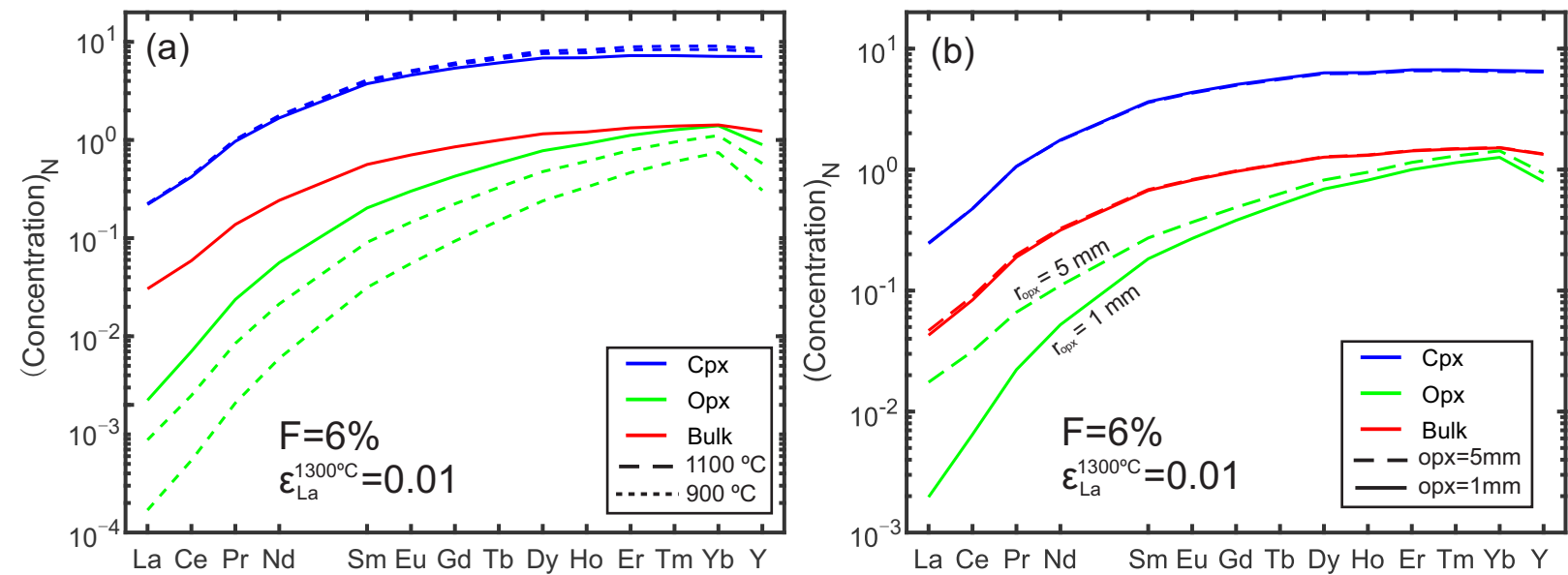


Fig. 1. (a) Forward simulation of REE patterns in residual solid, clinopyroxene (cpx), and orthopyroxene (opx) after 6% disequilibrium melting followed by subsolidus reequilibration. The solid lines represent REE patterns calculated using the multi-mineral disequilibrium melting model and melting parameters of  $\epsilon_{La}^{1300^\circ C} = 0.01$  and  $R = 0.95$ . The dashed lines represent the recalculated REE concentrations in the two pyroxenes at 1100°C and 900°C. (b) Comparison of REE patterns in residual solid, clinopyroxene, and orthopyroxene after 6% disequilibrium melting for two choices of opx grain size. The solid lines represent the case of  $r_{opx} = 1$  mm and the dashed lines are for  $r_{opx} = 5$  mm. The grain size of cpx is assumed to be 1 mm. Parameters used in this simulation are as same as in (a). The temperature-dependent cpx-opx partition coefficients are from Sun and Liang (2014). Concentrations of REE are normalized to CI chondrite using the values of Anders and Grevesse (1989).

Figure 2

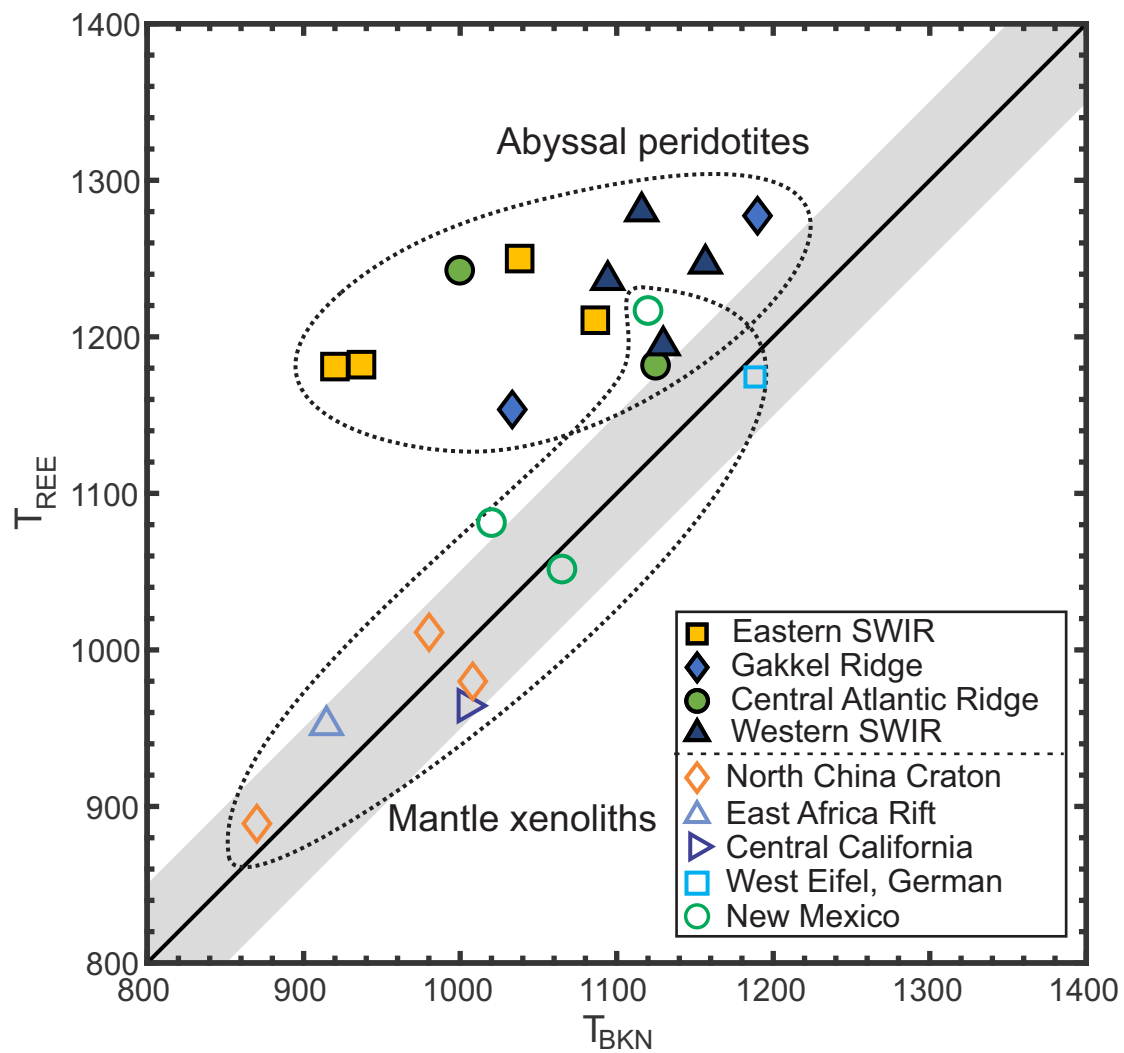


Fig. 2. Comparison of the temperatures derived from the REE-in-two-pyroxene thermometer of Liang et al. (2013,  $T_{REE}$ ) and those calculated using the two-pyroxene thermometer of Brey and Kohler (1990,  $T_{BKN}$ ) for the 9 mantle xenoliths and 12 abyssal peridotites included in this study (see text for a list of the source of data). All calculations were performed assuming a pressure of 1.5 GPa.

Figure 3

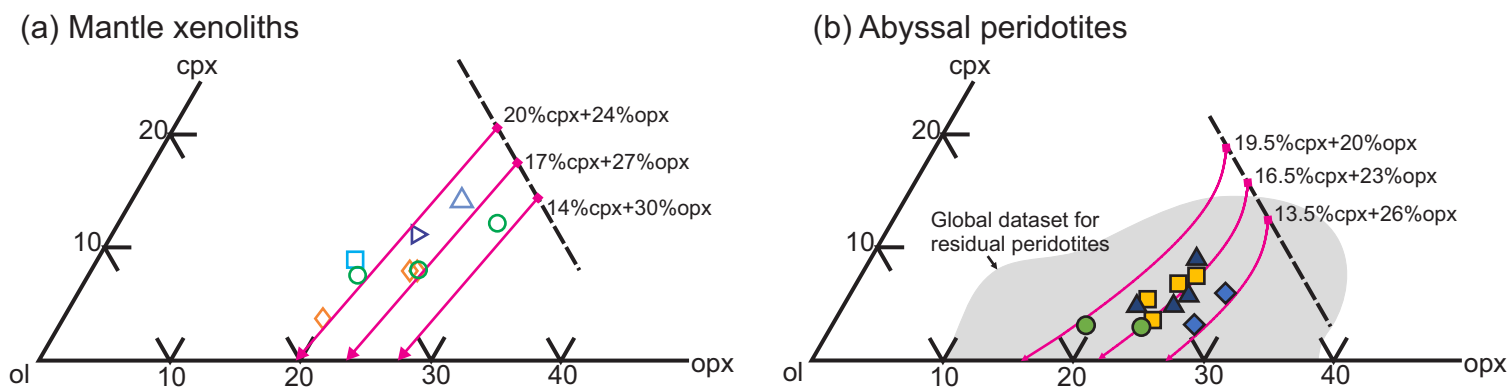


Fig. 3. Modal abundances of clinopyroxene (cpx), orthopyroxene (opx), and olivine (ol) in mantle xenoliths (a) and abyssal peridotites (b) selected in this study. The magenta lines in (a) are calculated using the melting reaction of Baker and Stolper (1994):  $0.38 \text{ opx} + 0.71 \text{ cpx} + 0.13 \text{ spinel} = 0.22 \text{ olivine} + 1 \text{ melt}$  and for three choices of starting mantle mode. The light grey area in (b) is based on Warren (2016) for residual abyssal peridotites from around the world. The magenta curves in (b) represent melting paths based on pMELTS with potential temperature of 1330 °C and 150 ppm water content and three choices of starting mantle mode. Sample legends are the same as in Fig. 2.

Figure 4

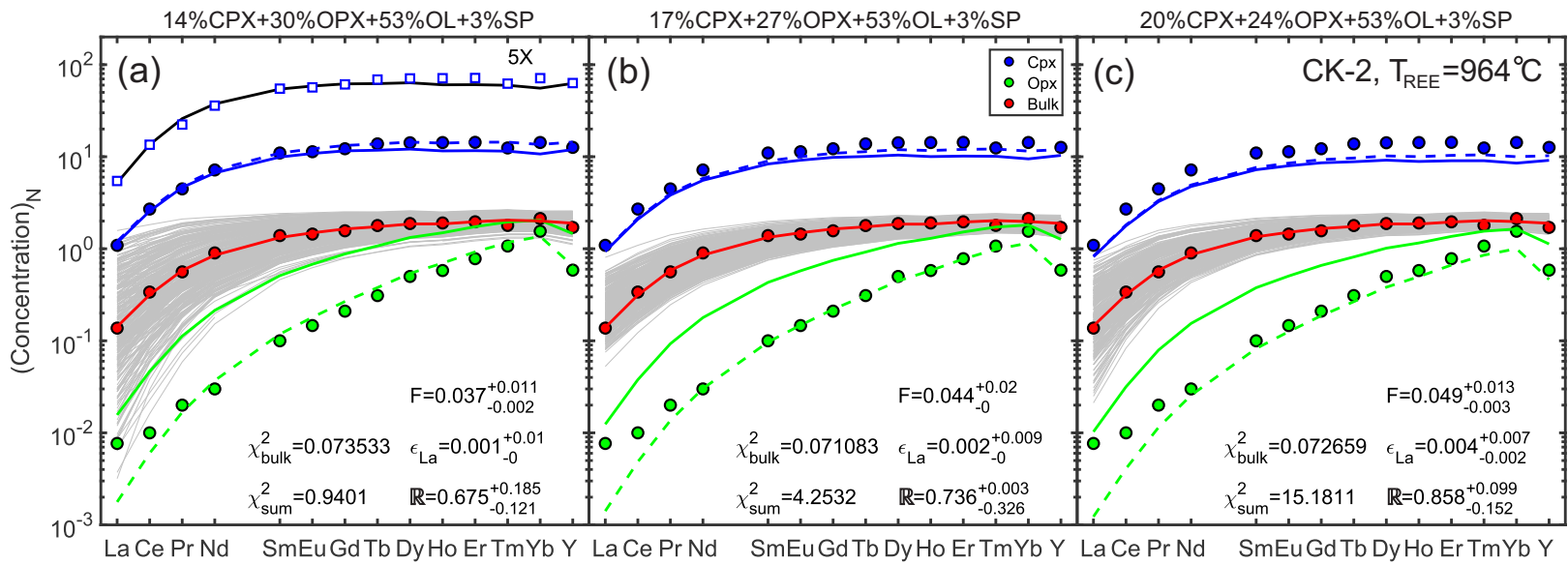


Fig. 4. Comparison between observed (circles) and model derived (curves) REE+Y patterns in the bulk and two pyroxenes in the xenolith sample CK-2 (Quinn et al., 2018). Simulation results for three starting mantle modes are shown in panels (a), (b), and (c). The grey solid curves are MCMC predictions and the red solid curve represents the best-fit of the bulk REE+Y data. The solid blue and green curves represent the calculated REE abundances in cpx and opx, respectively, based on the inverted melting parameters of the best-fit of the bulk data. The dashed blue and green curves represent the model predicted subsolidus REE abundances in cpx and opx at T = T<sub>REE</sub>, calculated using the temperature-dependent cpx-opx partition coefficients of Sun and Liang (2014). The sum of Pearson's Chi-square ( $\chi_{\text{sum}}^2$ ) is the sum of the Chi-squares of simulated bulk (red curve) and simulated cpx and opx after subsolidus re-equilibrium (dashed bulk and green curves). The open squares and black curve in (a) represent the cpx data and the best-fit result based on the cpx-alone melting model. For clarity, data from cpx-alone simulations were elevated by a factor of 5. Concentrations of REE are normalized to CI chondrite using the values of Anders and Grevesse (1989).

**Figure 5**

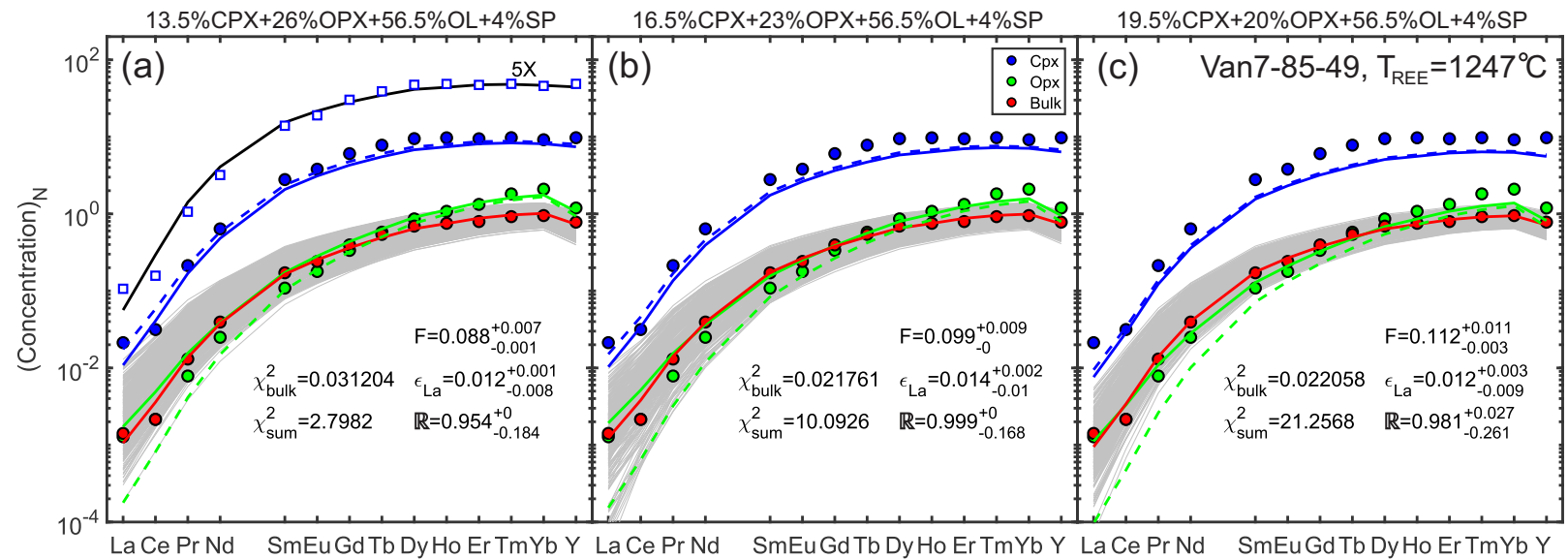


Fig. 5. Comparison between observed (circles) and model derived (curves) REE+Y patterns in the bulk and two pyroxenes in the abyssal peridotite sample Van7-85-49 (Warren et al., 2009). For a detailed explanation of symbols and curves, a reader is referred to the caption to Fig. 4.

Figure 6

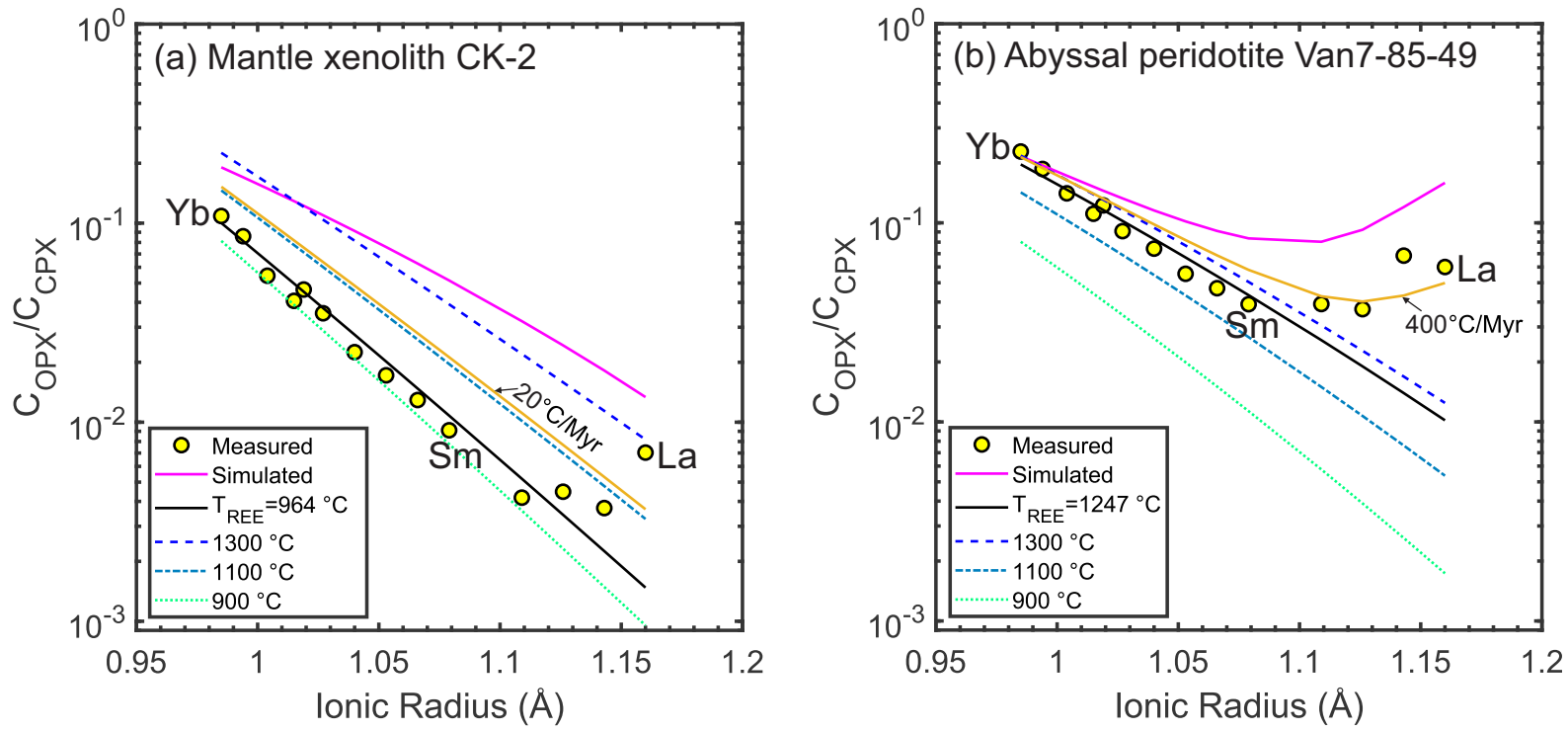


Fig. 6. Variations of the apparent opx-cpx REE partition coefficient as a function of REE ionic radius for the xenolith sample CK-2 (a) and abyssal peridotite Van7-85-49 (b). The yellow circles represent the measured data. The magenta and black curves represent the model predicted apparent partition coefficients at the end of melting and at the subsolidus temperature  $T = T_{\text{REE}}$ , respectively. The thin orange curves were calculated using a simple model for diffusive reequilibration between two minerals at the stated cooling rates (see text for details). The three dashed curves are the calculated opx-cpx REE partition coefficients using the model of Sun and Liang (2014).

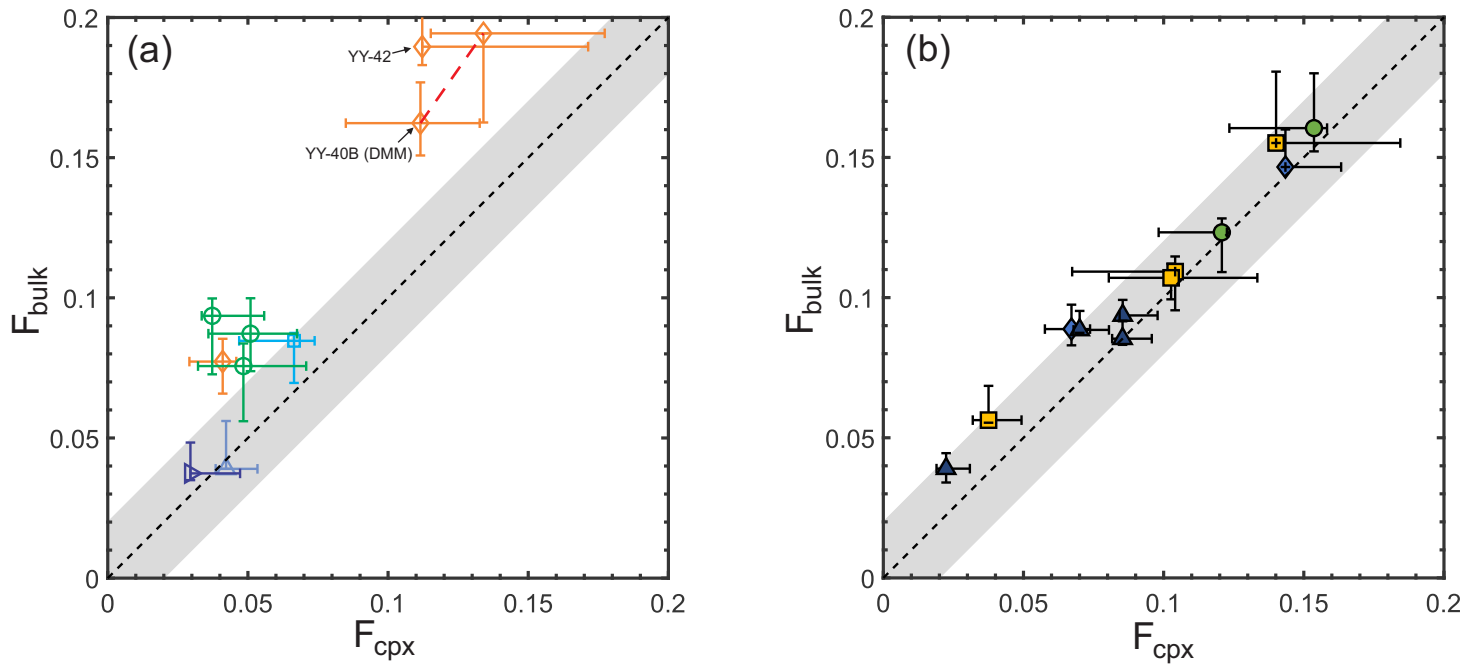
**Figure 7**

Fig. 7. Comparison of the degree of melting derived from the cpx-alone inversion ( $F_{cpx}$ ) and the degree of melting derived from inversion of the bulk sample ( $F_{bulk}$ ) for the mantle xenoliths (a) and abyssal peridotites (b) selected in this study. The dashed lines and grey areas represent the 1:1 ratio within a  $\pm 2\%$  range. The red dashed line in (a) connects the inversion results of sample YY-40B with primitive mantle (PM) and the depleted MORB mantle (DMM) starting compositions. Error bars are based on MCMC simulations. Sample legends are the same as in Fig. 2.

Figure 8

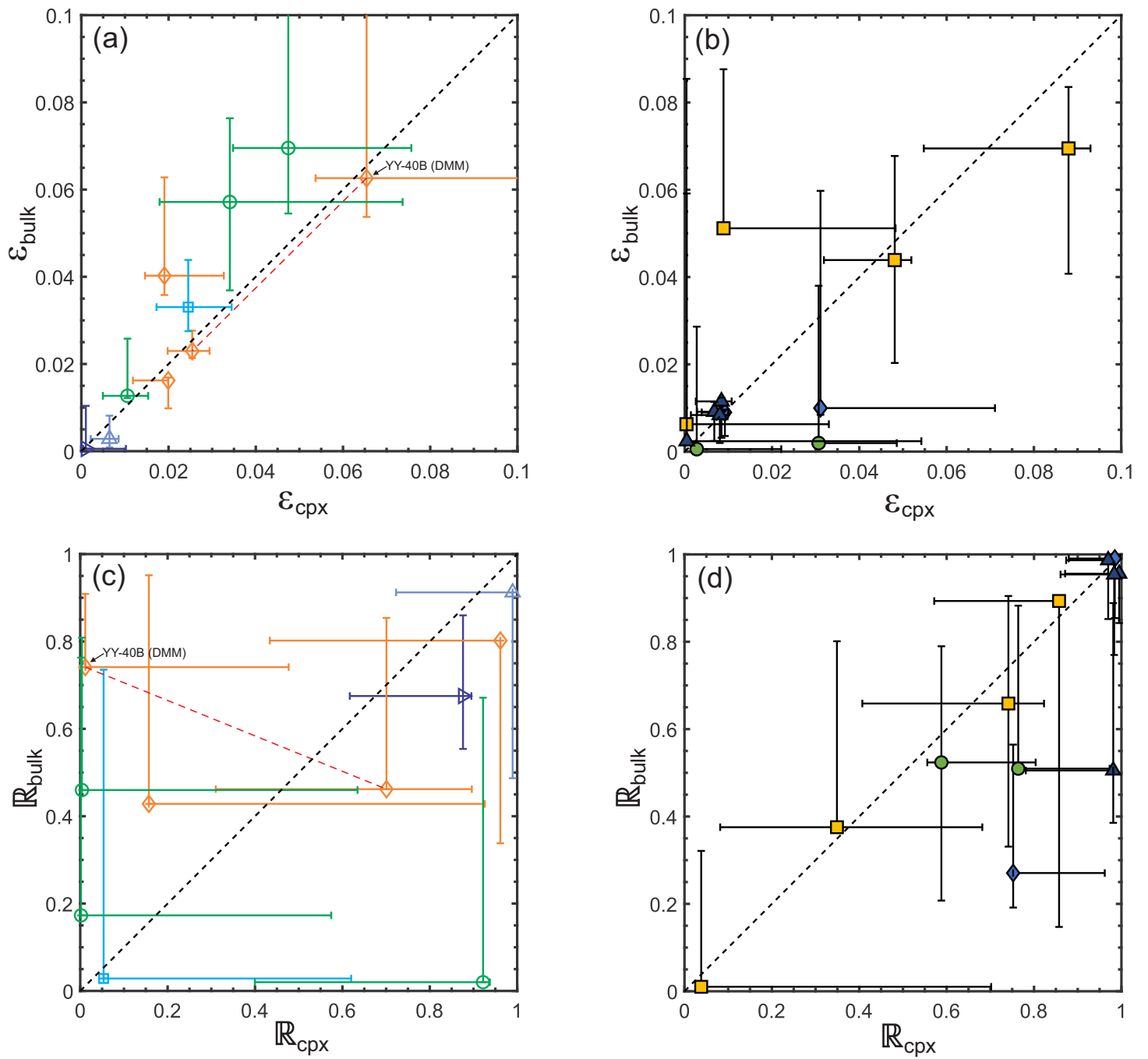


Fig. 8. Comparison of disequilibrium parameters ( $\epsilon$ ) and melt suction rate ( $R$ ) derived from the cpx-alone inversion and the bulk sample inversion for mantle xenoliths (a and c) and abyssal peridotites (b and d). Other details are the same as in Fig. 7.

Figure 9

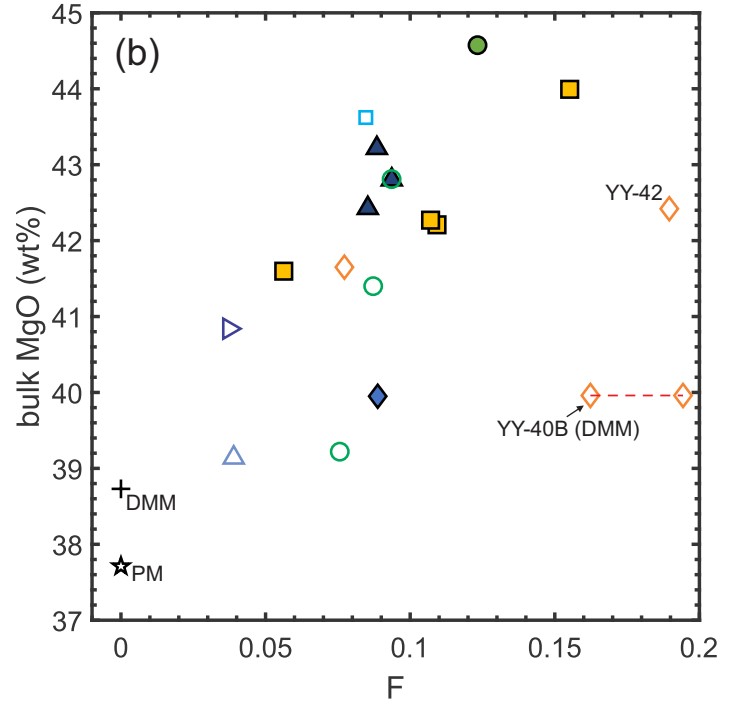
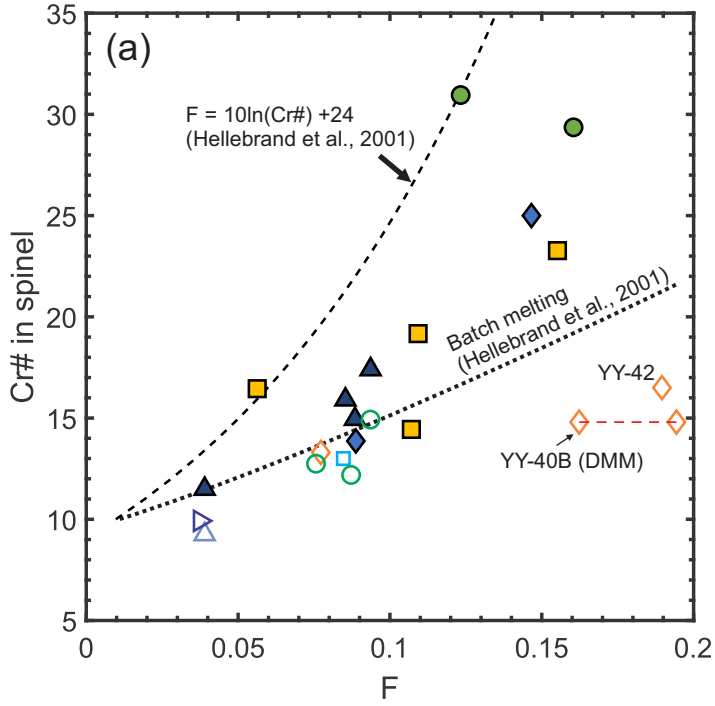


Fig. 9. Variations of spinel Cr# (a) and bulk MgO content (b) as a function of the degree of melting for the mantle xenoliths and abyssal peridotites included in this study. The two dashed lines are based on the empirical expressions of Hellebrand et al. (2001) for fractional and batch melting.

1           What can we learn from REE abundances in clinopyroxene and  
2                           orthopyroxene in residual mantle peridotites?

3  
4                           Yan Liang<sup>1</sup>, Zejia Ji<sup>1,2</sup>, and Boda Liu<sup>1,\*</sup>

5       1 Department of Earth, Environmental and Planetary Sciences, Brown University, Providence,  
6                           RI 02912, United States

7       2 The Key Laboratory of Orogenic Belts and Crustal Evolution, Peking University, Beijing,  
8                           100871, China

9       \* Now at Department of Earth, Environmental and Planetary Sciences, Rice University, Houston,  
10                           TX 77005, United States

11                           Corresponding author: Yan Liang ([yan\\_liang@brown.edu](mailto:yan_liang@brown.edu))

12  
13                           **Abstract**

14           Clinopyroxene and orthopyroxene are the two major repositories of rare earth elements  
15 (REE) in spinel peridotites. Most geochemical studies of REE in mantle samples focus on  
16 clinopyroxene. Recent advances in in situ trace element analysis has made it possible to measure  
17 REE abundance in orthopyroxene. The purpose of this study is to determine what additional  
18 information one can learn about mantle processes from REE abundances in orthopyroxene  
19 coexisting with clinopyroxene in residual spinel peridotites. To address this question, we select a  
20 group of spinel peridotite xenoliths (9 samples) and a group of abyssal peridotites (12 samples)  
21 that are considered residues of mantle melting and that have major element and REE compositions  
22 in the two pyroxenes reported in the literature. We use a disequilibrium double-porosity melting  
23 model and the Markov chain Monte Carlo method to invert melting parameters from REE  
24 abundance in the bulk sample. We then use a subsolidus reequilibration model to calculate REE  
25 redistribution between cpx and opx at the extent of melting inferred from the bulk REE data and  
26 at the closure temperature of REE in the two pyroxenes. We compare the calculated results with  
27 those observed in clinopyroxene and orthopyroxene in the selected peridotitic samples. Results

28 from our two-step melting followed by subsolidus reequilibration modeling show that it is more  
29 reliable to deduce melting parameters from REE abundance in the bulk peridotite than in  
30 clinopyroxene. We do not recommend the use of REE in clinopyroxene alone to infer the degree  
31 of melting experienced by the mantle xenolith, as HREE in clinopyroxene in the xenolith are reset  
32 by subsolidus reequilibration. In general, LREE in orthopyroxene and HREE in clinopyroxene are  
33 more susceptible to subsolidus redistribution. The extent of redistribution depends on the modes  
34 of clinopyroxene and orthopyroxene in the sample and thermal history experienced by the  
35 peridotite. By modeling subsolidus redistribution of REE between orthopyroxene and  
36 clinopyroxene after melting, we show that it is possible to discriminate mineral mode of the starting  
37 mantle and cooling rate experienced by the peridotitic sample. We conclude that endmembers of  
38 the depleted MORB mantle and the primitive mantle are not homogeneous in mineral mode. A  
39 modally heterogeneous peridotitic starting mantle provides a simple explanation for the large  
40 variations of mineral mode observed in mantle xenoliths and abyssal peridotites. Finally, by using  
41 different starting mantle compositions in our simulations, we show that composition of the  
42 primitive mantle is more suitable for modeling REE depletion in cratonic mantle xenoliths than  
43 the composition of the depleted MORB mantle.

44

## 45 **Introduction**

46 Rare earth elements (REE) in mantle rocks have been widely used to study partial melting,  
47 melt migration and melt-rock interaction processes in the mantle. Most geochemical studies of  
48 REE in spinel peridotites focus on clinopyroxene (cpx) which is the major repository of REE in  
49 the peridotites. Important conclusions based on REE abundances in cpx in abyssal peridotites  
50 include (1) samples with depleted LREE are resulted from fractional or near fractional melting  
51 (Johnson et al., 1990; Johnson and Dick, 1992; Kelemen et al., 1997; Niu and Hékinian, 1997;  
52 Shimizu, 1998; Hellebrand et al., 2001; Brunelli et al., 2006; Liang and Peng, 2010); (2) samples  
53 with elevated LREE are affected by melt impregnation and melt-rock interaction (Hellebrand et  
54 al., 2002; Warren et al., 2009; Brunelli et al., 2014); and (3) cpx with higher HREE but depleted  
55 LREE is attributed to fractional melting starting in the garnet stability field (Johnson et al., 1990;  
56 Hellebrand et al., 2002; Brunelli et al., 2006). However, not all of the interpretations are unique.  
57 For example, the slightly elevated LREE patterns in abyssal peridotites that show no obvious signs

58 of melt addition can also be explained by small extent of disequilibrium melting (Liang and Liu,  
59 2016; Liu and Liang, 2017). Near fractional melting starting in the garnet stability field failed to  
60 explain some samples with elevated HREE patterns (Liang and Peng, 2010). One possible  
61 explanation of the higher than expected HREE in residual cpx is subsolidus redistribution (Sun  
62 and Liang, 2014). During subsolidus reequilibration, REE is strongly and preferentially  
63 partitioning into cpx relative to orthopyroxene and olivine in spinel peridotites (e.g., Stosch, 1982;  
64 Witt-Eickschen and O'Neill, 2005; Lee et al., 2007; Liang et al., 2013; Sun and Liang, 2014). To  
65 sort out the various magmatic and subsolidus processes affecting the abundance and distribution  
66 of REE and other trace elements in residual peridotites, additional information is needed.

67         Recent advances in in situ trace element analysis makes it possible to measure REE and  
68 other incompatible trace elements in orthopyroxene (opx). An increasing number of geochemical  
69 studies of spinel peridotites have reported REE in both cpx and opx (e.g., Stosch, 1982; Bedini  
70 and Bodinier, 1999; Hellebrand et al., 2005; Witt-Eickschen and O'Neill, 2005; Warren et al.,  
71 2009; Brunelli and Seyler, 2010; Seyler et al., 2011; Liu et al., 2012; D'Errico et al., 2016; Quinn  
72 et al., 2018). These additional data not only can be used to reconstruct bulk trace element  
73 compositions for samples that experienced secondary alteration, but also offer an opportunity for  
74 a more complete assessment of the thermal and magmatic history experienced by the peridotite.  
75 To learn more from REE abundances in coexisting cpx and opx in residual peridotite samples, we  
76 use a disequilibrium double-porosity melting model and a subsolidus reequilibration model to  
77 investigate how REE in the bulk residue are fractionated during decompression melting along a  
78 mantle adiabat and how REE in residual cpx and opx are redistributed during subsolidus  
79 reequilibration after melting. In a closed system, REE abundance in the bulk sample is independent  
80 of subsolidus reequilibration, whereas REE abundances in coexisting cpx and opx are sensitive to  
81 temperature and mineral mode. Hence it is more advantageous to infer melting parameters from  
82 REE abundance in the bulk sample than in cpx alone.

83         The chief objectives of this study are twofold: (1) to develop a general method for  
84 interpreting REE in residual cpx, opx, and the bulk peridotite; and (2) to determine what more we  
85 can learn from REE concentrations in opx in addition to cpx in residual mantle peridotites. We use  
86 a general double-porosity model for disequilibrium melting in an upwelling melting column to  
87 address objective (1). In the absence of chemical disequilibrium, concentrations of REE in opx are

88 related to those in cpx by mineral-melt or mineral-mineral partition coefficients. Hence REE in  
89 residual cpx alone are sufficient for studying the melting history experienced by residual  
90 peridotites. This was first demonstrated in the pioneering work of Johnson et al. (1990). However,  
91 detailed modeling of REE in residual cpx in abyssal peridotites suggests that their LREE patterns  
92 can be better explained if a small extent of chemical disequilibrium is present between cpx and  
93 coexisting melt during partial melting (Liang and Liu, 2016; Liu and Liang, 2017). The present  
94 study is built on these recent modeling work by considering REE in opx in addition to cpx during  
95 disequilibrium melting. To achieve objective (2), we conduct two case studies of REE in selected  
96 residual spinel peridotites from subcontinental lithosphere (mantle xenoliths) and mid-ocean  
97 ridges (abyssal peridotites). We use the disequilibrium melting model to calculate REE  
98 concentrations in residual cpx, opx, and the bulk peridotite. We then redistribute REE between cpx  
99 and opx at their closure temperature using temperature-dependent REE opx-cpx partition  
100 coefficients and modal abundances of cpx and opx in the sample. We show that this two-step  
101 melting followed by subsolidus reequilibration modeling, which has not been done before, allows  
102 us to better match the observed REE patterns of cpx and opx in the two sets of peridotite samples.  
103 By including REE in opx in our modeling, we can learn not only the melting process but also  
104 thermal history experienced by the residual peridotites after melting. The latter is sensitive to  
105 mineral modes in the starting mantle. As will be demonstrated in this study, it is possible to  
106 constrain mineral mode in the starting mantle and thermal history of the residual peridotites based  
107 on REE abundances in both cpx and opx.

108

## 109 **Melting followed by subsolidus reequilibration**

### 110 **Model description**

111 We are interested in the fractionation of REE in bulk peridotite during decompression  
112 melting in a mantle column and the redistribution of REE between cpx and opx in the peridotite at  
113 a subsolidus temperature after melting. We use the disequilibrium double-porosity melting model  
114 of Liang and Liu (2016) to simulate REE depletion during decompression melting along a mantle  
115 adiabat. For the convenience of a reader, the governing equations are summarized in Appendix A.  
116 Key features of the disequilibrium melting model include channelized melt extraction and

117 diffusion-limited chemical exchange between the pyroxenes and the interstitial melt. Because  
 118 diffusivities of REE in olivine and garnet are considerably larger than those in the pyroxenes (Van  
 119 Orman et al., 2001, 2002; Cherniak and Liang, 2007; Cherniak, 2015) and abundances of REE in  
 120 olivine and spinel are much smaller than those in the pyroxenes, it is reasonable to assume that  
 121 olivine and spinel (also garnet for melting in the garnet stability field) are in local chemical  
 122 equilibrium with their interstitial melt during decompression melting.

123 There are four dimensionless parameters in the disequilibrium double-porosity melting  
 124 model for this problem: degree of melting experienced by the residual mantle ( $F$ ), fraction of melt  
 125 extracted to the channel ( $\mathbb{R}$ , called melt suction rate hereafter), disequilibrium parameter of La in  
 126 cpx ( $\varepsilon_{cpx}^{La}$ ), and relative diffusion rate of REE in cpx and opx grains. The melt suction rate is an  
 127 important parameter of the double-porosity melting model (Iwamori, 1994; Lundstrom, 2000; Jull  
 128 et al., 2002; Liang and Peng, 2010). The double-porosity model recovers the perfect fractional  
 129 melting model when  $\mathbb{R} = 1$  and the batch melting model when  $\mathbb{R} = 0$ . We refer the style of  
 130 melting as near fractional when more than 75% of melt produced by peridotite melting are  
 131 extracted to the channel (i.e.,  $0.75 < \mathbb{R} < 1$ ). The diffusive exchange rate constants for an REE  
 132 in opx ( $R_{opx}$ ) and cpx ( $R_{cpx}$ ) are inversely proportional to the diffusive time scales for opx and cpx  
 133 (Navon and Stolper, 1987; Bodinier et al., 1990; Liang, 2003):

$$134 \quad R_{opx} = \frac{3\beta D_{opx}}{d_{opx}^2}, \quad R_{cpx} = \frac{3\beta D_{cpx}}{d_{cpx}^2}, \quad (1a, 1b)$$

135 where  $D$  is the diffusion coefficient of REE in opx or cpx;  $d$  is the average or effective mineral  
 136 grain size of opx or cpx; and  $\beta$  is a geometric factor. The relative diffusion rate for an REE is given  
 137 by the expression:

$$138 \quad \frac{R_{opx}^{REE}}{R_{cpx}^{REE}} = \frac{D_{opx}^{REE}}{D_{cpx}^{REE}} \frac{d_{cpx}^2}{d_{opx}^2}. \quad (2)$$

139 The disequilibrium parameter is a measure of bulk melting rate relative to diffusion rate for the  
 140 element of interest in a mineral (Eq. A1d in Appendix A). Given the disequilibrium parameter of  
 141 La in cpx, disequilibrium parameters for other REE in cpx can be calculated according to their  
 142 diffusivity ratio (Liang and Liu, 2016):

143 
$$\epsilon_{cpx}^{REE} = \frac{D_{cpx}^{La}}{D_{cpx}^{REE}} \epsilon_{cpx}^{La} . \quad (3)$$

144 During decompression melting along a mantle adiabat, temperature decreases upward in the  
 145 melting column. In this study, we calculate the relative diffusion rate and disequilibrium  
 146 parameters using experimentally determined diffusion parameters for REE in cpx and opx (Van  
 147 Orman et al., 2001, 2002; Cherniak and Liang, 2007). For convenience of numerical calculations,  
 148 we scale the disequilibrium parameters in Eq. 3 by their respective values at 1300°C,

149 
$$\epsilon_{cpx}^T = \frac{D_{cpx}^{1300}}{D_{cpx}^T} \epsilon_{cpx}^{1300} . \quad (4)$$

150 In the simulations presented below, we treat  $\epsilon_{cpx}^{1300}$  for La in cpx as a free parameter and calculate  
 151 the disequilibrium parameter at other temperatures using Eq. 4. Variations of the disequilibrium  
 152 parameter of La in cpx as a function of temperature and degree of melting along a 1300 °C mantle  
 153 adiabat can be found in supplementary Fig. S1. Equilibrium melting is realized when  $\epsilon_{cpx}^{La} = 0$ .

154 We use the temperature and major element composition dependent opx-cpx and olivine-  
 155 cpx REE partitioning models of Sun and Liang (2014) and mineral mode in the sample to calculate  
 156 REE abundances in coexisting opx and cpx at a subsolidus temperature after melting. In a closed  
 157 system, concentration of a trace element in the bulk peridotite ( $C_s$ ) depends on mineral mode and  
 158 mineral composition, but is independent of temperature, viz.,

159 
$$C_s = w_{cpx} C_{cpx} + w_{opx} C_{opx} + w_{ol} C_{ol} + w_{sp} C_{sp} , \quad (5)$$

160 where  $w_j$  and  $C_j$  are the weight fraction of and trace element concentration in mineral  $j$  in the  
 161 residual peridotite, respectively. Since REE abundances in olivine and spinel are much lower than  
 162 those in cpx and opx, concentrations of an REE in cpx and opx at a given temperature ( $T$ ) can be  
 163 calculated using the expressions (see also Eq. A2e in Appendix A):

164 
$$C_{cpx}(T) = \frac{C_s}{w_{cpx} + w_{opx} k_{opx-cpx}} , \quad (6a)$$

165 
$$C_{opx}(T) = k_{opx-cpx} C_{cpx} , \quad (6b)$$

166 where  $k_{\text{opx-cpx}}$  is the temperature and major element composition dependent opx-cpx REE partition  
167 coefficient. In the case studies presented below, we set the temperature in Eqs. 6a and 6b to the  
168 closure temperature of REE based on the REE-in-two-pyroxene thermometer of Liang et al. (2013).  
169 According to Eqs. 6a and 6b, concentrations of REE in cpx and opx in a residual peridotite vary  
170 as a function of mineral mode and temperature even when concentrations of REE in the bulk rock  
171 are constant. The sensitivity of REE redistribution to mineral mode and subsolidus temperature  
172 will be demonstrated below.

173

### 174 **Forward simulations of REE in pyroxenes during melting and subsolidus reequilibration**

175 Variations of REE in opx and cpx in residual peridotites that have experienced  
176 decompression melting and subsolidus reequilibration can be visualized through forward  
177 simulations using the two-step melting followed by subsolidus reequilibration model outlined in  
178 the preceding section. Figure 1a shows one such example for a case of 6% near fractional melting  
179 ( $R = 0.95$ ,  $\epsilon_{La}^{1300} = 0.01$ ) of spinel lherzolite along the 1300 °C adiabat. Melting strongly depletes  
180 LREE in both cpx and opx, hence the bulk rock (solid lines in Fig. 1a). Since REE abundances in  
181 cpx are considerably higher than those in opx, olivine and spinel, REE pattern of the bulk residue  
182 follows that of cpx, forming subparallel trends in the chondrite-normalized REE diagram (Fig. 1a).  
183 To the first order, REE abundance in the bulk rock is proportional to the amount of cpx in the  
184 residue, viz.,  $C_s \sim w_{\text{cpx}} * C_{\text{cpx}}$ . This is demonstrated in Fig. 1a where the abundance of REE in cpx  
185 is about 7 times that in the bulk rock and the modal abundance of cpx in the residue after 6%  
186 melting is 13.6%. The close similarity between REE in the bulk rock and its constituent cpx forms  
187 the basis for using REE in cpx to study mantle melting processes in the literature.

188 Figure 1a also shows that REE pattern of residual opx differs considerable from those of  
189 cpx and the residue: light and middle REE are preferentially depleted in opx relative to those in  
190 the bulk or cpx whereas heavy REE in opx are comparable to those in the bulk rock. This is due to  
191 the smaller M2 site of opx structure, making LREE more incompatible in opx than in cpx. The net  
192 effect is a steeper LREE depleted pattern for opx in the REE diagram. The REE pattern in opx can  
193 be further complicated by subsolidus reequilibration: with decreasing temperature, LREE is  
194 preferentially redistributed from opx to cpx, shifting the entire opx REE pattern below that  
195 produced by partial melting (cf. dashed and solid green lines in Fig. 1a). Although it is not

196 straightforward to infer mantle melting processes based on REE abundances and patterns in opx  
197 in residual peridotites that are reset by subsolidus reequilibration, abundances of REE in opx may  
198 offer useful information on the thermal history experienced by the peridotite and mineral modes  
199 in the starting mantle, as we will demonstrate through two case studies below. However, due to  
200 the ionic size-dependent REE opx-cpx partitioning, subsolidus reequilibration mildly elevates  
201 HREE in cpx (Figs. 1a and 1b), which may complicate the interpretation of garnet signal in residual  
202 spinel lherzolite and harzburgite (Sun and Liang, 2014). Since the abundance of LREE is  
203 considerably lower in residual opx, LREE in cpx are not sensitive to subsolidus redistribution in  
204 spinel lherzolite. When the degree of melting is large, the modal abundance of cpx decreases in  
205 the residue, and the effect of subsolidus reequilibration on the REE in cpx will be more significant.  
206 This is illustrated in Fig. 1b for a case of 15% near fractional melting ( $R = 0.95$ ,  $\epsilon_{La}^{1300} = 0.01$ ).

207         The mineral grain size also affects REE abundances in cpx and opx during disequilibrium  
208 melting and subsequent cooling through the relative diffusive exchange rate (Eq. 2). In general,  
209 grain size of opx (2-5 mm) is larger than grain size of cpx (< 2 mm) in residual spinel peridotites.  
210 The effect of chemical disequilibrium increases with increasing opx grain size, leading to an  
211 increase in the effective or apparent partition coefficient for REE between opx and its coexisting  
212 melt (Liang and Liu, 2016). This can be demonstrated through a forward simulation in which we  
213 increase the relative opx-to-cpx grain size from 1 to 5 while keeping the cpx grain size to 1 mm.  
214 As shown in Fig. 1c, the calculated middle and heavy REE abundances in cpx slightly decrease  
215 whereas the light REE abundances in opx significantly increase compared to the case of 1 mm opx.  
216 Consequently, the simulated bulk REE is not very sensitive to the choice of opx/cpx grain size  
217 ratio. Regardless of how REE are distributed between opx and cpx, the REE abundance in the bulk  
218 residue remains the same as that produced by partial melting. Hence it is more reliable to use REE  
219 in the bulk rock to infer melting processes experienced by residual peridotites than REE in cpx  
220 alone. We will demonstrate this point through two case studies below.

221

## 222 **Reading magmatic and thermal history from REE abundances in bulk** 223 **peridotites and two pyroxenes**

### 224 **Strategy and methods**

225 We use the melting followed by subsolidus reequilibration model and REE abundances in  
226 selected bulk samples and their constituent cpx and opx to infer melting and cooling processes  
227 experienced by residual peridotites. Based on forward simulations such as the ones shown in Fig.  
228 1, we treat this problem in two sequential steps: melting and subsolidus redistribution. For the  
229 melting part, we use Bayesian analysis and the disequilibrium double-porosity melting model to  
230 invert key melting parameters ( $F$ ,  $\mathbb{R}$ , and  $\varepsilon_{cpx}^{La}$ ) from the observed REE concentrations in the bulk  
231 residual peridotite. To account for temperature-dependent diffusive exchange of REE in cpx and  
232 opx (Eq. 1), we carry out disequilibrium melting calculations along a mantle adiabat in the  
233 Bayesian analysis. Since our inversion is based on bulk REE in the peridotite, REE concentrations  
234 in cpx and opx derived from our best-fit model are not required to match the observed REE patterns  
235 in cpx and opx in the peridotite sample, as the latter concentrations can be reset by subsolidus  
236 reequilibration. For the subsolidus part of our modeling, we use Eqs. 6a and 6b and the model-  
237 predicted bulk REE concentration from the first step to calculate REE concentrations in cpx and  
238 opx at the closure temperature of REE in the two pyroxenes. The closure temperature is calculated  
239 using measured REE and major element compositions of cpx and opx in the peridotite sample and  
240 the REE-in-two-pyroxene thermometer of Liang et al. (2013). As will be shown in the two case  
241 studies below, inversion of bulk REE in residual peridotites is not sensitive to mineral modes in  
242 the starting mantle, whereas subsolidus redistribution of REE between cpx and opx is sensitive to  
243 mineral mode. Given the large variations of mineral modes in mantle peridotites (e.g., Bodinier  
244 and Godard, 2014; Warren, 2016) and uncertainties in estimating mineral modes of peridotite  
245 samples, we carry out the melting and subsolidus simulations using three choices of starting mantle  
246 mode, as detailed below. Our preferred model produces the closest match to the observed REE  
247 concentrations in the bulk rock and the two pyroxenes.

248 To demonstrate the advantages of the method outlined in the preceding paragraph, we  
249 model REE + Y abundances in selected spinel peridotite samples from subcontinental lithosphere  
250 (mantle xenoliths, 9 samples) and mid-ocean ridges (abyssal peridotites, 12 samples). We include  
251 Y in our analysis because it behaves similarly to HREE during mantle melting and its abundance  
252 is routinely reported along with REE in opx and cpx. Peridotites from stable cratons are generally  
253 well-equilibrated and have similar and relatively low equilibrium or closure temperatures for both  
254 major elements and REE in coexisting cpx and opx, whereas abyssal peridotites have higher

255 closure temperatures for REE than major elements in pyroxenes (Liang et al., 2013; Dygert and  
256 Liang, 2015; Wang et al., 2015). This is illustrated in Fig. 2 for the selected samples in this study.  
257 Since abyssal peridotites are variously serpentized and some mantle xenoliths contain glass veins,  
258 we use measured REE + Y abundances in minerals (cpx, opx, and olivine when available) and  
259 mineral modes reported in the literature to reconstruct bulk REE + Y abundances in the peridotites.  
260 As shown in Fig. 1, the light and middle REE in opx are considerably lower than those in cpx,  
261 making accurate measurements of these elements in opx an analytical challenge. This problem is  
262 especially prevalent for odd atomic number elements such as La (57) and Pr (59), resulting in  
263 scattered LREE patterns in some samples. To include more elements and more samples in this  
264 study, we applied an interpolation/extrapolation procedure to some of the samples that exhibit  
265 scattered REE patterns. The procedure, detailed in Supplementary Materials (*REE interpolation  
266 procedure and results*), is based on correlation between the nearest neighbor REE (e.g., La and Ce)  
267 established by mantle pyroxenes that have smooth REE patterns. In Supplementary Table S1a, we  
268 list mineral modes and REE concentrations in cpx, opx, and the bulk peridotite included in this  
269 study.

270 In order to use the disequilibrium melting model to calculate the melting parameters from  
271 the bulk REE + Y abundances in residual peridotites, we need to know mineral grain size, mineral  
272 mode, and composition of the starting mantle. Following standard practice in REE modeling, we  
273 assume that abundances of REE + Y in the starting mantle are the same as the average depleted  
274 MORB mantle (DMM, Workman and Hart, 2005) for abyssal peridotites and the primitive mantle  
275 (PM, McDonough and Sun, 1995) for mantle xenoliths in our first round of simulations. To assess  
276 uncertainties and misfits, we also explore other starting mantle compositions. The mineralogy of  
277 the starting mantle is a primitive spinel lherzolite. (We will discuss garnet field melting in a later  
278 section.) There are some uncertainties in the mineral mode of the starting mantle. For example, the  
279 DMM of Workman and Hart (2005) consists of 13% cpx, 28% opx, 57% olivine, and 2% spinel,  
280 whereas the starting mantle of Johnson (1998) and Hellebrand et al. (2002) has 17% cpx, 27% opx,  
281 53% olivine, and 3% spinel. The latter has been used in our inverse modeling of REE depletion in  
282 residual cpx from abyssal peridotites (Liang and Peng, 2010; Liang and Liu, 2016; Liu and Liang,  
283 2017). Figs. 3a and 3b show large variations in mineral modes in both mantle xenoliths and abyssal  
284 peridotites. (For more peridotite data, a reader is referred to Fig. 1 in Bodinier and Godard (2014)  
285 and Fig. 4 in Warren (2016).) Even for the small number of samples included in the present study,

286 the range of modal variations cannot be explained by a single melting trend or melting reaction  
287 using either aforementioned starting mode. It is possible that mineral modes are not well  
288 constrained for some of the peridotite samples (e.g., heavily serpentinized abyssal peridotites,  
289 point counting of small area). It is also likely that mineral mode in the starting mantle is not  
290 uniform, considering the efficiency of mantle convection, lithological heterogeneities in the mantle,  
291 and diversity of peridotites in the field. In this study, we consider three mineral modes for the  
292 starting mantle source. To reduce the number of free parameters in our modeling, we fix the modal  
293 abundance of olivine in the mantle source to 56% or 60.5% and vary the cpx:opx proportion in the  
294 mantle source for the mantle xenolith or abyssal peridotite samples (Figs. 3a and 3b). This is a  
295 reasonable approach as (1) the relative REE pattern in the bulk rock is not very sensitive to the  
296 abundance of olivine in the mantle source, and (2) the resultant residual modes cover a wide range  
297 of mineral modal abundances (Fig. 3). Finally, the grain size of the starting mantle is unknown,  
298 although in general grain size of opx is larger than grain size of cpx in peridotites. As a starting  
299 model, we assume that the grain size ratio between opx and cpx ( $\frac{d_{cpx}}{d_{opx}}$ ) does not change during  
300 melting. The latter helps to simplify the evaluation of the relative diffusion rate between opx and  
301 cpx (Eq. 2).

302 Mantle melting is non-modal. In standard geochemical treatment of non-modal melting,  
303 one uses melting reaction derived from peridotite melting studies. The coefficients of the melting  
304 reaction are constant and residual mineral modes vary linearly as a function of  $F$  in the melting  
305 column. In this study, we use the melting reaction of Baker and Stolper (1994) for spinel lherzolite  
306 in our inverse modeling of REE + Y in the bulk mantle xenoliths. This standard geochemical  
307 approach is adequate for modeling REE in mantle xenoliths as detailed melting processes  
308 experienced by the lithospheric mantle are not well understood. To model garnet-field melting in  
309 a self-consistent way for abyssal peridotites, we use mineral modes derived from pMELTS  
310 (Ghiorso et al., 2002) simulation of decompression melting along an adiabat. In this pMELTS  
311 based model, mineral modes ( $w_j$  in Eqs. A2a-A2e in Appendix A) vary somewhat nonlinearly as  
312 a function of  $F$  in the melting column (the three curves in Fig. 3b). Nonetheless, the average  
313 melting reaction derived from the pMELTS based modeling is very similar to the 1 GPa melting  
314 reactions of Baker and Stolper (1994) and Kinzler and Grove (1992) for spinel lherzolite (see  
315 Table 2 in Walter, 2014). As detailed in the section *Case study 2: Abyssal peridotites*, this

316 pMELTS based modeling allows us to eliminate a free parameter in garnet-field melting. With the  
317 stated choices of mineral modes and melting reactions, our melting model is able to cover most of  
318 the observed variations in mineral modes in the selected mantle samples (Figs. 3a and 3b).

319 The disequilibrium double-porosity melting model summarized in Appendix A consists of  
320 three coupled nonlinear ordinary differential equations and one algebraic equation for spatial  
321 variations of a trace element in interstitial melt, cpx, opx, and bulk residue (Eqs. A2a-A2d). They  
322 have no analytical solutions for the problem outlined above. Hence, we cannot use nonlinear least  
323 squares analysis to invert melting parameters as we did for REE in cpx (Liang and Peng, 2010;  
324 Liang and Liu, 2016). To get around this difficulty, we use Markov chain Monte Carlo (MCMC)  
325 method to invert the melting parameters  $F$ ,  $\epsilon_{cpx}^{1300}$ , and  $\mathbb{R}$  from REE + Y concentrations in the bulk  
326 sample. MCMC methods are a class of powerful statistical tools for solving nonlinear inverse  
327 problems in Bayesian analysis (e.g., Sambridge and Mosegaard, 2002). Liu and Liang (2017) used  
328 MCMC to invert melting parameters from REE abundance in residual cpx in abyssal peridotites.  
329 The present work follows the inversion procedure detailed in their study. To facilitate MCMC  
330 inversion, we set bounds for the disequilibrium parameter  $\epsilon_{cpx}^{1300}$  to  $[0, 0.15]$  and the melt suction  
331 rate  $\mathbb{R}$  to  $[0, 1]$ , based on previous inversion results using similar model or method (Lundstrom,  
332 2000; Liang and Peng, 2010; Liang and Liu, 2016; Liu and Liang, 2017). We run 10,000 to 50,000  
333 simulations for each sample to ensure convergence and use the result to calculate best fitting  
334 parameters and uncertainties. The best fitting parameters are then used to calculate REE  
335 abundances in the bulk sample, residual cpx and opx, and chemically re-equilibrated cpx and opx  
336 at closure temperatures in the two pyroxenes. Below we present results from two case studies.

337

### 338 **Case study 1: Mantle xenoliths**

339 To demonstrate the basic feature of the disequilibrium melting model and the effect of  
340 subsolidus redistribution, we select 9 well-characterized spinel lherzolite and harzburgite  
341 xenoliths from the literature: 3 samples from Yangyuan, North China Craton (Liu et al., 2012), 1  
342 sample from West Eifel, Germany (Witt-Eickschen and O'Neill, 2005), 1 sample from East Africa  
343 Rift (Bedini and Bodinier, 1999), 3 samples from Kilbourne Hole, New Mexico (Harvey et al.,  
344 2012), and 1 sample from the Coast Ranges of central California (Quinn et al., 2018). These

345 samples are protogranular, free of garnet, plagioclase, hydrous minerals, and veins. They are  
 346 selected on the basis of their depleted light REE patterns in cpx and opx, well-defined linear trends  
 347 for at least the middle and heavy REE in the inversion diagram of the REE-in-two-pyroxene  
 348 thermometer, and similar equilibrium temperatures between major element-based and REE-based  
 349 pyroxene thermometers. Figure 2 shows that the calculated temperatures are generally below the  
 350 solidus of the peridotite xenoliths. Figure 3a displays modal abundances of the selected samples.  
 351 For reference, we plot selected major element concentrations in these samples as a function of bulk  
 352 MgO content and spinel Cr# (= 100Cr/Cr+Al, in molar) in supplementary Figs. S2a and S2b.  
 353 Supplementary Tables S1b and S2 and Fig. S4 present results of MCMC simulations with PM and  
 354 DMM starting compositions for the nine xenolith samples along the 1300°C mantle adiabat (Fig.  
 355 S1). Figure 4 shows an example of MCMC simulations for sample CK-2 from the Coast Ranges  
 356 of central California (Quinn et al., 2018). Figure 5 presents the best fit models for the nine xenoliths  
 357 with PM starting compositions. The main results are summarized below.

358 First, the bulk REE patterns are well reproduced by the disequilibrium double-porosity  
 359 melting model. The quality of fit is not very sensitive to the choice of starting mantle mode (cf.  
 360 Figs. 4a-4c). This is shown by the similar Pearson's Chi-squares among the three cases for each  
 361 sample (Supplementary Table S2). Here we calculate Pearson's Chi-square for the bulk REE after  
 362 inversion using the expression:

$$363 \quad \chi_{bulk}^2 = \sum_{j=1}^N \frac{(C_{s,j} - C_{s,j}^m)^2}{C_{s,j}}, \quad (7)$$

364 where  $C_{s,j}$  and  $C_{s,j}^m$  are the model-derived and measured bulk solid concentrations for element  $j$ ,  
 365 respectively;  $N$  (= 14) is the number of elements in the model. In general, the smaller the Pearson's  
 366 Chi-square, the better the model prediction will be. There is a small trade-off between cpx  
 367 abundance in the starting mantle and the degree of melting: the higher the cpx mode in the starting  
 368 mantle, the greater the degree of melting is required to match the observed depletion in REE in the  
 369 bulk residue. Increasing cpx mode from 14% to 20% in the starting mantle results in 0.11~3%  
 370 increase in the inferred degree of melting for the nine xenolith samples.

371 Second, the observed REE patterns in residual cpx and opx (filled blue and green circles  
 372 in Figs. 4 and 5) cannot be reproduced directly using melting parameters derived from the bulk

373 REE pattern (blue and green solid lines). Very often, LREE in opx is overestimated and HREE in  
374 cpx is underestimated by the melting model, which appears to be consistent with the subsolidus  
375 reequilibration trends displayed in Fig. 1. To quantify the effect of subsolidus redistribution, we  
376 recalculated the model-derived REE concentrations in opx and cpx using the temperature and  
377 major element composition dependent REE opx-cpx partition coefficients (Sun and Liang, 2014)  
378 and closure temperatures ( $T_{REE}$ ) derived from the REE-in-two-pyroxene thermometer (Liang et al.,  
379 2013). The latter is 964°C for sample CK-2. ( $T_{REE}$  for the nine xenoliths are provided in Fig. 5.)  
380 Figures 4 and 5 (see also supplementary Fig. S4) show that the matches to the measured REE  
381 patterns in cpx and opx in the nine xenolith samples are considerably improved after adjustment  
382 of subsolidus redistribution. This is an important new result from this study.

383 Finally, for a given sample, our preferred starting mantle mode and melting parameter  
384 should have the smallest sum of Pearson's Chi-squares for the bulk peridotite, cpx, and opx among  
385 the three starting mantle modes, where Pearson's Chi-squares for cpx and opx are calculated after  
386 adjustment for subsolidus reequilibration. Figure 5 summarizes results of our preferred model and  
387 Supplementary Table S2 provides additional information on uncertainties of our preferred melting  
388 parameters and Pearson's Chi-squares. To facilitate discussion, we also invert melting parameters  
389 from REE in cpx alone using the disequilibrium melting model of Liu and Liang (2017). It is  
390 interesting to note that the quality of fit to REE patterns in cpx is comparable to that based on  
391 inversion of REE in cpx alone, as the calculated Pearson's Chi-squares for cpx from the bulk model  
392 and cpx alone model are very similar for the nine samples (Supplementary Table S2). The misfits,  
393 if present, are mostly LREE in opx and cpx. (We will discuss the misfits in a later section.) Figure  
394 4 and supplementary Fig. S4 also show that the recalculated REE patterns in model-derived opx  
395 and cpx (dashed lines) are sensitive to starting mantle mode. This is highlighted by the large  
396 differences in the sum of Pearson's Chi-squares among the three choices of mantle mode (e.g.,  
397 0.94, 4.25, and 15.2 for 14%, 17%, and 20% cpx in the starting mantle, respectively for sample  
398 CK-2). Hence by modeling REE redistribution among cpx, opx, and olivine in the mantle xenolith  
399 after melting, it is possible to constrain mineral mode of the starting mantle. Preferred mineral  
400 modes in the starting mantle for the nine xenoliths are listed in Fig. 5.

401

## 402 **Case study 2: Abyssal peridotites**

403 Trace element abundances in cpx in abyssal peridotites have been widely used to study  
404 melting and melt-rock interaction processes beneath mid-ocean ridges (e.g., Johnson et al., 1990;  
405 Kelemen et al., 1997; Hellebrand et al., 2002, 2005; Salters and Dick, 2002; Hellebrand and Snow,  
406 2003; Brunelli et al., 2006; Warren et al., 2009; Brunelli and Seyler, 2010; D’Errico et al., 2016).  
407 Detailed modeling of REE patterns in residual cpx in abyssal peridotites from Central Indian Ridge  
408 (data from Hellebrand et al., 2002) using an equilibrium double-porosity melting model revealed  
409 a systematic difference between measured and calculated HREE in cpx: model predicted HREE in  
410 cpx are often slightly lower than those measured in actual samples (see Fig. 8 in Liang and Peng,  
411 2010). To fit the HREE in cpx, one can decrease the extent of melting, but this would result in an  
412 over estimation of LREE in cpx. One way to get around this dilemma is by allowing small extent  
413 of chemical disequilibrium for LREE in cpx (Liang and Liu, 2016; Liu and Liang, 2017), which  
414 hinders the depletion of LREE in cpx. This is consistent with diffusion of REE in diopside (Van  
415 Orman et al., 2002). Another possible way to elevate HREE in cpx is through subsolidus  
416 reequilibration, as we demonstrated in previous sections. However, the extent of subsolidus  
417 redistribution may be limited due to higher REE closure temperatures recorded in abyssal  
418 peridotites (Fig. 2). Yet another mechanism to produce depleted LREE and elevated HREE in cpx  
419 is to start melting in the garnet stability field (e.g., Johnson et al., 1990; Hellebrand et al., 2002;  
420 Brunelli et al., 2006).

421 To critically assess the roles of garnet field melting, finite rate of chemical exchange for  
422 LREE, and subsolidus redistribution of REE between cpx and opx in affecting REE patterns in  
423 abyssal peridotites, we select 12 residual abyssal peridotites from the literature that reported REE  
424 abundances in both cpx and opx: 4 samples from eastern Southwest Indian Ridge (SWIR, Seyler  
425 et al., 2011), 2 samples from Gakkel Ridge (D’Errico et al., 2016), 4 samples from western SWIR  
426 (Warren et al., 2009), and 2 samples from Central Atlantic Ridge (Brunelli and Seyler, 2010).  
427 Based on the criteria of Warren (2016), these samples are residual peridotites as they are free of  
428 plagioclase and melt veins, have low  $\text{TiO}_2$  in spinel and depleted LREE patterns in cpx and opx.  
429 Similar to mantle xenoliths, these samples also have well-defined linear trends for at least the  
430 middle and heavy REE in the inversion diagram of the REE-in-two-pyroxene thermometer. Fig.  
431 3b display modal abundances of the selected samples. For reference, we also plot major element  
432 compositions of the samples as a function of bulk MgO content and spinel Cr# in supplementary  
433 Figs. S3a and S3b.

434 Previous experimental studies have demonstrated that melting reaction of peridotite varies  
435 systematically with pressure (e.g., Kinzler and Grove, 1992; Baker and Stolper, 1994; Walter and  
436 Presnall, 1994). The extent of melting in the garnet stability field is a free parameter in most  
437 geochemical studies of REE fractionation during garnet peridotite melting, with values ranging  
438 from less than 1% to more than 10% (e.g., Johnson et al., 1990; Hellebrand et al., 2002; Brunelli  
439 et al., 2006; Liang and Peng, 2010). This free parameter can be eliminated by considering the  
440 thermodynamics of peridotite melting. In this study, we use pMELTS (Ghiorso et al., 2002) to  
441 calculate mineral mode along an adiabatic melting path that has a potential temperature of 1330°C.  
442 The starting mantle (DMM) contains 150 ppm water and melting starts in the garnet stability field.  
443 In this pMELTS-based model, the maximum extent of melting in the garnet stability field is 0.7%  
444 and the cpx exhausts at  $F = 20\%$ . There is no clear experimental nor geophysical evidence for the  
445 presence of high-porosity channels at depth greater than 60 km beneath mid-ocean ridges. Based  
446 on 2D double-porosity ridge modeling of Liu and Liang (2019), high-porosity channels initiating  
447 at depth less than 60 km can better explain geophysically inferred high-porosity region beneath  
448 the ridge axis (Yang et al., 2007; Key et al., 2013). In the absence of high-porosity channels, the  
449 melting suction rate reduces to zero in the double-porosity model (i.e.,  $\mathbb{R} = 0$ ). For this reason, we  
450 use batch melting to model decompression melting in the garnet stability field for abyssal  
451 peridotites. Figure 3b displays variations of mineral mode in residual peridotites calculated using  
452 pMELTS for three choices of starting mantle mineralogy (solid curves). These residual trends  
453 bracket the observed modal variations in the selected samples. Figure 6 shows an example of  
454 MCMC simulations for sample Van 7-85-49 from Western SWIR (Warren et al., 2009). Figure 7  
455 summaries results of our preferred model for the 12 abyssal peridotite samples. Supplementary  
456 Fig. S5 presents detailed simulation results for individual samples. Supplementary Tables S1c and  
457 S2 provide additional information on uncertainties of our preferred melting parameters, Pearson's  
458 Chi-squares, and results from cpx alone inversion. The main results are summarized below.

459 Similar to the case of mantle xenolith, the disequilibrium double-porosity melting model  
460 can fit the bulk REE patterns very well for most of the abyssal peridotite samples included in this  
461 study (Fig. 7). The exceptions are sample Van7-96-38 from Western SWIR (Warren et al., 2009)  
462 and sample Dr 23-3-2 from Eastern SWIR (Seyler et al., 2011) which exhibit some misfits in light  
463 and middle REE (Fig. 7 and Fig. S5). (We will discuss the misfits in the next section.) As in the  
464 case of mantle xenolith, the quality of fit to the bulk REE data is not very sensitive to the starting

465 mantle mode, and the match to the measured REE in cpx and opx depends strongly on the starting  
466 mantle mode (cf. the three cases in Fig. 6, for other samples see Fig. S5). Overall, the matches to  
467 the observed REE patterns in cpx and opx are improved after adjustment of subsolidus  
468 redistribution (cf. solid and dashed lines in Fig. 7). However, the improvement is moderate because  
469 of the relatively high  $T_{REE}$  for the peridotite samples and very small adjustment for REE in cpx.  
470 This may result from incomplete reequilibration of REE between cpx and opx, as we discuss below.  
471 Supplementary Table 2 lists melting parameters of our preferred model for the 12 abyssal  
472 peridotite samples based on the sum of Pearson's Chi-squares of the bulk and subsolidus  
473 redistributed cpx and opx.

474

## 475 **Discussion**

### 476 **Misfits of REE in the bulk samples**

477 Although the disequilibrium double-porosity melting model can account for most of the  
478 variations of REE + Y in the bulk peridotites, noticeable misfits in the light and middle REE are  
479 observed in samples Van7-96-38 (from Western SWIR, Warren et al., 2009) and Dr23-3-2 (from  
480 eastern SWIR, Seyler et al., 2011, see Figs. 7 and S5). In both cases, the model-predicted La, Er,  
481 Tm and Yb in the bulk residue are higher than, whereas the predicted Nd, Sm, E, Gd and Tb are  
482 lower than, measured values in the samples. This humped feature is not sensitive to starting mantle  
483 mode, and is also present in the cpx-alone inversion models. Addition of melt would elevate La in  
484 cpx and opx and hence cannot explain the depleted LREE patterns in the two samples. The lower  
485 than expected bulk La, Er, Tm and Yb can be accounted for by increasing the degree of melting,  
486 but this would result in additional misfits in Nd, Sm, E, Gd and Tb. Since partition coefficients of  
487 middle REE in cpx are higher than those in garnet and the partition coefficients of HREE in cpx  
488 are lower than those in garnet, prolonged melting in the garnet stability field can produce the  
489 humped middle REE pattern in cpx and the bulk residue (e.g., Johnson et al., 1990). Our pMELTS  
490 based model for abyssal peridotites includes 0.7% initial melting in the garnet field. To further  
491 explore the role of garnet field melting, we consider a hypothetical case in which batch melting in  
492 the garnet stability field is 4.1%. Supplementary Fig. S6 presents the simulation results. The  
493 simulated bulk rock and pyroxene REE patterns after 4.1% batch melting in the garnet field show

494 only a small improvement for sample Dr23-3-2 (the sum of Pearson's Chi-squares decreases from  
495 3.8 to 3.3 which is still higher than the other 10 abyssal peridotites) and no improvement at all for  
496 sample Van7-96-38. Hence the misfits are unlikely due to batch melting in the garnet stability field.  
497 Although fractional melting of garnet lherzolite can produce humped REE in cpx (Johnson et al.,  
498 1990), the physical mechanism for fractional melting in the garnet stability field remains uncertain.

499 Abyssal peridotites are heavily altered by serpentinization. It is possible that mineral modes  
500 in these two samples are not accurately determined. To explore this possibility, we reconstruct two  
501 new modal abundances for the two samples: one by increasing cpx mode by 2% and decreasing  
502 opx mode by 2%, and the other by decreasing cpx mode by 2% and increasing opx mode by 2%.  
503 We run MCMC simulations followed by subsolidus redistribution for these 4 cases and the results  
504 are shown in supplementary Fig. S7. Changing cpx mode by  $\pm 2\%$  in the samples does not lead to  
505 a significant improvement in the fit to the reconstructed bulk REE in these two samples (i.e., the  
506 humped pattern persists). However, addition of 2% cpx does result in moderate improvement in  
507 the match to the observed REE patterns in cpx and opx in the two samples. This is confirmed by  
508 the smaller sum of Pearson's Chi-squares for the +2% cpx case.

509 We should point out that none of the hypotheses explored in this section can explain the  
510 humped REE pattern in cpx using the cpx-alone inversion model. In theory, one can match the  
511 observed REE pattern in bulk residue by judiciously adjusting starting mantle composition. It is  
512 possible that composition of the starting mantle for these two samples are different from DMM.  
513 We will come back to this point in the section **Mantle source composition**.

514

#### 515 **Misfits of LREE in opx and cpx: Incomplete reequilibration?**

516 A common misfit shared by all the abyssal peridotite samples and four of the nine mantle  
517 xenoliths (ET80, CK-2, YY-26B, and KN03-25) in this study is that model-derived LREE (La +  
518 Ce + Pr  $\pm$  Nd) are lower in cpx but higher in opx than measured values in cpx and opx, respectively.  
519 The misfit, which persists even after adjustment of subsolidus re-distribution, can be visualized by  
520 plotting the apparent opx/cpx REE partition coefficient against REE ionic radius: the apparent  
521 partition coefficients for the middle and heavy REE follow closely to an isotherm, whereas those  
522 for LREE are gradually displaced above the isotherm, defining a spoon-shaped or U-shaped pattern

523 (Figs. 8a and 8b). In the inversion diagram for the REE-in-two-pyroxene thermometer, the  
524 displaced LREE fall below the linear trend established by the heavy and middle REE and are  
525 excluded from the temperature calculation (Liang et al., 2013). Spoon- or U-shaped opx/cpx REE  
526 partitioning pattern is a common feature among mantle samples (e.g., Stosch, 1982; Agranier and  
527 Lee, 2007; Seyler et al., 2011). It arises when LREE in opx and cpx are out of chemical equilibrium.  
528 Agranier and Lee (2007) identified two mechanisms that can produce U-shaped disequilibrium  
529 patterns in mantle xenoliths from Dish Hill, California and abyssal peridotites from the Gakkel  
530 Ridge: diffusive fractionation at subsolidus state or metasomatism introduced by “injection and  
531 subsequent freezing in of small amounts of melt” under lithospheric or asthenospheric conditions.  
532 The 9 mantle xenoliths and 12 abyssal peridotite samples included in the present study are all  
533 depleted in LREE. Given that our disequilibrium double-porosity melting model can fit the bulk  
534 REE patterns very well in these samples, we can rule out the melt addition hypothesis for these  
535 samples.

536 We suggest that the spoon- or U-shaped opx/cpx REE partitioning patterns can be produced  
537 by disequilibrium melting followed by diffusive exchange between cpx and opx at subsolidus state.  
538 Figures 8a and 8b compare the apparent opx/cpx REE partition coefficients calculated from the  
539 measured REE abundances in opx and cpx in mantle xenolith CK-2 from the Coast Ranges of  
540 central California (Quinn et al., 2018, filled circles) and abyssal peridotite Van7-85-49 from  
541 western SWIR (Warren et al., 2009) with those calculated using melting parameters derived from  
542 our MCMC simulations (magenta lines). (Similar plots for other samples included in this study are  
543 presented in supplementary Figs. S4 and S5.) In both samples, the simulated apparent partition  
544 coefficients at the end of melting are displaced above the measured values. Since opx/cpx REE  
545 partition coefficients decrease with the decrease of temperature (cf. the three isotherms in Fig. 8)  
546 and diffusion coefficients of REE in cpx increase systematically from La to Lu at a given  
547 temperature (Van Orman et al., 2001, 2002; see also supplementary Fig. S1c), time scales for  
548 diffusive exchange between opx and cpx in a closed system are longer for LREE than HREE (see  
549 Fig. 5 in Liang, 2014). During diffusive reequilibration, HREE approach opx/cpx equilibrium  
550 partitioning faster than LREE. Depending on thermal history experienced by the samples (e.g.,  
551 cooling and upwelling rates), the elevated opx/cpx REE patterns produced by disequilibrium  
552 melting (magenta lines in Fig. 8) would be gradually relaxed to the spoon-shaped pattern recorded  
553 in the peridotite samples (filled circles). As a proof-of-concept, we carry out two forward

554 simulations of diffusive reequilibration of REE between opx and cpx under two prescribed cooling  
555 rates. In this simple demonstration, cooling starts at the end of melting and terminates at the closure  
556 temperature of REE (i.e.,  $T = T_{REE}$ ). Figures 8a and 8b show that the results are promising (thin  
557 orange lines). In a more complicate but realistic situation, the cooling rate, which is likely very  
558 different for the mantle xenolith and abyssal peridotite, may vary as a function of time. Hence it  
559 may be possible to deduced cooling rate through detailed modeling of the spoon-shaped opx/cpx  
560 REE patterns in residual peridotites, a subject we will pursue in the future.

561

## 562 **Mantle source composition**

563 The starting mantle composition (DMM vs. PM) affects our inversion results. The depleted  
564 MORB mantle or DMM has been widely used in REE modeling of abyssal peridotites. In their  
565 original studies of mantle xenoliths, Liu et al. (2012) and Harvey et al. (2012) anchored their major  
566 and trace element data to the primitive mantle of McDonough and Sun (1995), whereas Quinn et  
567 al (2018) used HREE in their samples and DMM of Workman and Hart (2005) to infer the extent  
568 of melting. We used the primitive mantle of McDonough and Sun (1995) as the starting mantle  
569 composition in our inversion of the mantle xenolith data (Fig. 5). Composition of the mantle source  
570 is unlikely homogeneous, even for a suite of depleted samples from the same locality. Liu et al.  
571 (2012) reported Nd and Hf isotopic compositions of cpx for the three North China Craton samples  
572 (YY-26, YY-40B, and YY-42) included in this study. They found that samples YY-40B and YY-  
573 42 have considerably higher  $^{143}\text{Nd}/^{144}\text{Nd}$  and  $^{176}\text{Hf}/^{177}\text{Hf}$  ratios than sample YY-26 and suggested  
574 that samples such as YY-26 might be affected by melt addition via melt-rock interaction. As shown  
575 in Fig. 5, REE patterns in the bulk sample, cpx, and opx in YY-26 can be well reproduced by our  
576 two-step melting followed by subsolidus reequilibration model using PM as the starting mantle  
577 composition (see also Fig. S4). The misfit is LREE in opx, which is likely resulted from incomplete  
578 reequilibration at a low temperature ( $T_{REE} = 889$  °C). The higher  $^{143}\text{Nd}/^{144}\text{Nd}$  and  $^{176}\text{Hf}/^{177}\text{Hf}$  ratios  
579 in samples YY-40B and YY-42 suggest that these samples may have derived from a more depleted  
580 mantle source. To test this hypothesis, we run MCMC simulations for samples YY-40B and YY-  
581 42 using DMM as our starting mantle composition. The results are summarized in Supplementary  
582 Table S2 and Fig. S4: the fits to sample YY-40B are slightly improved as the sum of Pearson's  
583 Chi-squares decreases from 1.76 (PM) to 1.68 (DMM), whereas no improvement is observed for

584 YY-42 as the sum of Pearson's Chi-squares increases from 0.62 (PM) to 1.21 (DMM). In fact,  
585 inversion of the remaining 7 xenolith samples with DMM starting composition leads to moderate  
586 to significant reduction in the quality of fits to the observed REE patterns (i.e., the sum of Pearson's  
587 Chi-squares has increased, Fig. S4). This intriguing result suggests that composition of PM is more  
588 suitable for modeling REE depletion in the nine residual mantle xenoliths included in this study.  
589 Given the slight improvement of fits to sample YY-40B using DMM starting mantle composition,  
590 we include inversion results with DMM starting composition in our discussion (two points  
591 connected by red dashed lines in Figs. 9a, 10a, 10c, and 11 below).

592         Composition of the average DMM is a convenient common start point in modeling REE  
593 depletion in abyssal peridotites. According to Warren et al. (2009),  $^{143}\text{Nd}/^{144}\text{Nd}$  ratios in cpx in the  
594 4 samples from SWIR (Van7-85-42, Van7-85-47, Van7-85-49, and Van7-96-38) are more similar  
595 to the depleted endmember of DMM (D-DMM) of Workman and Hart (2005) than the average  
596 DMM (see Fig. 5a in Warren et al., 2009). Intrigued, we run MCMC simulations again for the 4  
597 samples using REE + Y in the D-DMM of Workman and Hart (2005) as the starting mantle  
598 composition. The results are presented in supplementary Fig. S8: the fits to the observed REE in  
599 the bulk, cpx, and opx are slightly improved as the sums of Pearson's Chi-squares for the 4 samples  
600 are all reduced. The small improvement is probably due to the fact that concentration differences  
601 between D-DMM and DMM of Workman and Hart (2005) are small. As noted earlier,  
602 concentrations of Pr to Eu in sample Van7-96-38 are underestimated in our models (Fig. 7). It is  
603 possible that the starting mantle for Van7-96-38 is more depleted than D-DMM. Existence of ultra-  
604 depleted mantle domains have been proposed for magma genesis beneath mid-ocean ridges based  
605 on Os, Nd, and Hf isotope ratios in residual peridotites and olivine-hosted melt inclusions (e.g.,  
606 Liu et al., 2008; Stracke et al., 2011, 2019; Sanfilippo et al., 2019). The mantle source composition  
607 for residual abyssal peridotites such as the ones examined in this study is likely more variable than  
608 that represented by the DMM model of Workman and Hart (2005). More study is needed to  
609 quantify the abundances of REE and other trace elements in these extremely depleted mantle  
610 sources.

611

612 **Mantle source mode**

613 The starting mantle mode also affects fitting results. Our original purpose of exploring 3~6%  
614 variations in cpx and opx modes in the starting lherzolitic mantle was to understand the large  
615 variations in mineral modal abundance observed in the mantle xenoliths and abyssal peridotites  
616 included in this study, as such variations cannot be produced by melting a single mantle source. It  
617 turns out that the quality of fits to the bulk REE in the mantle xenoliths and abyssal peridotites are  
618 not very sensitive to the starting mantle mode, albeit a trade-off between cpx mode in the starting  
619 mantle and the inferred degree of melting. This is explained by the very similar bulk REE partition  
620 coefficients for the three starting mantle modes: they are subparallel to each other in the spider  
621 diagram (see supplementary Fig. S9). Hence one cannot use bulk REE in residual peridotite to  
622 discriminate starting mantle mode. However, REE abundances in residual cpx and opx are  
623 sensitive to starting mantle mode for the mantle xenoliths and abyssal peridotites. This is due  
624 simply to mass balance and temperature-dependent opx/cpx and ol/cpx REE partition coefficients  
625 (Eqs. 5 and 6). During subsolidus reequilibration in a closed system (i.e., for a constant  $C_s$  in Eq.  
626 5), concentrations of REE in opx and ol in lherzolite or harzburgite decrease with the decrease of  
627 temperature, whereas concentrations of REE in cpx increase. At a given temperature, the change  
628 of concentration depends on mineral mode (cf. Figs. 2a and 2b) which, in turn, is sensitive to the  
629 starting mantle mode and the melting reaction. During subsolidus reequilibration, cpx and opx  
630 modes and major element compositions also change due to pyroxene exsolution and subsolidus  
631 reaction among the mantle minerals, which complicates the application of Eq. 6. A preliminary  
632 pMELTS-based study suggests that these major element effects are small to moderate on REE re-  
633 distribution in peridotites (Yao, 2015). Results from this study suggest that the mineral mode in  
634 the starting mantle is not homogeneous and should be taken into consideration in detailed modeling  
635 of REE and other trace elements during mantle melting. This is consistent with the scattered  
636 correlations between the bulk MgO and major and minor elements (CaO, Al<sub>2</sub>O<sub>3</sub>, Na<sub>2</sub>O, and TiO<sub>2</sub>)  
637 in the mantle xenoliths and abyssal peridotites (supplementary Figs. S2a and S3a).

638

### 639 **Comparing extent of melting derived from REE in the bulk and REE in cpx**

640 In general, degrees of melting based on MCMC inversion of REE + Y in the bulk samples  
641 (designated as  $F_{bulk}$  hereafter) and cpx alone ( $F_{cpx}$ ) are positively correlated (Fig. 9). Figure 9a  
642 compares our estimated  $F_{bulk}$  with  $F_{cpx}$  for the nine xenoliths. Samples CK-2 (Coast Ranges of

643 central California, Quinn et al., 2018) and ET80 (East African Rift, Bedini and Bodinier, 1999)  
644 are considerably more fertile in terms of spinel Cr# and contain 12.4% and 15.8% cpx, respectively.  
645 Hence REE + Y in cpx in these two samples should be less affected by subsolidus redistribution.  
646 Indeed, the calculated degrees of melting for CK-2 and ET80 based on the disequilibrium double-  
647 porosity melting model (3.7% and 3.9%) are essentially the same as that derived from HREE in  
648 cpx (2.9% and 4.2%, Supplementary Table S2). Nonetheless, light and middle REE in opx in these  
649 samples are strongly affected by subsolidus redistribution, which is consistent with their low  $T_{REE}$   
650 (964°C and 952°C, respectively). The remaining seven xenolith samples are more depleted. Except  
651 sample YY-42, their inverted  $F_{bulk}$  are 2~6% higher than  $F_{cpx}$ . Sample YY-42 from North China  
652 Craton (Liu et al., 2012) has the lowest cpx mode (4%, a harzburgite), the highest spinel Cr#, and  
653 the second highest  $F_{bulk}$  (19%) among the nine xenolith samples included in this study. This is in  
654 contrast to the rather small  $F_{cpx}$  for this sample (11%, Table S2). Given its very refractory nature,  
655 we suspect that a large fraction of cpx in this sample may have derived from exsolution of opx  
656 after melting. Hence the degree of melting inferred from cpx alone in this sample is not meaningful.  
657 Caution should be exercised when inferring extent of melting using REE abundance in cpx in  
658 harzburgitic mantle xenoliths.

659         Given the relatively high  $T_{REE}$  recorded by the 12 abyssal peridotite samples (Fig. 2) and  
660 the limited extent of subsolidus redistribution of REE between cpx and opx (Fig. 7), it is not  
661 surprising that the inferred degrees of melting based REE in the bulk samples are only slightly  
662 higher than those derived from REE in cpx alone (Fig. 9b). The maximum difference is only 2.2%.  
663 Hence in the absence of bulk REE data, one can use REE in cpx to infer the extent of melting  
664 experienced by residual abyssal peridotites.

665

## 666 **Variations of extent of melting derived from bulk REE with key melting indices**

667         Chromian spinel has been widely used in studies of abyssal peridotites and peridotites from  
668 other tectonic settings (e.g., Dick and Bullen, 1984). Hellebrand et al (2001) showed that spinel  
669 Cr# in residual abyssal peridotites are strongly and inversely correlated with HREE abundances in  
670 cpx in the peridotites and developed empirical equations relating degree of melting to spinel Cr#  
671 for abyssal peridotites. Figure 10a shows the positive correlation between our inverted  $F_{bulk}$  and  
672 spinel Cr# for the xenolith and abyssal peridotite samples included in this study. The abyssal

673 peridotites are bracketed by the batch melting and perfect fractional melting trends of Hellebrand  
674 et al. (2011). However, due to the low spinel Cr#, the mantle xenolith data are mostly plotted below  
675 the batch melting trend (open symbols in Fig. 10a). The latter may in part be due to subsolidus  
676 redistribution of Cr and Al in spinel peridotite (e.g., Voigt and von der Handt, 2011). Caution  
677 should be exercised when inferring extent of melting using Cr# of spinel in well-equilibrated  
678 mantle xenoliths.

679 Our inferred degrees of melting for the mantle xenoliths and abyssal peridotites are  
680 consistent with the observed variation trends of the major and minor elements in the samples. For  
681 example, with increasing degree of melting, MgO in the bulk residue increases from the starting  
682 DMM or PM (Fig. 10b), whereas CaO, Al<sub>2</sub>O<sub>3</sub>, Na<sub>2</sub>O, and TiO<sub>2</sub> in the bulk sample decrease (Figs.  
683 S2c and S3c). The scatteredness of the data shown in Figs. 10b, S2c and S3c can be attributed to  
684 variations in mineral modes, hence major element composition, in the starting mantle.

685

#### 686 **What have we learned from REE abundances in residual pyroxenes and peridotites?**

687 LREE depleted spinel peridotites are generally interpreted as residues of mantle melting.  
688 Through case studies of carefully selected residual spinel peridotites from two distinct tectonic  
689 settings we have demonstrated the advantages of using REE abundances in both the bulk rock and  
690 constituent minerals (cpx and opx) in deducing magmatic and thermal history of the peridotites.  
691 REE abundances in bulk residual peridotites are well-suited for studying melting process, provided  
692 their concentrations are accurately determined, and grain size and mineral mode are known. As a  
693 first application, we kept opx and cpx grain size ratio constant in our MCMC inversion. This is  
694 likely a simplification, as we do not know how grain sizes of cpx and opx vary during mantle  
695 melting and subsolidus reequilibration. LREE in opx and HREE in cpx are more susceptible to  
696 subsolidus redistribution. The extent of redistribution depends on cpx and opx abundances in the  
697 sample and thermal history experienced by the peridotite. We have shown that, by modeling  
698 subsolidus redistribution of REE between opx and cpx after melting, it is possible to discriminate  
699 mineral mode of the starting mantle. HREE in cpx in less primitive spinel lherzolite and  
700 harzburgite from subcontinental lithosphere are significantly reset by subsolidus reequilibration  
701 over geologic time. We do not recommend the use of REE in cpx alone to study mantle melting  
702 process in such samples. The harzburgite YY-42 from North China Craton (Liu et al., 2012) is an

703 extreme example. In the absence of REE abundance in opx, REE in cpx in residual abyssal  
704 peridotites can be used to infer the degree of melting of samples that experienced small to moderate  
705 extent of melting. HREE in highly depleted harzburgite may be affected by subsolidus  
706 reequilibration. By modeling REE abundances in the bulk and constituent cpx and opx, it is also  
707 possible to discriminate starting mantle composition. Results from this study has lent support to  
708 the common practice of using composition of the primitive mantle to model REE depletion in  
709 cratonic mantle xenoliths and composition of DMM to model REE depletion in residual abyssal  
710 peridotites. REE patterns in some of the isotopically more depleted abyssal peridotites such as the  
711 four samples from SWIR (Warren et al., 2009) can be better explained by a starting mantle that is  
712 more depleted than the average DMM.

713         The mantle xenoliths and residual abyssal peridotites examined in this study are a small  
714 fraction of xenolith samples (9 out of 71) and abyssal peridotite samples (12 out of 60) analyzed  
715 in the original studies cited in *Case study 1* and *Case study 2*. To focus on REE depletion in the  
716 bulk peridotite produced by partial melting, we exclude samples that have LREE enriched patterns,  
717 samples that may have been affected by melt addition, and samples that exhibit disequilibrium  
718 partitioning in HREE between opx and cpx. In spite of our conservative approach in sample  
719 selection, we find that it is still not possible to reproduce REE + Y patterns in the bulk and  
720 pyroxenes in these two groups of highly selective mantle peridotites using a starting mantle with  
721 constant mineral mode. It is well known that the upper mantle is chemically (e.g., enriched vs.  
722 depleted) and lithologically (e.g., peridotite vs. pyroxenite) heterogeneous. Results from the present  
723 study suggests that the endmembers of the primitive and depleted peridotitic upper mantle are also  
724 modally heterogeneous. A modally heterogeneous mantle source provides a simple explanation  
725 for the large variations of mineral mode observed in peridotitic mantle xenoliths and abyssal  
726 peridotites. An implication of a modally heterogeneous mantle is that REE abundances of the  
727 mantle source (DMM or PM) likely vary with mineral mode, i.e., a modally heterogeneous mantle  
728 must also be chemically heterogeneous. A mantle source with constant and uniform composition  
729 and mineral mode is merely a convenient starting point in trace element modeling of mantle  
730 melting. Although adequate for examining broad variation trends of a suit of peridotitic samples,  
731 a uniform mantle source is not sufficient to account for detailed variations of REE in both the bulk  
732 peridotite and its constituent minerals, as demonstrated in this study.

733 Finally, we note that the methodology developed in this study can also be applied to other  
734 trace elements in residual peridotites, provided their diffusion in and partitioning between mantle  
735 minerals are well characterized. A potential target is the high field strength elements. Spoon- or  
736 U-shaped opx/cpx REE partitioning patterns are observed in all the abyssal peridotite samples  
737 included in this study. Four of the nine mantle xenoliths that have lower REE closure temperature  
738 also exhibit spoon-shaped REE partitioning pattern. Through simple forward modeling, we have  
739 shown that the spoon- or U-shaped opx/cpx REE partitioning patterns can be produced by  
740 disequilibrium melting followed by diffusive exchange between cpx and opx at subsolidus state.  
741 It may be possible to deduce cooling rate and thermal history through detailed modeling of REE  
742 in coexisting cpx and opx and spoon-shaped opx/cpx REE partitioning patterns in mantle samples.  
743 A prerequisite in subsolidus modeling is the initial concentrations of REE in cpx and opx at the  
744 onset of cooling which corresponds to the end of the disequilibrium melting modeling. The present  
745 study has set a stage for such endeavors in the future.

746

#### 747 **ACKNOWLEDGEMENTS**

748 We thank Daniele Brunelli, Henry Dick, Jingao Liu, and Jessica Warren for useful  
749 discussion regarding grain size in peridotites, and Suzanne Birner for helpful comments and  
750 suggestions on an earlier version of this manuscript. This work was supported by National Science  
751 Foundation grant EAR-1852088 and the China Scholarship Council (201806010079).

752

753 **APPENDIX A. GOVERNING EQUATIONS**

754 The disequilibrium double-porosity melting model of Liang and Liu (2016) is intended for  
 755 modeling trace element fractionation during concurrent melting, channelized melting extraction,  
 756 and finite rate of crystal-melt chemical exchange in an upwelling steady-state melting column. In  
 757 terms of the degree of melting experienced by the solid matrix ( $F$ ), mass conservation equations  
 758 for a trace element in the interstitial melt ( $C_f$ ), residual solid ( $C_s$ ), individual mineral ( $C_s^j$ ) can be  
 759 written as:

$$760 \quad \varepsilon_{cpx}(1 - \mathbb{R})F \frac{dC_f}{dF} = \varepsilon_{cpx}(C_s^p - C_f) + \sum_{j=1}^N w_j \frac{R_j}{R_{cpx}} (C_s^j - k_j C_f) \quad (A1a)$$

$$761 \quad \varepsilon_{cpx} (1 - F) \frac{dC_s}{dF} = \varepsilon_{cpx} (C_s - C_s^p) - \sum_{j=1}^N w_j \frac{R_j}{R_{cpx}} (C_s^j - k_j C_f) \quad (A1b)$$

$$762 \quad \varepsilon_{cpx} (1 - F) \frac{dC_s^j}{dF} = - \frac{R_j}{R_{cpx}} (C_s^j - k_j C_f) \quad (A1c)$$

763 where  $k_j$  is the partition coefficient between mineral  $j$  and melt for the element of interest;  $\mathbb{R}$  is  
 764 the dimensionless melt suction rate defined as the fraction of melt removed from the residual solid  
 765 (to a nearby channel) relative to the amount of melt produced by melting (Iwamori, 1994; Liang  
 766 and Peng, 2010);  $\varepsilon_{cpx}$  is the disequilibrium parameter for a trace element in cpx;  $C_s^p$  is the  
 767 concentration of bulk solid calculated according to melting reaction; and  $w_j$  is the weight fraction  
 768 of mineral  $j$  in residual solid. The latter three parameters are defined as follows:

$$769 \quad \varepsilon_{cpx} = \frac{\Gamma}{\rho_s(1-\phi_f)R_{cpx}} \quad (A1d)$$

$$770 \quad C_s^p = \sum_{j=1}^N w_j^p C_s^j \quad (A1e)$$

$$771 \quad w_j = \frac{w_j^0 - w_j^p F}{1 - F} \quad (A1f)$$

772 where  $\Gamma$  is the melting rate;  $\rho_s$  is the density of the bulk solid;  $\phi_f$  is the volume fraction of the  
 773 melt in the residue;  $w_j^0$  is the weight fraction of mineral  $j$  at the onset of the melting; and  $w_j^p$  is the  
 774 weight fraction of mineral  $j$  participating in the melting reaction. Equations (A1a)-(A1c) can be  
 775 further simplified by assuming that the interstitial melt and olivine and spinel are location chemical  
 776 equilibrium. The mass conservation equations become:

$$777 \left( \varepsilon_{\text{cpx}}(1 - \mathbb{R})F + \varepsilon_{\text{cpx}}(1 - F)(w_{\text{ol}}k_{\text{ol}} + w_{\text{sp}}k_{\text{sp}}) \right) \frac{dC_f}{dF} =$$

$$778 \varepsilon_{\text{cpx}}(C_s^p - C_f) + w_{\text{cpx}}(C_s^{\text{cpx}} - k_{\text{cpx}}C_f) + w_{\text{opx}} \frac{R_{\text{opx}}}{R_{\text{cpx}}} (C_s^{\text{opx}} - k_{\text{opx}}C_f) \quad (\text{A2a})$$

$$779 \varepsilon_{\text{cpx}}(1 - F) \frac{dC_s^{\text{cpx}}}{dF} = -(C_s^{\text{cpx}} - k_{\text{cpx}}C_f) \quad (\text{A2b})$$

$$780 \varepsilon_{\text{cpx}}(1 - F) \frac{dC_s^{\text{opx}}}{dF} = -\frac{R_{\text{opx}}}{R_{\text{cpx}}} (C_s^{\text{opx}} - k_{\text{opx}}C_f) \quad (\text{A2c})$$

$$781 C_s^p = w_{\text{cpx}}^p C_s^{\text{cpx}} + w_{\text{opx}}^p C_s^{\text{opx}} + w_{\text{ol}}^p k_{\text{ol}} C_f + w_{\text{sp}}^p k_{\text{sp}} C_f \quad (\text{A2d})$$

782 Concentration of REE in the bulk residue can be calculated using the expression:

$$783 C_s = \sum w_j C_s^j = w_{\text{cpx}} C_s^{\text{cpx}} + w_{\text{opx}} C_s^{\text{opx}} + w_{\text{ol}} k_{\text{ol}} C_f + w_{\text{sp}} k_{\text{sp}} C_f \quad (\text{A2e})$$

784 Equations (A2a)-(A2c) are closed by the following boundary conditions at the bottom of the  
 785 melting column ( $F = 0$ ):

$$786 C_f(0) = \frac{\varepsilon_{\text{cpx}} k_p + k_0}{k_0(\varepsilon_{\text{cpx}} + k_0)} C_s^0 \quad (\text{A2f})$$

$$787 C_s^{\text{cpx}}(0) = \frac{k_{\text{cpx}}}{k_0} C_s^0 \quad (\text{A2g})$$

$$788 C_s^{\text{opx}}(0) = \frac{k_{\text{opx}}}{k_0} C_s^0 \quad (\text{A2h})$$

789 where  $k_0$  is the bulk solid–melt partition coefficient at the onset of melting; and  $k_p$  is the bulk  
 790 solid–melt partition coefficient according to the melting reaction. Equation (A2f) is based on the  
 791 analysis of Liang and Liu (2016). Equations (A2a)-(A2c) are a set of coupled ordinary differential

792 equations and can be solved numerically using standard methods. In this study, we solve these  
793 equations using the routine ODEIENT in Python.

794

795

796 **References**

- 797 Agranier A. and Lee C. T. A. (2007) Quantifying trace element disequilibria in mantle xenoliths  
798 and abyssal peridotites. *Earth Planetary Science Letter* **257**, 290–298.
- 799 Anders E. and Grevsse N. (1989) Abundances of the elements: Meteoritic and solar. *Geochimica*  
800 *et Cosmochimica Acta* **53**, 197–214.
- 801 Baker M. B. and Stolper E. M. (1994) Determining the composition of high–pressure mantle  
802 melts using diamond aggregates. *Geochimica et Cosmochimica Acta* **58**, 2811–2827.
- 803 Baker M. B. and Stolper E. M. (1994) Determining the composition of high–pressure mantle  
804 melts using diamond aggregates. *Geochimica et Cosmochimica Acta* **58**, 2811–  
805 2827. Bedini R. and Bodinier J. L. (1999) Distribution of incompatible trace elements  
806 between the constituents of spinel peridotite xenoliths: ICP–MS data from the East  
807 African Rift. *Geochimica et Cosmochimica Acta* **63**, 3883–3900.
- 808 Bodinier J-L. and Godard M. (2014) Orogenic, ophiolitic, and abyssal peridotites. In *Treatise on*  
809 *Geochemistry: The Mantle and Core* 2nd Edition (ed. R. W. Carlson). Elsevier, New  
810 York. pp. 103-167.
- 811 Bodinier J. L., Vasseur G., Vernieres J., Dupuy C. and Fabries J. (1990) Mechanisms of Mantle  
812 Metasomatism: Geochemical Evidence from the Lherz Orogenic Peridotite. *Journal of*  
813 *Petrology* **31**, 597–628.
- 814 Brey G. and Kohler T. (1990) Geothermobarometry in four–phase lherzolites II. New  
815 thermobarometers, and practical assessment of existing thermobarometers. *Journal of*  
816 *Petrology* **31**, 1353–1378.
- 817 Brunelli D. and Seyler M. (2010) Asthenospheric percolation of alkaline melts beneath the St.  
818 Paul region (Central Atlantic Ocean). *Earth Planetary Science Letter* **289**, 393–405.
- 819 Brunelli D., Paganelli E. and Seyler M. (2014) Percolation of enriched melts during incremental  
820 open–system melting in the spinel field: a REE approach to abyssal peridotites from the  
821 Southwest Indian Ridge. *Geochimica et Cosmochimica Acta* **127**, 190–203.
- 822 Brunelli D., Seyler M., Cipriani A., Ottolini L. and Bonatti E. (2006) Discontinuous melt  
823 extraction and weak refertilization of mantle peridotites at the Vema Lithospheric Section  
824 (Mid– Atlantic Ridge). *Journal of Petrology* **47**, 745–771.
- 825 Cherniak D. J. (2015) Nb and Ta diffusion in titanite. *Chemical Geology* **413**, 44–50.
- 826 Cherniak D. J. and Liang Y. (2007) Rare earth element diffusion in natural enstatite. *Geochimica*  
827 *et Cosmochimica Acta* **71**, 1324–1340.
- 828 D’Errico M. E., Warren J. M. and Godard M. (2016) Evidence for chemically heterogeneous  
829 Arctic mantle beneath the Gakkel Ridge. *Geochimica et Cosmochimica Acta* **174**, 291–  
830 312.

- 831 Dick H. J. B. and Bullen T. (1984) Chromian spinel as a petrogenetic indicator in abyssal and  
832 alpine-type peridotites and spatially associated lavas. *Contributions to Mineralogy and*  
833 *Petrology* **86**, 54–76.
- 834 Dygert N. and Liang Y. (2015) Temperatures and cooling rates recorded in REE in coexisting  
835 pyroxenes in ophiolitic and abyssal peridotites. *Earth Planetary Science Letter* **420**, 151–  
836 161.
- 837 Dygert N., Kelemen P. B. and Liang, Y. (2017) Spatial variations in cooling rate in the mantle  
838 section of the Samail ophiolite in Oman: Implications for formation of lithosphere at  
839 mid-ocean ridges. *Earth and Planetary Science Letters* **465**, 134–144.
- 840 Ghiorso M. S., Hirschmann M. M., Reiners P. W. and Kress V. C. (2002) The pMELTS: a  
841 revision of MELTS for improved calculation of phase relations and major element  
842 partitioning related to partial melting of the mantle to 3 GPa. *Geochemistry, Geophysics,*  
843 *Geosystems* **3**, 1–35.
- 844 Harvey J., Yoshikawa M., Hammond S. J. and Burton K. W. (2012) Deciphering the trace  
845 element characteristics in Kilauea Hole peridotite xenoliths: melt–rock interaction  
846 and metasomatism beneath the Rio Grande Rift, SW USA. *Journal of Petrology* **53**, 1709–  
847 1742.
- 848 Hellebrand E. and Snow J. E. (2003) Deep melting and sodic metasomatism underneath the  
849 highly oblique-spreading Lena Trough (Arctic Ocean). *Earth and Planetary Science*  
850 *Letters* **216**, 283–299.
- 851 Hellebrand E., Snow J. E., Dick H. J. B. and Hofmann A. W. (2001) Coupled major and trace  
852 elements as indicators of the extent of melting in mid-ocean-ridge peridotites. *Nature*  
853 **410**, 677–681.
- 854 Hellebrand E., Snow J. E., Hoppe P. and Hofmann A. W. (2002) Garnet–field melting and late-  
855 stage refertilization in ‘residual’ abyssal peridotites from the Central Indian Ridge.  
856 *Journal of Petrology* **43**, 2305–2338.
- 857 Hellebrand E., Snow J. E., Mostefaoui S. and Hoppe P. (2005) Trace element distribution  
858 between orthopyroxene and clinopyroxene in peridotites from the Gakkel Ridge: a SIMS  
859 and NanoSIMS study. *Contributions to Mineralogy and Petrology* **150**, 486–504.
- 860 Iwamori H. (1994)  $^{238}\text{U}$ – $^{230}\text{Th}$ – $^{226}\text{Ra}$  and  $^{235}\text{U}$ – $^{231}\text{Pa}$  disequilibria produced by mantle melting  
861 with porous and channel flows. *Earth and Planetary Science Letters* **125**, 1–16.
- 862 Johnson K. T. M. (1998) Experimental determination of partition coefficients for rare earth and  
863 high-field-strength elements between clinopyroxene, garnet, and basaltic melt at high  
864 pressures. *Contributions to Mineralogy and Petrology* **133**, 60–68.
- 865 Johnson K. T. M. and Dick H. J. B. (1992) Open system melting and temporal and spatial  
866 variation of peridotite and basalt at the Atlantis II Fracture Zone. *Journal of Geophysical*  
867 *Research: Solid Earth* **97**, 9219–9241.

- 868 Johnson K. T. M., Dick H. J. B. and Shimizu N. (1990) Melting in the oceanic upper mantle: an  
869 ion microprobe study of diopsides in abyssal peridotites. *Journal of Geophysical*  
870 *Research: Solid Earth* **95**, 2661–2678.
- 871 Jull M., Kelemen P. B., Sims K. (2002) Consequences of diffuse and channelled porous melt  
872 migration on uranium series disequilibria. *Geochimica et Cosmochimica Acta* **66**, 4133-  
873 4148.
- 874 Kelemen P. B., Hirth G., Shimizu N., Spiegelman M. and Dick H. J. B. (1997) A review of melt  
875 migration processes in the adiabatically upwelling mantle beneath oceanic spreading  
876 ridges. *Philosophical Transactions: Mathematical, Physical and Engineering Science* **355**,  
877 283–318.
- 878 Key K., Constable S., Liu L., and Pommier A. (2013) Electrical image of passive mantle  
879 upwelling beneath the northern East Pacific Rise. *Nature* **495**, 499-502.
- 880 Kinzler R. J. and Grove T. L. (1992) Primary magmas of mid-ocean ridge basalts 1. Experiments  
881 and methods. *Journal of Geophysical Research: Solid Earth* **97**, 6885–6906.
- 882 Lee C. T. A., Harbert A. and Leeman W. P. (2007) Extension of lattice strain theory to  
883 mineral/mineral rare–earth element partitioning: An approach for assessing  
884 disequilibrium and developing internally consistent partition coefficients between olivine,  
885 orthopyroxene, clinopyroxene and basaltic melt. *Geochimica et Cosmochimica Acta* **71**,  
886 481–496.
- 887 Liang Y. (2003) On the thermo–kinetic consequences of slab melting. *Geophysical Research*  
888 *Letter* **30**, 2270. [http://dx.doi.org/ 10.1029/2003GL018969](http://dx.doi.org/10.1029/2003GL018969).
- 889 Liang Y. (2014) Time scales of diffusive re–equilibration in bi–mineralic systems with and  
890 without a fluid or melt phase. *Geochimica et Cosmochimica Acta* **132**, 274–287.
- 891 Liang Y. and Liu B. (2016) Simple models for disequilibrium fractional melting and batch  
892 melting with application to REE fractionation in abyssal peridotites. *Geochimica et*  
893 *Cosmochimica Acta* **173**, 181–197.
- 894 Liang Y. and Peng Q. (2010) Non–modal melting in an upwelling mantle column: steady–state  
895 models with applications to REE depletion in abyssal peridotites and the dynamics of  
896 melt migration in the mantle. *Geochimica et Cosmochimica Acta* **74**, 321– 339.
- 897 Liang Y., Sun C. and Yao L. (2013) A REE–in–two–pyroxene thermometer for mafic and  
898 ultramafic rocks. *Geochimica et Cosmochimica Acta* **102**, 246–260.
- 899 Liu B. and Liang Y. (2017) An introduction of Markov chain Monte Carlo method to  
900 geochemical inverse problems: Reading melting parameters from REE abundances in  
901 abyssal peridotites. *Geochimica et Cosmochimica Acta* **203**, 216–234.
- 902 Liu B. and Liang Y. (2019) Importance of permeability and deep channel network on the  
903 distribution of melt, fractionation of REE in abyssal peridotites, and U-series

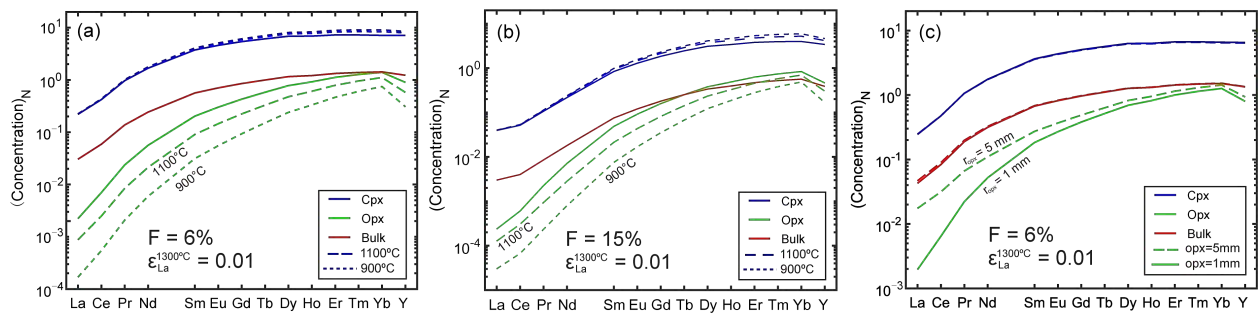
- 904 disequilibria in basalts beneath mid-ocean ridges: A numerical study using a 2D double-  
905 porosity model. *Earth Planetary Science Letters* **528**, 115788.
- 906 Liu C.-Z., Snow J. E., Hellebrand E., Brugmann G., von der Handt A., Buchl A. and Hofmann  
907 A. W. (2008) Ancient, highly heterogeneous mantle beneath Gakkel ridge, Arctic Ocean.  
908 *Nature* **452**, 311–316.
- 909 Liu J., Carlson R. W., Rudnick R. L., Walker R. J., Gao S. and Wu F. (2012) Comparative Sr–  
910 Nd–Hf–Os–Pb isotope systematics of xenolithic peridotites from Yangyuan, North China  
911 Craton: additional evidence for a Paleoproterozoic age. *Chemical Geology* **332**, 1–14.
- 912 Lundstrom C. (2000) Models of U–series disequilibria generation in MORB: the effects of two  
913 scales of melt porosity. *Physics of the Earth and Planetary Interiors* **121**, 189–204.
- 914 McDonough W. F. and Sun S. S. (1995) The composition of the Earth. *Chemical Geology* **120**,  
915 223–253.
- 916 Navon O. and Stolper E. (1987) Geochemical consequences of melt percolation: the upper  
917 mantle as a chromatographic column. *The Journal of Geology* **95**, 285–307.
- 918 Niu Y. and He´kinian R. (1997) Spreading–rate dependence of the extent of mantle melting  
919 beneath ocean ridges. *Nature* **385**, 326– 329.
- 920 Quinn D. P., Saleeby J., Ducea M., Luffi P. and Asimow P. (2018) Late–Cretaceous con–  
921 struction of the mantle lithosphere beneath the central California coast revealed by  
922 Crystal Knob xenoliths. *Geochemistry, Geophysics, Geosystems* **19**, 3302–3346.
- 923 Salters V. J. M. and Dick H. J. B. (2002) Mineralogy of the mid– ocean–ridge basalt source from  
924 neodymium isotopic composition of abyssal peridotites. *Nature* **418**, 68–72.
- 925 Sambridge M. and Mosegaard K. (2002) Monte Carlo methods in geophysical inverse problems.  
926 *Reviews of Geophysics* **40**, 1009.
- 927 Sanfilippo A., Salters V., Tribuzio R. and Zanetti A. (2019) Role of ancient, ultra–depleted  
928 mantle in mid–ocean–ridge magmatism. *Earth Planetary Science Letter* **511**, 89–98.
- 929 Seyler M., Brunelli D., Toplis M. J. and Me´vel C. (2011) Multiscale chemical heterogeneities  
930 beneath the eastern Southwest Indian Ridge (52° E–68° E): Trace element compositions  
931 of along–axis dredged peridotites. *Geochemistry, Geophysics, Geosystems* **12**, Q0AC15,  
932 doi:10.1029/2011GC003585.
- 933 Shimizu N. (1998) The geochemistry of olivine–hosted melt inclusions in a FAMOUS basalt  
934 ALV519–4–1. *Physics of the Earth and Planetary Interiors* **107**, 183–201.
- 935 Stosch H. G. (1982) Rare earth element partitioning between minerals from anhydrous spinel  
936 peridotite xenoliths. *Geochimica et Cosmochimica Acta* **46**, 793–811.
- 937 Stracke A., Genske F., Berndt J. and Koornneef J. M. (2019) Ubiquitous ultra–depleted domains  
938 in Earth’s mantle. *Nature Geoscience* **12**, 851–855.

- 939 Stracke A., Snow J. E., Hellebrand E., von der Handt A., Bourdon B., Birbaum K. and Günther,  
940 D. (2011) Abyssal peridotite Hf isotopes identify extreme mantle depletion. *Earth*  
941 *Planetary Science Letter* **308**, 359–368.
- 942 Sun C. and Liang, Y. (2014) An assessment of subsolidus re-equilibration on REE distribution  
943 among mantle minerals olivine, orthopyroxene, clinopyroxene, and garnet in peridotites.  
944 *Chemical Geology* **372**, 80–91.
- 945 Van Orman J. A., Grove T. L. and Shimizu N. (2001) Rare earth element diffusion in diopside;  
946 influence of temperature, pressure, and ionic radius, and an elastic model for diffusion in  
947 silicates. *Contributions to Mineralogy and Petrology* **141**, 687–703.
- 948 Van Orman J. A., Grove T. L. and Shimizu N. (2002) Diffusive fractionation of trace elements  
949 during production and transport of melt in Earth's upper mantle. *Earth Planetary Science*  
950 *Letter* **198**, 93–112.
- 951 Voigt M. and von der Handt A. (2011) Influence of subsolidus processes on the chromium  
952 number in spinel in ultramafic rocks. *Contributions to Mineralogy and Petrology* **162**,  
953 675–689.
- 954 Walter M. J. and Presnall D. C. (1994) Melting behavior of simplified lherzolite in the system  
955 CaO–MgO–Al<sub>2</sub>O<sub>3</sub>–SiO<sub>2</sub>–Na<sub>2</sub>O from 7 to 35 kbar. *Journal of Petrology* **35**, 329–359.
- 956 Wang C., Liang Y. and Xu W. (2015) On the significance of temperatures derived from major  
957 element and REE based two-pyroxene thermometers for mantle xenoliths from the North  
958 China Craton. *Lithos* **224–225**, 101–113.
- 959 Warren J. M. (2016) Global variations in abyssal peridotite compositions. *Lithos* **248–251**, 193–  
960 219.
- 961 Warren J. M., Shimizu N., Sakaguchi C., Dick H. J. B. and Nakamura E. (2009) An assessment  
962 of upper mantle heterogeneity based on abyssal peridotite isotopic compositions. *Journal*  
963 *of Geophysical Research* **114**, B122023, doi:10.1029/2008JB006186.
- 964 Witt-Eickschen G. and O'Neill H. S. C. (2005) The effect of temperature on the equilibrium  
965 distribution of trace elements between clinopyroxene, orthopyroxene, olivine and spinel  
966 in upper mantle peridotite. *Chemical Geology* **221**, 65–101.
- 967 Workman R. K. and Hart S. R. (2005) Major and trace element composition of the depleted  
968 MORB mantle (DMM). *Earth Planetary Science Letter* **231**, 53–72.
- 969 Yang Y. Forsyth D. W., and Weeraratne D. S. (2007) Seismic attenuation near the East Pacific  
970 Rise and the origin of the low-velocity zone. *Earth Planet. Sci. Lett.* **258**, 260–268.
- 971 Yao L. (2015) Closure Temperature and Closure Pressure in Bi-Mineralic Systems with  
972 Applications to REE-in-Two-Mineral Thermobarometers. Brown University Ph.D.  
973 thesis.

974 Yao L. and Liang Y. (2015) Closure temperature in cooling bi-mineralic systems: I. Definition  
975 and with application to REE-in-two-pyroxene thermometer. *Geochimica et*  
976 *Cosmochimica Acta* **162**, 137–150.

977

978 **Figures**



979

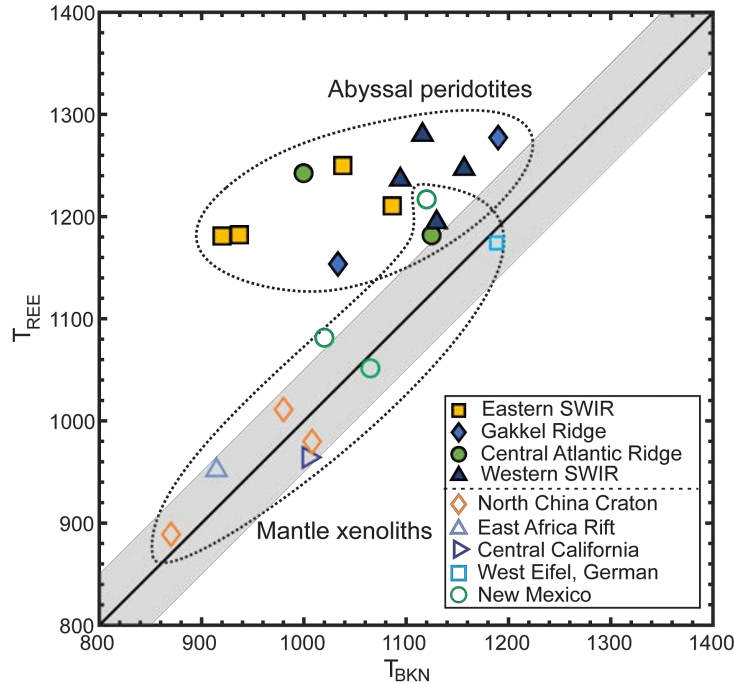
980 Fig. 1. (a) Forward simulation of REE patterns in residual solid, clinopyroxene (cpx), and  
 981 orthopyroxene (opx) after 6% disequilibrium melting followed by subsolidus reequilibration. The  
 982 solid lines represent REE patterns calculated using the disequilibrium melting model and melting  
 983 parameters of  $\epsilon_{La}^{1300} = 0.01$  and  $R = 0.95$ . The dashed lines represent the recalculated REE  
 984 concentrations in the two pyroxenes at 1100°C and 900°C. (b) same as (a) but with 15% melting.  
 985 (c) Comparison of REE patterns in residual solid, cpx, and opx after 6% disequilibrium melting  
 986 for two choices of opx grain size. The solid lines represent the case of  $r_{cpx} = 1$  mm and the dashed  
 987 lines are for  $r_{opx} = 5$  mm. The grain size of cpx is assumed to be 1 mm. Parameters used in this  
 988 simulation are as same as in (a). The temperature-dependent cpx-opx partition coefficients are  
 989 from Sun and Liang (2014). Concentrations of REE are normalized to CI chondrite using the values  
 990 of Anders and Grevesse (1989).

991

992

993

994

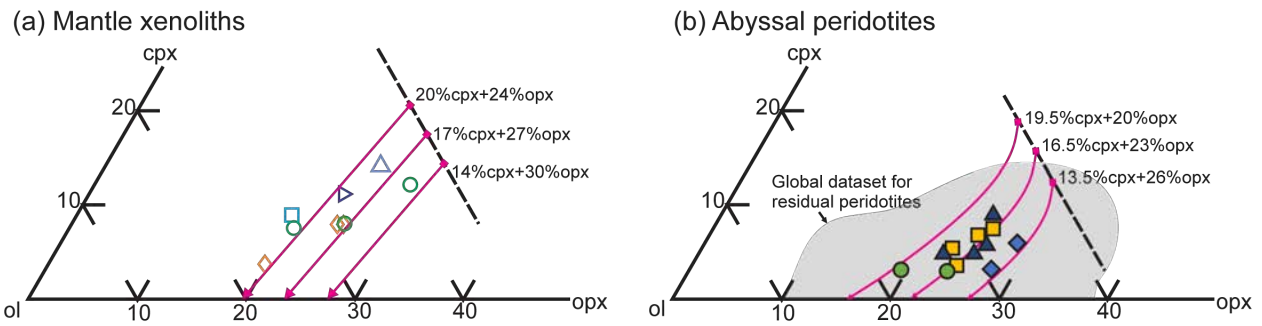


995

996 Fig. 2. Comparison of the temperatures derived from the REE-in-two-pyroxene thermometer of  
 997 Liang et al. (2013,  $T_{REE}$ ) and those calculated using the two-pyroxene thermometer of Brey and  
 998 Kohler (1990,  $T_{BKN}$ ) for the 9 mantle xenoliths and 12 abyssal peridotites included in this study  
 999 (see text for a list of the source of data). All calculations were performed assuming a pressure of  
 1000 1.5 GPa.

1001

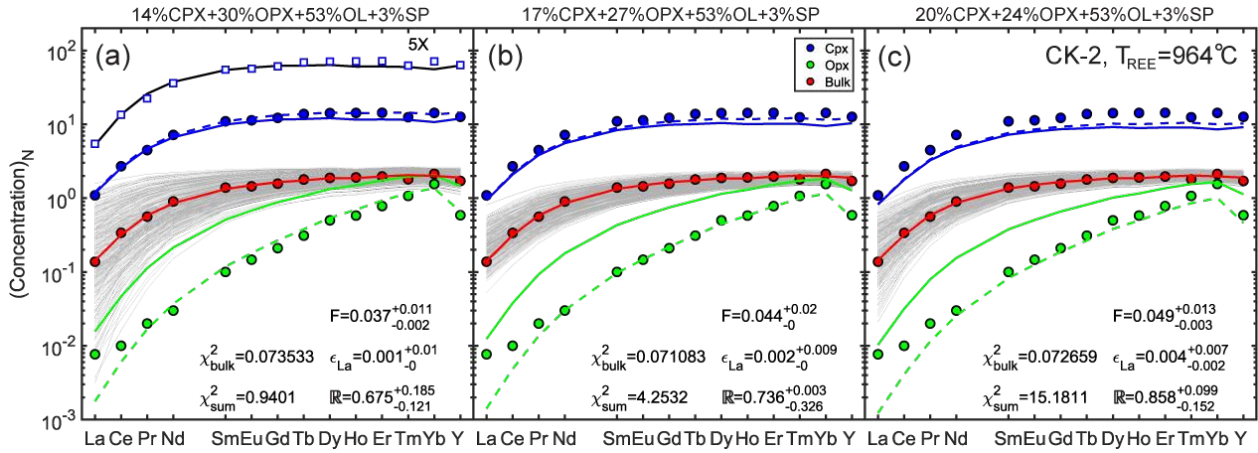
1002



1003

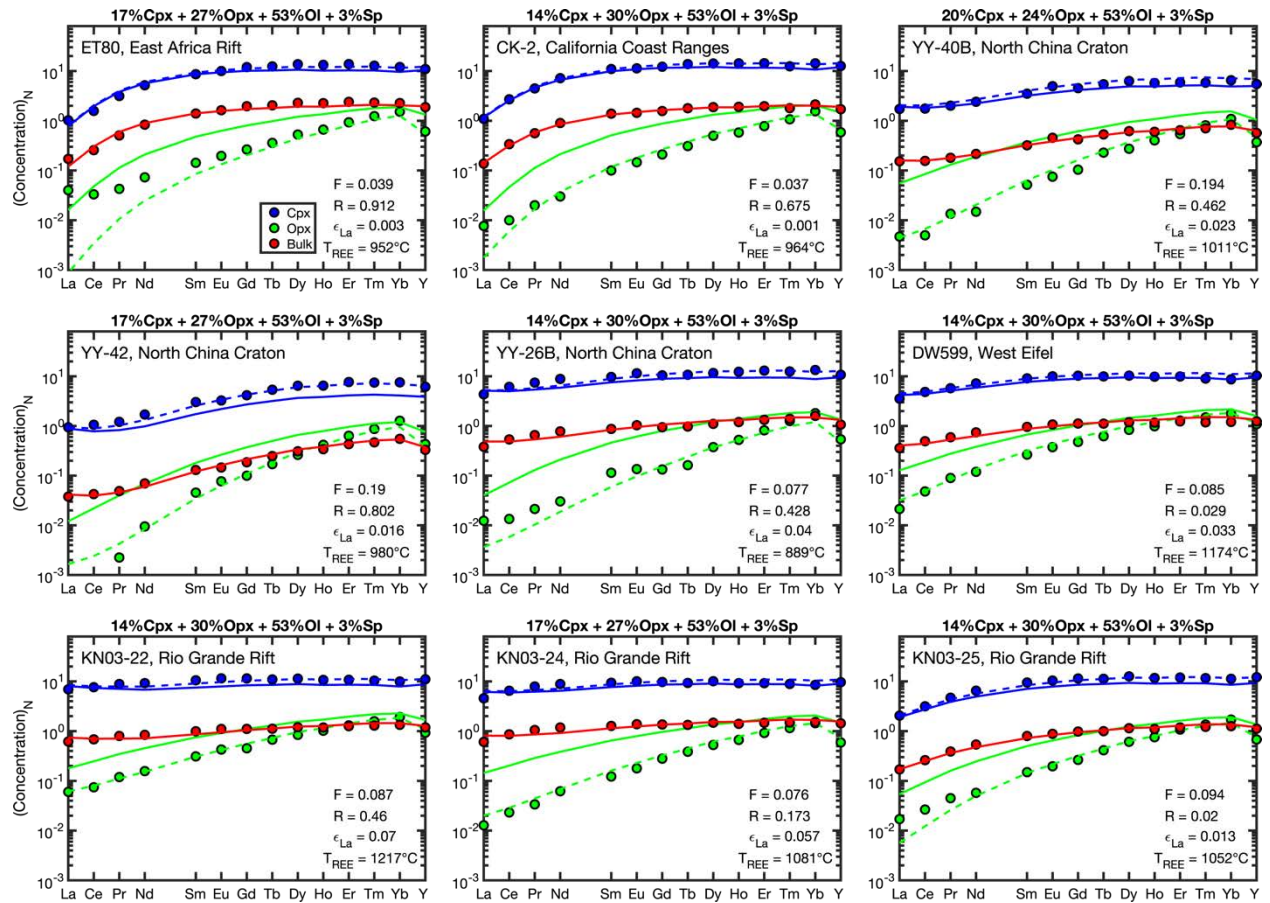
1004 Fig. 3. Modal abundances of clinopyroxene (cpx), orthopyroxene (opx), and olivine (ol) in mantle  
 1005 xenoliths (a) and abyssal peridotites (b) selected in this study. The magenta lines in (a) are  
 1006 calculated using the melting reaction of Baker and Stolper (1994):  $0.38 \text{ opx} + 0.71 \text{ cpx} + 0.13$   
 1007  $\text{spinel} = 0.22 \text{ olivine} + 1 \text{ melt}$  and for three choices of starting mantle mode. The light grey area in  
 1008 (b) is based on Warren (2016) for residual abyssal peridotites from around the world. The magenta  
 1009 curves in (b) represent melting paths based on pMELTS with potential temperature of 1330 °C and  
 1010 150 ppm water content and three choices of starting mantle mode. Sample legends are the same as  
 1011 in Fig. 2.

1012



1013

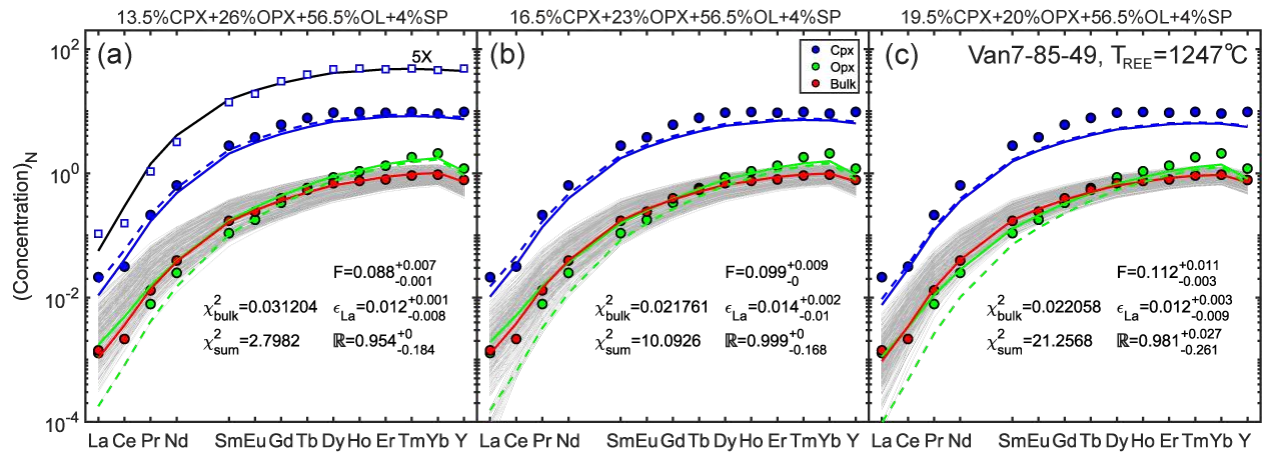
1014 Fig. 4. Comparison between observed (circles) and model derived (curves) REE+Y patterns in the  
 1015 bulk and two pyroxenes in the xenolith sample CK-2 (Quinn et al., 2018). Simulation results for  
 1016 three starting mantle modes are shown in panels (a), (b), and (c). The grey solid curves are MCMC  
 1017 predictions and the red solid curve represents the best-fit of the bulk REE+Y data. The solid blue  
 1018 and green curves represent the calculated REE abundances in cpx and opx, respectively, based on  
 1019 the inversed melting parameters of the best-fit of the bulk data. The dashed blue and green curves  
 1020 represent the model predicted subsolidus REE abundances in cpx and opx at  $T = T_{REE}$ , calculated  
 1021 using the temperature-dependent cpx-opx partition coefficients of Sun and Liang (2014). The sum  
 1022 of Pearson's Chi-square ( $\chi^2_{sum}$ ) is the sum of the Chi-squares of simulated bulk (red curve) and  
 1023 simulated cpx and opx after subsolidus re-equilibrium (dashed bulk and green curves). The open  
 1024 squares and black curve in (a) represent the cpx data and the best-fit result based on the cpx-alone  
 1025 melting model. For clarity, data from cpx-alone simulations were elevated by a factor of 5.  
 1026 Concentrations of REE are normalized to CI chondrite using the values of Anders and Grevesse  
 1027 (1989).



1028

1029 Fig. 5. Summary of preferred models for the nine mantle xenolith samples with REE + Y in the  
 1030 primitive mantle as starting mantle compositions. Modal abundance of the starting mantle is listed  
 1031 for each sample. The solid red curves are the best-fits of the bulk REE + Y data (circles). The  
 1032 solid blue and green curves represent the calculated REE concentrations in cpx and opx,  
 1033 respectively, based on the inversed melting parameters. The dashed blue and green curves  
 1034 represent the model predicted subsolidus REE abundances in cpx and opx at  $T = T_{REE}$ , calculated  
 1035 using the temperature-dependent cpx-opx partition coefficients of Sun and Liang (2014). Results  
 1036 of MCMC simulations with PM and DMM starting compositions for the nine xenolith samples are  
 1037 presented in supplementary Fig. S4 and Tables S1b and S2.

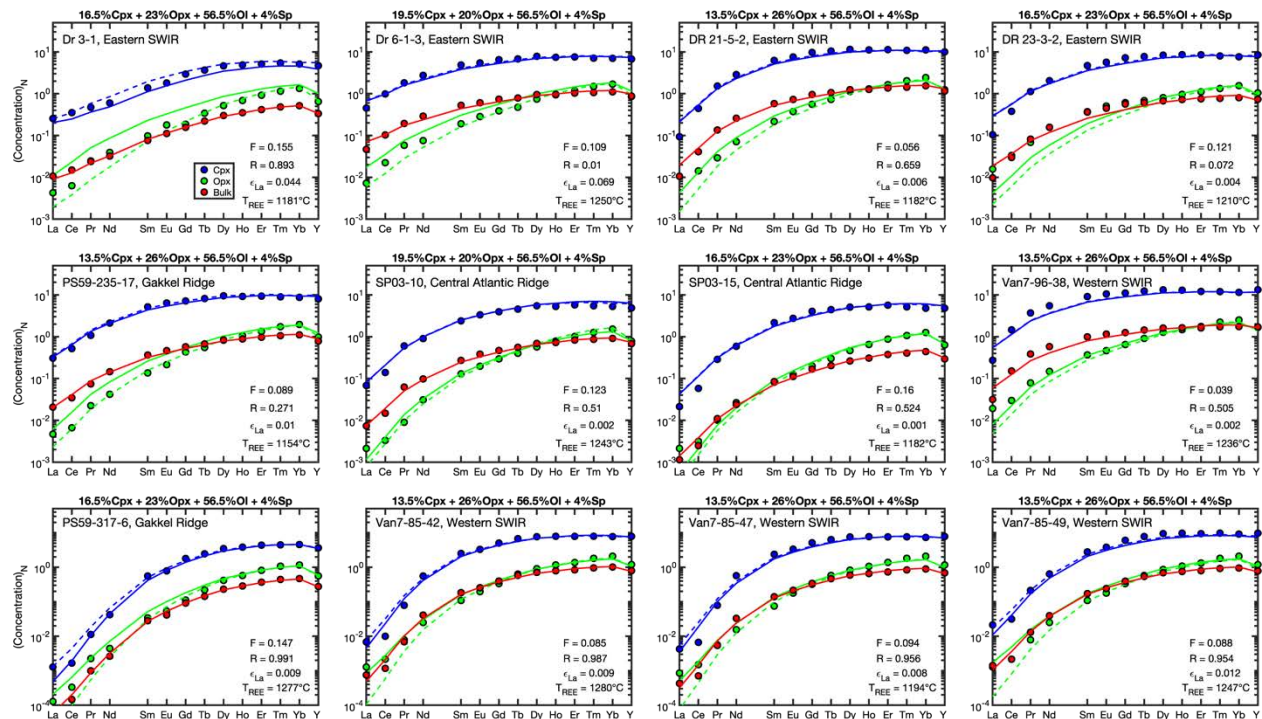
1038



1039

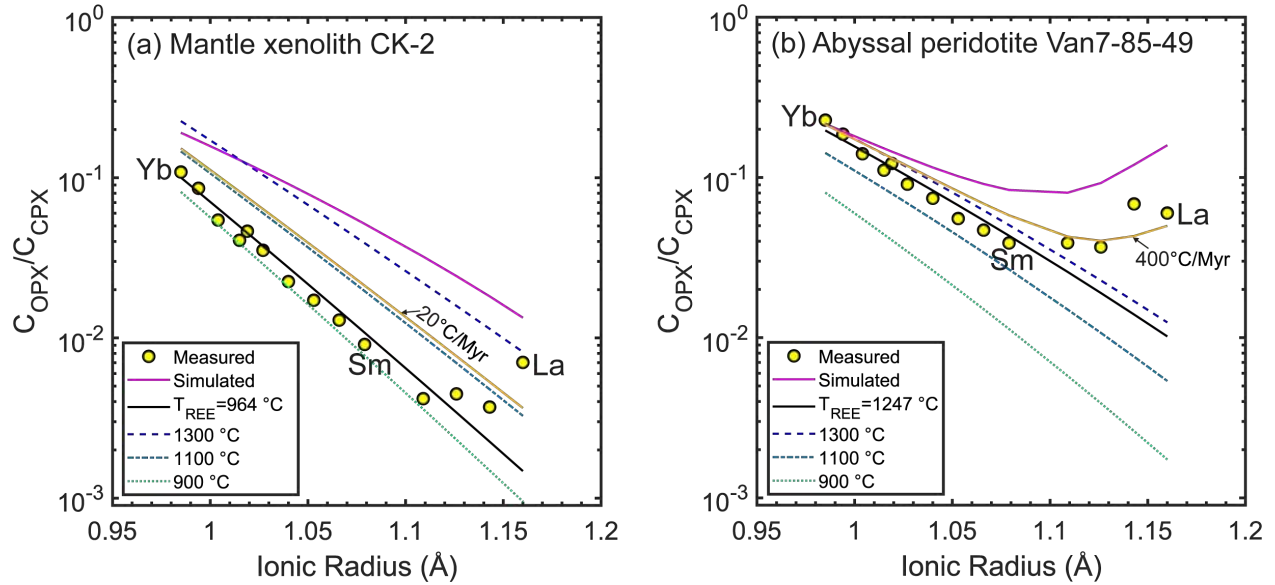
1040 Fig. 6. Comparison between observed (circles) and model derived (curves) REE+Y patterns in the  
 1041 bulk and two pyroxenes in the abyssal peridotite sample Van7-85-49 (Warren et al., 2009). For a  
 1042 detailed explanation of symbols and curves, a reader is referred to the caption to Fig. 4.

1043



1044

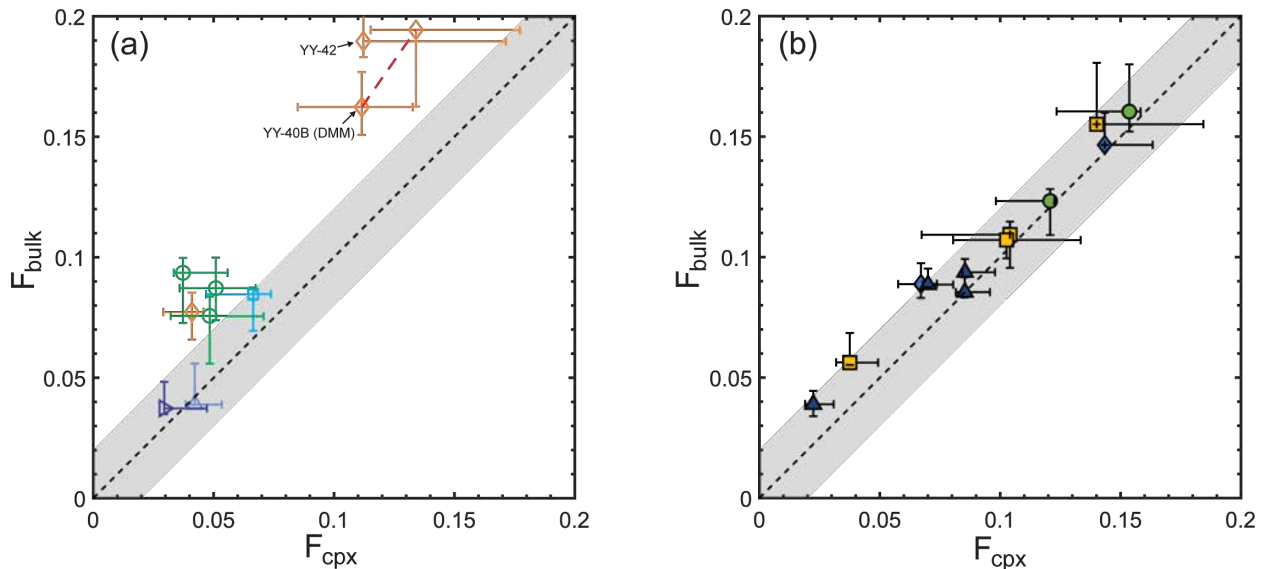
1045 Fig. 7. Summary of preferred models for the twelve abyssal peridotite samples with REE + Y in  
 1046 DMM as starting mantle compositions. Modal abundance of the starting mantle is listed for each  
 1047 sample. Supplementary Fig. S5 presents detailed simulation results for individual samples.  
 1048 Supplementary Tables S1c and S2 provide additional information on uncertainties of preferred  
 1049 melting parameters, Pearson's Chi-squares, and results from cpx alone inversion. Symbols are the  
 1050 same as those described in the caption to Fig. 5.



1051

1052 Fig. 8. Variations of the apparent opx-cpx REE partition coefficient as a function of REE ionic  
 1053 radius for the xenolith sample CK-2 (a) and abyssal peridotite Van7-85-49 (b). The yellow circles  
 1054 represent the measured data. The magenta and black curves represent the model predicted apparent  
 1055 partition coefficients at the end of melting and at the subsolidus temperature  $T = T_{REE}$ , respectively.  
 1056 The thin orange curves were calculated using a simple model for diffusive reequilibration between  
 1057 two minerals at the stated cooling rates. The three dashed curves are the calculated opx-cpx REE  
 1058 partition coefficients using the model of Sun and Liang (2014).

1059

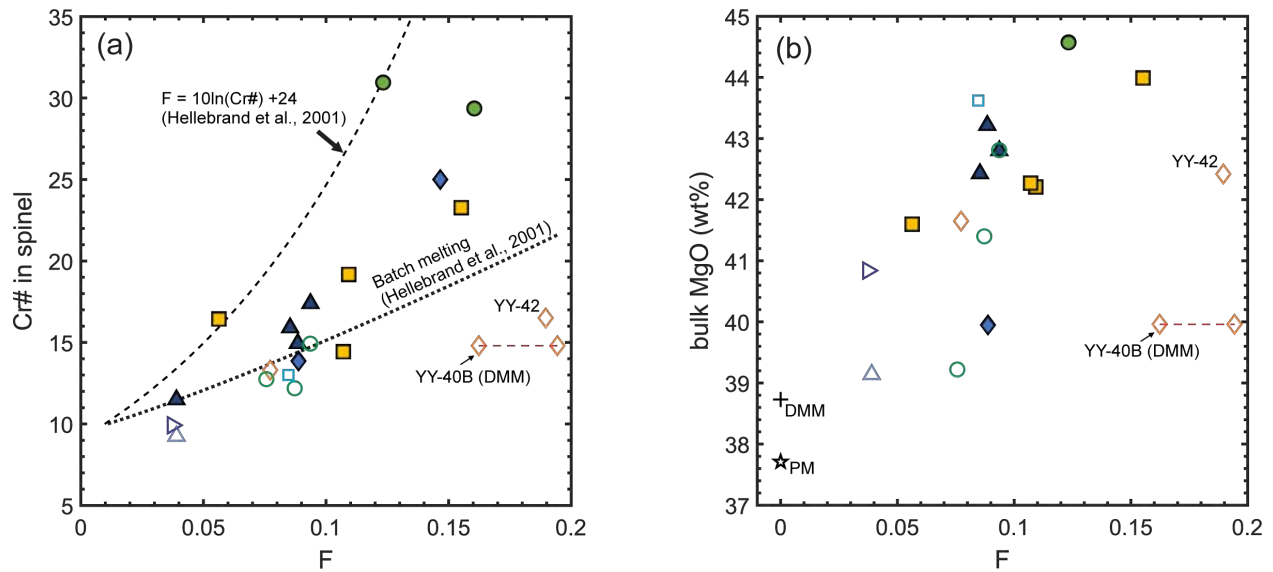


1060

1061 Fig. 9. Comparison of the degree of melting derived from the cpx-alone inversion ( $F_{cpx}$ ) and the  
 1062 degree of melting derived from inversion of the bulk sample ( $F_{bulk}$ ) for the mantle xenoliths (a)  
 1063 and abyssal peridotites (b) selected in this study. The dashed lines and grey areas represent the 1:1  
 1064 ratio within a  $\pm 2\%$  range. The red dashed line in (a) connects the inversion results of sample YY-

1065 40B with primitive mantle (PM) and the depleted MORB mantle (DMM) starting compositions.  
1066 Error bars are based on MCMC simulations. Sample legends are the same as in Fig. 2.

1067



1068

1069 Fig. 10. Variations of spinel Cr# (a) and bulk MgO content (b) as a function of the degree of  
1070 melting for the mantle xenoliths (open symbols) and abyssal peridotites (filled symbols) included  
1071 in this study. The two dashed lines are based on the empirical expressions of Hellebrand et al.  
1072 (2001) for fractional and batch melting. Symbols are the same as in Fig. 2.